AFRL-ML-TY-TR-2004-4517

Development Of A Flexible Molecular Photocell With Up To 20% Conversion Efficiency

K.R. Thampi, PhD., M.G. Graetzel, PhD.

Swiss Federal Institute of Technology (EPFL)
Laboratory of Photonics and Interfaces (LPI)
Institute Of Molecular and Biological Chemistry (ICMB)
Lausanne, Switzerland, CH-1015

Approved For Public Release: Distribution Unlimited

AIR FORCE RESEARCH LABORATORY
MATERIALS & MANUFACTURING DIRECTORATE
AIR EXPEDITIONARY FORCES TECHNOLOGIES DIVISION
139 BARNES DRIVE, STE 2
TYNDALL AFB FL 32403-5323

20040422 068

NOTICES

USING GOVERNMENT DRAWINGS, SPECIFICATIONS, OR OTHER DATA INCLUDED IN THIS DOCUMENT FOR ANY PURPOSE OTHER THAN GOVERNMENT PROCUREMENT DOES NOT IN ANY WAY OBLIGATE THE US GOVERNMENT. THE FACT THAT THE GOVERNMENT FORMULATED OR SUPPLIED THE DRAWINGS, SPECIFICATIONS, OR OTHER DATA DOES NOT LICENSE THE HOLDER OR ANY OTHER PERSON OR CORPORATION; OR CONVEY ANY RIGHTS OR PERMISSION TO MANUFACTURE, USE, OR SELL ANY PATENTED INVENTION THAT MAY RELATE TO THEM.

THIS REPORT IS RELEASABLE TO THE NATIONAL TECHNICAL INFORMATION SERVICE
5285 PORT ROYAL RD.
SPRINGFIELD VA 22 161
TELEPHONE (703) 487-4650; (703) 487-4639 (TDD for the hearing-impaired)
E-MAIL orders@ntis.fedworld.gov
WWW http://www.ntis.gov/index.html

AT NTIS, IT WILL BE AVAILABLE TO THE GENERAL PUBLIC, INCLUDING FOREIGN NATIONS.

THIS TECHNICAL REPORT HAS BEEN REVIEWED AND IS APPROVED FOR PUBLICATION.

REZA SALAVANI
Program Manager

RICHARD N. VICKERS, DR-IV
Chief, Deployed Base Systems Branch

JIMMY L. POLLARD, Colonel, USAF
Chief, Airbase Technologies Division

Do not return copies of this report unless contractual obligations or notice on a specific document requires its return.

REPORT DOCUMENTATION PAGE	Form Approved OMB No. 0704-0188

Public reporting burden for this collection of information is estimated to average 1 hour per response, including the time for reviewing instructions, searching existing data sources, gathering and maintaining the data needed, and completing and reviewing the collection of information. Send comments regarding this burden estimate or any other aspect of this collection of information, including suggestions for reducing this burden, to Washington Headquarters Services, Directorate for Information Operations and Reports, 1215 Jefferson Davis Highway, Suite 1204, Arlington, VA 22202-4302, and to the Office of Management and Budget, Paperwork Reduction Project (0704-0188), Washington, DC 20503.

1. AGENCY USE ONLY (Leave blank)	2. REPORT DATE	3. REPORT TYPE AND DATES COVERED
	31December 2003	Final Report, 30 Aug 00 - 30 Aug 03

4. TITLE AND SUBTITLE	5. CONTRACT NUMBERS
Development of a Flexible Molecular Photocell with up to 20% Conversion Efficiency	F61775-00-C0003
6. AUTHOR (S): K.R. Thampi and M. Graetzel, PhDs.	
7. PERFORMING ORGANIZATION NAMES (S) AND ADDRESS (ES) Laboratory of Photonics and Interfaces (LPI) Institute of Molecular and Biological Chemistry (ICMB) Swiss Federal Institute of Technology (EPFL) CH-1015 Lausanne, Switzerland.	8. PERFORMING ORGANIZATION REPORT NUMBER
9. SPONSORING/MONITORING AGENCY NAME (S) AND ADDRESS (ES) AFRL/MLQD 139 Barnes Drive, Suite 2 Tyndall AFB FL 32403-5323	10. SPONSORING/MONITORING AGENCY REPORT NUMBER AFRL-ML-TY-2004-4517

11. SUPPLEMENTARY NOTES

12a. DISTRIBUTION/AVAILABILITY STATEMENT	12b. DISTRIBUTION CODE
Approved for public release, distribution unlimited	A

13. ABSTRACT (Maximum 200 words)

This document reports on the main activities and outputs originated under this research project over a period of 3 years. The program was targeted at first realizing a molecular photovoltaic cell based on a dye sensitized nanocrystalline semiconductor film employing a hole conductor, a conducting polymer or a polymer electrolyte reaching an AM1.5 solar-to electric conversion efficiency of at least 2.5 %, within the first 9 months itself. This milestone was achieved within 9 months by producing solid-state solar cells containing hole conductors, with 2.56% efficiency. Further, a new type of solar cell based on polymer electrolytes was also developed. A typical cell of this type showed 5.06% solar conversion efficiency. All efficiency figures were certified by NREL, USA. In the second and the third years the aims were to reach conversion efficiencies reaching 5 and 10% respectively and these targets have been achieved. Three annual progress meetings to review the progress of the project have been organized during the project duration.

14. SUBJECT TERMS	15. NUMBER OF PAGES
Molecular Photovoltaic, Dye Sensitized Nanocrystalline Semiconductor, Solar Power	55
	16. PRICE CODE

17. SECURITY CLASSIFICATION OF REPORT	18. SECURITY CLASSIFICATION OF REPORT	19. SECURITY CLASSIFICATION OF REPORT	20. LIMITATION OF ABSTRACT
Unclassified	Unclassified	Unclassified	UL

TABLE OF CONTENT

PART I SUMMARY REPORT

	Page no
1. Key Results and Findings in 2000 – 2002	**1**
1.1 Operational principle of the dye sensitized solar cell (DSC)	1
1.2 Solid hole conductor based cells:	2
1.3 Cell Design	5
1.4 Design, Synthesis and Application of Hydrophobic Polypyridyl Photosensitizers	6
1.5 Development of ionic liquids and Polymer electrolytes	7
1.6 Development of Panchromatic Sensitizers	9
1.7 Calibrated cell efficiency measurements	10
2. Major research advances in 2003	**16**
2.1 The use of self-assembly facilitating agents	17
2.2 Improving the quality of the TiO_2 nanocrystals	19
3. Future work	**21**
3.1.Development of new panchromatic sensitizers.	21
4. Meetings, Visit, Conferences	**22**
5. Publications	**22**

PART II DETAILED REPORT

A. Dye sensitized Solid State Cells, General Procedures and Specific Details on Organic Hole Conductors	
A.1 Introduction and Presentation of the Device Structure	**24**
A.2 Device Preparation Procedures	**33**
A.2.1 Materials	33
A.2.2 General Device Assembly	34
A.2.3 Conclusions of the procedures outlined in section A.2	43
B. Dye Sensitized Cells Based on Solid Electrolytes	**45**
B.1 Device structure	**45**
B.2 Performance optimization	**46**
B.2.1 TiO2 particle synthesis,_Preparation of 18-nm-Sized TiO_2 Colloid.	46
B,2.2 Paste preparation for flexible solar cell	47
B.2.3 Sensitizer preparation	48
B.2.4 Electrolyte preparation	49
B.2.5 Preparation of counterelectrodes	49
B.2.6 Assembly of flexible cells	54

ANNEX 1 and ANNEX 2 give further procedural details

PART I: SUMMARY REPORT

Executive Summary:

The EPFL - USAF solar cell project commenced in July 2000. This report covers briefly the main activities and outputs originated under this research project over the last three years. The project started with a pre-performance meeting in August 2000. In addition to the project finance allocated by USAF, fund matching has been obtained from the EPFL administration in order to augment our research capabilities required for this project. The program was targeted at first realizing a molecular photovoltaic cell based on a dye sensitized nanocrystalline semiconductor film employing a hole conductor, a conducting polymer or a polymer electrolyte reaching an AM1.5 solar-to electric conversion efficiency of at least 2.5 %, within the first 9 months itself. This milestone was achieved within 9 months by producing solid state solar cells containing hole conductors, with 2.56% efficiency. Further, a new type of solar cell based on polymer electrolytes was also developed. A typical cell of this type showed 5.06% solar conversion efficiency. All efficiency figures were certified by NREL, USA. In the second and the third years the aims were to reach conversion efficiencies reaching 5 and 10% respectively and these targets have been achieved. Three annual progress meetings to review the progress of the project have been organized during the project duration.

1. Key Results and Findings in 2000 – 2002

1.1 Operational principle of the dye sensitized solar cell (DSC)

Figure 1 shows the operational principle of a dye-sensitized photovoltaic cell. A sensitizer attached to the surface of a nanocrystalline TiO2 film serves to harvest solar light. Upon excitation it injects an electron in the conduction band of the semiconductor oxide. The electrons migrate across the nanoparticle network to the current collector (anode). They pass subsequently through the external circuit where they perform electrical work to the counter-electrode (cathode). A redox mediator contained in a solid electrolyte, or a hole conductor serves to regenerate the sensitizer and transport the positive charges to the counter-electrode, where they recombine with the electrons. Overall, there is no net chemical change under solar exposure, light being converted to electric power through this regenerative molecular photovoltaic system.

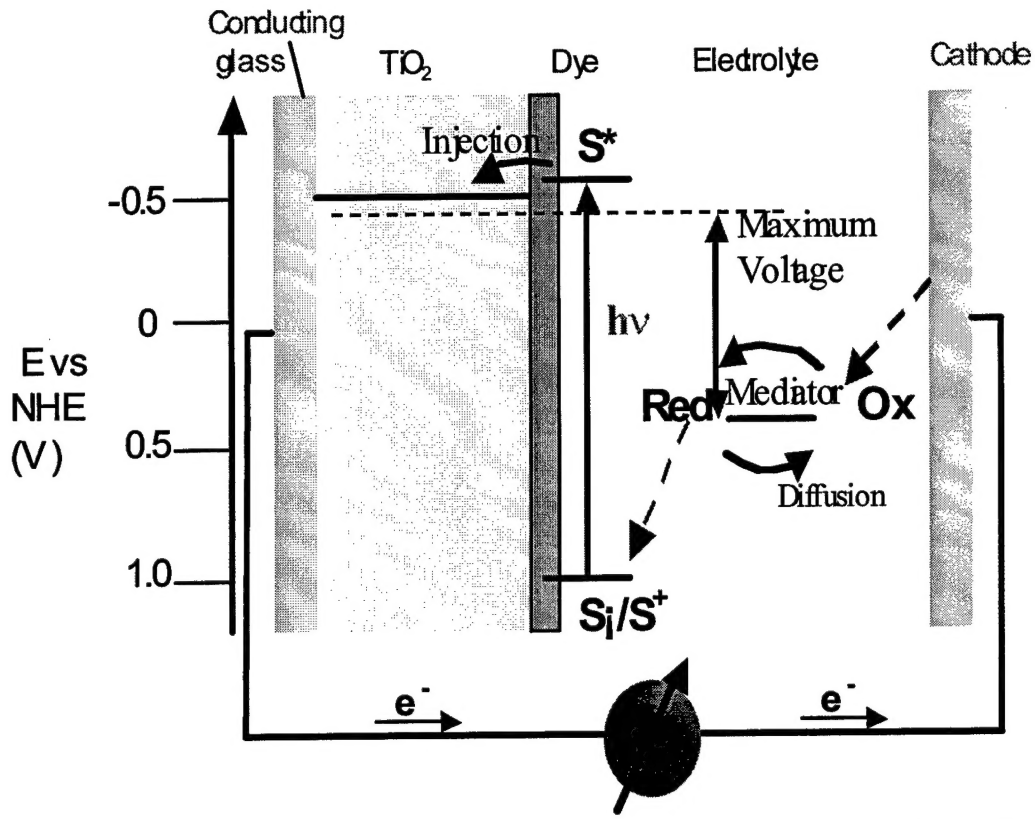

Figure 1. Schematic illustration of the operational principle of the dye-sensitized solar cell.

1.2 Solid hole conductor based cells:

The hole conductor selected for these studies is the spiro-connected triarylamine whose structure is shown in Figure 3. The hole mobility of this material is $2x10^{-4}$ cm^2/Vs. and the work function is 4.9 eV. A systematic study of the solid hole conductor based system was undertaken to improve the performance of the photovoltaic cell. In these investigations the standard N3 dye, i.e cis-Ru(SCN)2L2 (L=2,2'-bipyridyl-4,4'-dicarboxylate) or the deprononated version (coded N-719), where two of the carboxylic acid protons are replaced by tetrabutylamonium ions were employed as sensitizesr. The surface treatment with tert.butyl pyrididine and the addition of lithium bistriflylimide turned out to be advantageous to decrease substantially the electron – hole recombination rate. In this fashion it was possible to extend the diffusion length of the charge carriers to about 4 microns. Though impressive this is still a factor of 6 – 8 smaller than the charge carrier diffusion length observed in solid electrolyte based flexible solar cells. The shorter diffusion length limits the TiO2 film thickness that can be used in solid-state hole conductor cells to 2 –3 micron. This is not enough to ascertain efficient light harvesting by the surface adsorbed sensitizer explaining the relatively low photocurrents observed so far with these cells.

Figure 3 summarizes the salient features for the dynamics of the charge carrier generation, transport and recombination processes in this system. These parameters were determined by time resolved laser studies with time resolution down to the Femtosecond regime. In addition impedance analysis was carried out on complete cells using intensity modulated photocurrent

(IMPS) and intensity modulated photovoltage (IMVS) spectroscopy The electron injection from the excited dye into the oxide semiconductor and the subsequent regeneration of the sensitizer by electron donation from the hole conductor are extremely fast processes occurring in the femto- to picosecond time domain. On the other hand the charge carrier diffusion and recombination take place on a much slower time scale, i.e. within milliseconds.

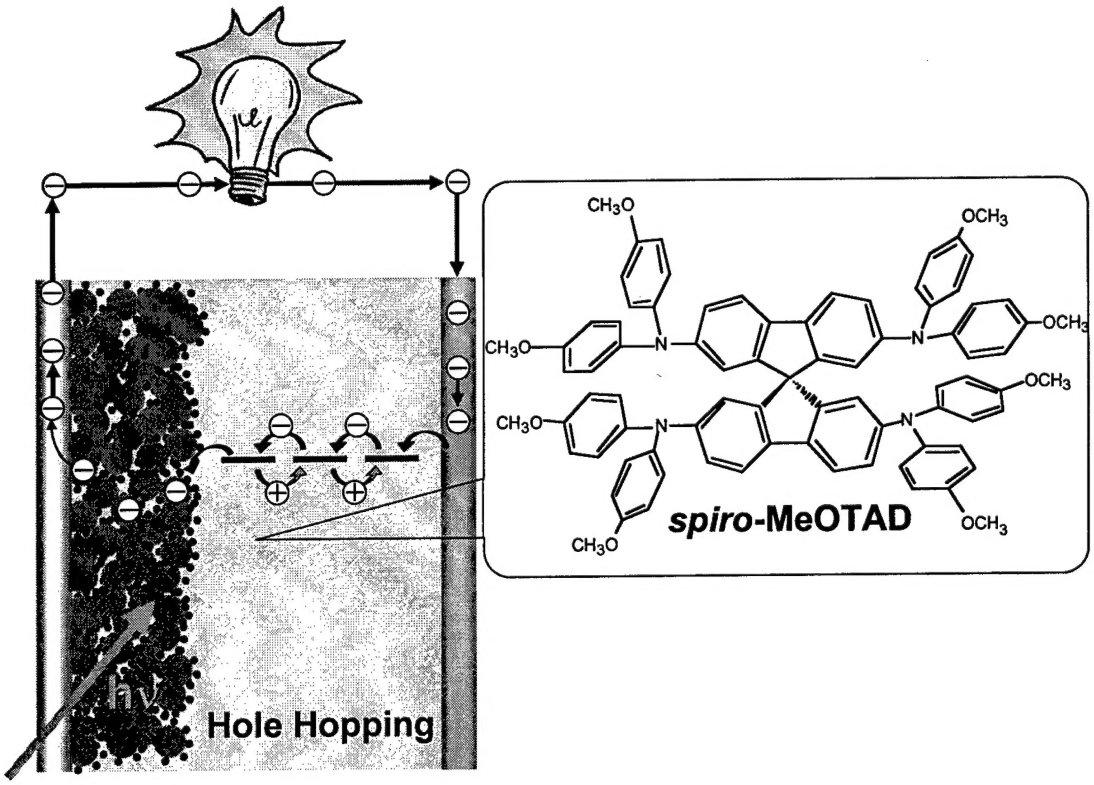

Figure 2. Structure of the molecular hole conductor employed during the first phase of the project for solid state sensitized hetero-junction solar cells.

Apart from minimizing the recombination losses we have investigated the effect of different dopants on the solar cell performance. During the start of the project, $(NPhBr)_3SbCl_6$ was employed to dope the hole conductor via generation of MeOTAD cation radicals, which serve as a charge carrier in the hole-conducting matrix. However, devices containing the doubly oxidized *spiro*-MeOTAD$(PF_6)_2$ as a dopant instead of $(NPhBr)_3SbCl_6$, showed better long term stability and were used during subsequent investigations

Using silver ions to assist the self assembly of the N3 dye on the TiO_2 it was possible to push the overall conversion yield The photovoltaic device parameters measured under full air mass 1.5 solar light were as follows: open circuit photovoltage (Voc) = 0.93 V, short circuit photocurrent (isc) = 3.6 mA/cm2 and fill factor (ff) = 0.72. This corresponds to an overall conversion efficiency of 3.2 %, which presently is still a record for this type of solid state solar cells.

While the Voc value of 0.93 V is impressively high, the photocurrents obtained with the hole conductor cells are still about a factor of four smaller than those achieved with solid

electrolyte or gel electrolyte based cells. The main reason for this is that for the former the charge carrier diffusion length is smaller than the film thickness needed to ascertain efficient solar light harvesting. Further improvement is of this type of device is possible but depends on the availability of hole conductors having a higher mobility than the spiro-MeoTAD compound employed in this investigations. Recently, new polymers and dendrimeric materials have become available, whose hole mobility is in the 10-3 cm2/Vs range and whose work function matches is close to 5 eV. These very interesting charge transport materials will be examined during future studies.

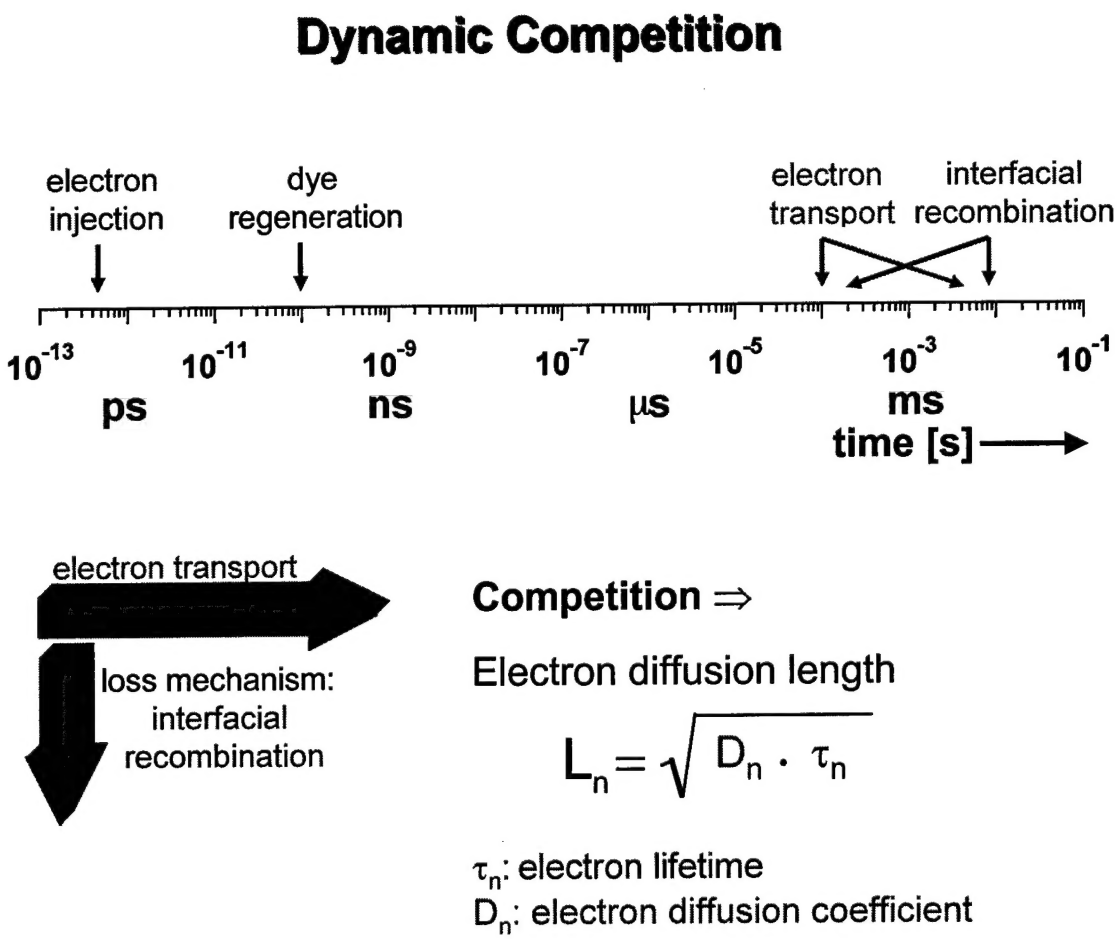

Figure 3. The time scale for charge carrier generation transport and recombination in solid state hole conductor photovoltaic cells.

1.3 Cell Design:

During the first project period, the basic cell design has been modified and further up-scaled from 0.16 cm^2 to 1.08 cm^2. This first design developed for solid hole conductors based cell is

shown in Figure 4. It allows the solid state cell to be sealed and it also has an optimised current collection technique aided by two collecting strips. These collectors are made of screen printed silver layers. It should also noted that the performance of flexible cells can more or less be predicted by measuring a glass based dye sensitised solar cell under illumination from the back side. The flexible solar cell performance may fall below this prediction only when poorly transmitting or conducting polymer films are used as the counter (transparent) electrode. Since the fabrication of a glass based cell is much faster and easier when done in a laboratory, routine measurements to study the effect of various cell parameters were done by fabricating hundreds of small glass cells. The performance of such combinations have been later verified by fabricating flexible cells.

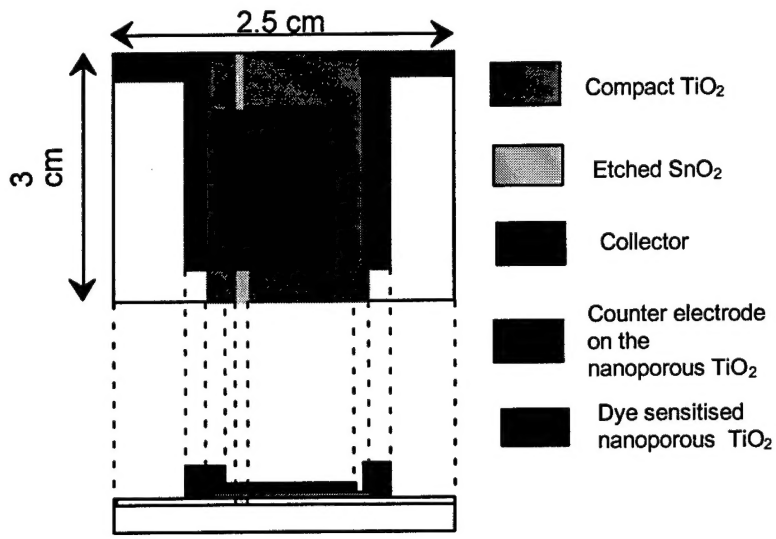

Figure 4: Outlay of the solid hole state conductor cell based on a sensitized mesoporous heterojunction.

The flexible embodiment of the hole conductor or solid electrolyte cell is shown in Figure 5. It employs a thin titanium foil instead of the conducting glass as the current collector that supports the dye-derivatized TiO_2 nanocrystals. The deposition of the compact underlayer of TiO2 is not necessary for this device since a blocking layer of TiO2 is spontaneously formed by oxidation of the titanium foil. The counter electrode in this case is a transparent conducting plastic film.

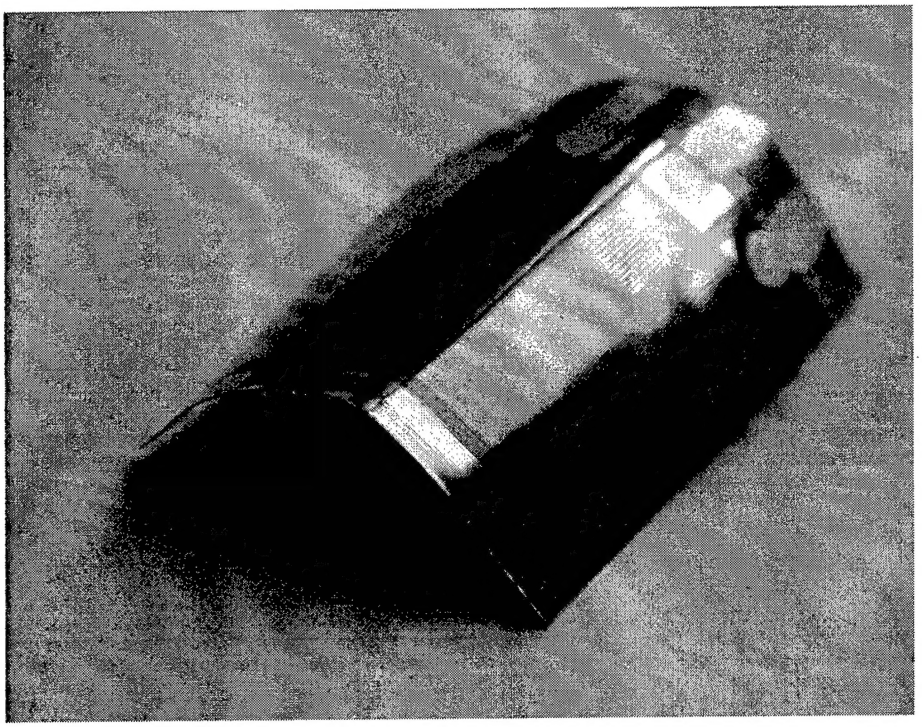

Figure 5. Photograph of a flexible and light-weight embodiment of a solid state dye sensitized solar cell.

1.4 Design, Synthesis and Application of Hydrophobic Ruthenium Polypyridyl Photosensitizers

In an effort to reduce the sensitivity of the solar cell towards water and improve the local order in the adsorbed dye monolayer a new series of amphiphilic heteroleptic ruthenium(II) sensitizers has been synthesized. Being hydrophobic, these sensitizers do not desorb from the surface of the mesoporous TiO_2 film in the presence of water. Tolerance of water is of great advantage for practical applications of flexible and light-weight solar cells. The plastic material used for the cover electrode is water permeable. Hence any interference of moisture with cell performance is expected to be detrimental for photovoltaic stability.

The structures for the hydrophobic heteroleptic ruthenium(II) sensitizers examined during our study are shown in Figure 6. $[Ru(H_2dcbpy)(mhdbpy)(NCS)_2]$ **(1)**, $[Ru(H_2dcbpy)(dnbpy)(NCS)_2]$ (**2** coded **Z907**), and $[Ru(H_2dcbpy)(mddbpy)(NCS)_2]$ **(3)**, have been fully characterized (where the ligands H_2dcbpy = 4,4'-dicarboxy-2,2'-bipyridine, mhdbpy = 4-methyl,4'-hexadecyl-2,2'-bipyridine and dnbpy = 4,4'-dinonyl-2,2'-bipyridine , mddbpy= 4-methyl,4'-didodecyl-2,2'-bipyridine).

Of the hydrophobic heteroleptic ruthenium(II) sensitizers described above the complex Z907 has shown the greatest promise so far. When anchored to nanocrystalline TiO_2 films from dimethylformamide solutions it yields close to 90% incident photon to current conversion efficiencies in a broad wavelength range in the visible corresponding to short circuit currents

of 18 – 19 mA/cm^2. Solar cells containing these new hydrophobic sensitizers show excellent stability both under thermal stress for 1000 hours at 80 – 85 °C and when submitted to light soaking under full sun at 55 – 60 °C.

A.1.5 Development of ionic liquids and Polymer electrolytes:

A new type of solid polymer electrolyte based on an ionic liquid has been developed during the reporting three-year project period. The ionic liquid is composed of N-methyl-N-propyl imidazolium cations and a mixture of iodide/triiodide anions. The latter serve as the redox mediating conducting matrix. The copolymer polyvylinidene fluoride/hexafluoropropylene (PVDF-HFP) whose structure is shown below was used to solidify the ionic liquid. In some cases an organic plastifying agent, such as methoxypropionitrile and a solid buffer, such as N-methylbenzimidazol were added to the mixture. These new solid polymer electrolytes were found to display very remarkable properties. Thus, the diffusion of the redox-active ioidide and triiodide anions was found to be much faster than expected from the high viscosity of the ionic liquids. This was attributed to the occurrence of Grothus-type exchange mechanism to which enhances the charge movement in the redox melt. These fluoro-polymer solid electrolytes were mainly studied in the second and third year of the project and have great potential for practical applications of the flexible solar cell.

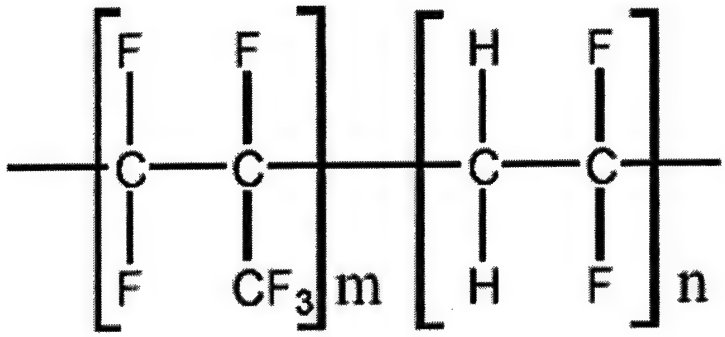

Structure of the PVDF-HFP copolymer

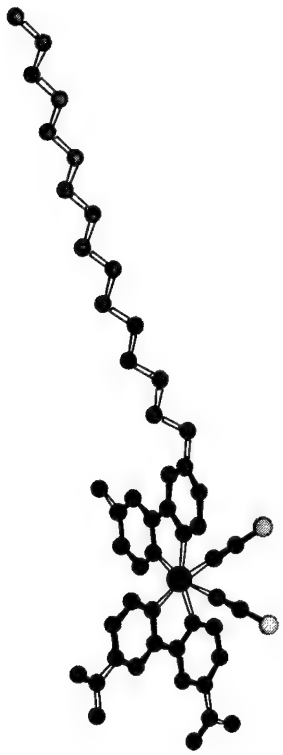

Complex **1**

Complex **2**

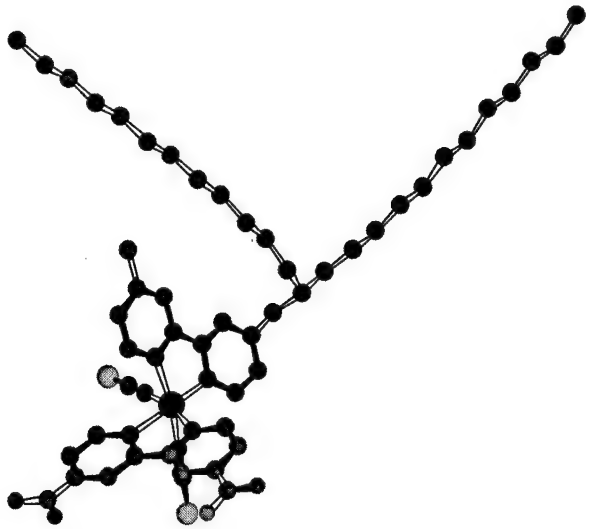

Complex **3**

Figure 6. Structure of the heteroleptic hydrophobic ruthernium complexes **1**, **2** and **3**, The complex 2 (Z907) has so far shown the best perfomance of these hydrophobic dyes.

1.6 Development of Panchromatic Sensitizers

We have developed new tetradentate ligands containing donor and acceptor groups and its ruthenium complexes (Figure 7), which show enhanced IR response to capture the near IR regionm of the sunlight. Figure 8 compares the absorption spectrum of a typical representative of this class of panchromatic dyes to that of the standard sensitizer. These substituted tetradentate ligands tune metal t_{2g} orbitals enhancing the spectral response in the visible and near IR region. The spectral properties of these new sensitizers are further adjusted by introducing nonchromophoric ligands such as Cl^-, NCS^-, CN. The panchromatic ruthenium complexes were used as sensitizers for solar energy conversion. A preliminary results using the *trans*-[Ru(L)$(NCS)_2$] complex, show 75% incident photon-to-current efficiencies (IPCE), yielding 18 mA/cm^2 photocurrent density under standard AM 1.5 sunlight. However the photovoltage for these panchromatic sensitizers is only 650 mV, which resulted in overall lower efficiency compared to the standard dyes. The most likely reason for such low open circuit potential is the lower LUMO of the quaterpyridyl ligands as compared to the standard N3 sensitizer. In other words, the extension of the spectral response into the near IR was gained at the expense of shifting the LUMO orbital to lower levels from where charge injection into the TiO_2 conduction band is significantly impaired. To overcome this problem we have designed new tetradentate ligands (shown in figure 8), containing oxygen and nitrogen linkers that break the conjugation of quaterpyridyl ligands that shifting the LUMO more negatively.

The role of non-chromophoric ligands such as thiocyanato is to tune the metal t_{2g} orbitals of ruthenium(II) and possibly to stabilize the hole that is being generated on the metal, after having injected an electron into the conduction band. In order to tune further the metal t_{2g} orbitals and separate the hole more efficiently from the ruthenium center we have engineered at the molecular level and designed new donor ligands, which will be used in panchromatic sensitizers as well in our standard dyes N719 and Z907.

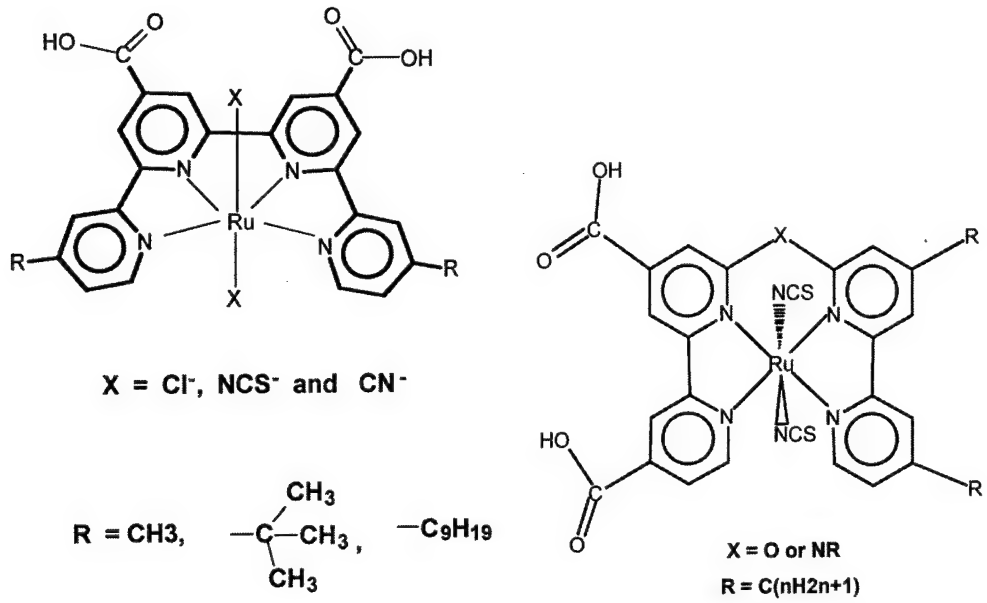

Figure 7 : Tetradentate ligands and its ruthenium complexes.

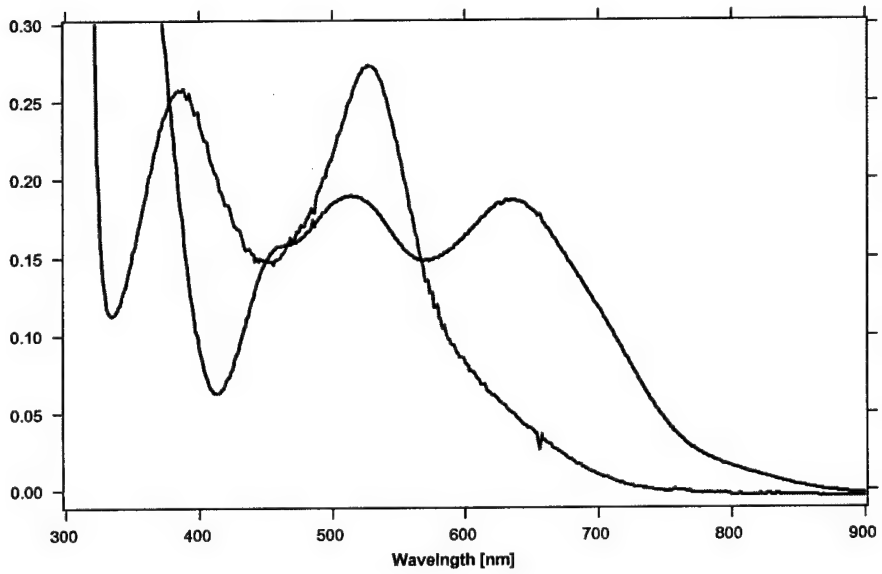

Figure 8: Comparison of UV/Vis Absorption Spectra of N719 and the panchromatic sensitizer shown on the left side of Figure 7 where X = NCS.

1.8 Calibrated cellefficiency measurements:

Great care was taken during the whole project period to perform cell efficiency measurements under the well defined conditions standard conditions, i.e. air mass 1.5 (AM 1.5) global solar

radiation and a temperature of 25 °C. Our own measurements were repeatedly verified by the photovoltaic calibration at NREL. Excellent agreement was always found the deviations between the two measurements being less than 2%.

By the 9th month of the program, the milestone of 2.5% solar conversion efficiency at AM 1.5 condition set for the solid state hole conductor device, has been surpassed. The results clearly established an efficiency of 2.56% in full Sun (AM 1.5), with a solid hole conductor cell. In addition to our own measurements, cells have been also taken to NREL in USA for independent measurement and certification. Figure 9 shows a typical I-V curve of a hole conductor based cell measured in EPFL. Figure 10 shows the corresponding data from NREL. Figure 11 and 12 show results of a cell with polymer electrolyte (active area = 0.78 cm^2) measured at NREL under 1.5 AM sun conditions. This cell showed 5.06% solar conversion efficiency.

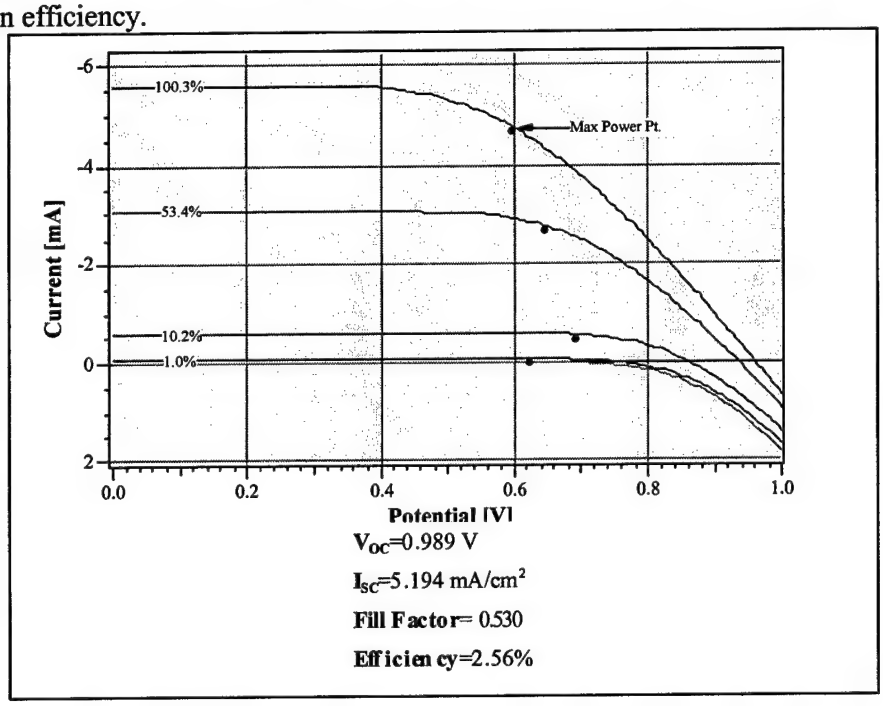

Figure 9. A typical I-V curve of a hole conductor solar cell, measured in LPI-EPFL. The cell area = 1.07 cm^2; 1.5 AM sunlight conditions; dye : N719; Charge transfer material in the spin coating fluid contains: spiro-MeOTAD (0.2M); $(NPhBr)_3SbCl_6$: 4.2×10^{-4} M ; t-butyl pyridine: 0.8M; Li triflate: 26mM; solvent : chlorobenzene. All liquids have been removed by vacuum drying. counter electrode: Au; NSG-SnO_2:F^- glass (8 ohms.cm).

Figure 10. I-V curve measured at NREL, USA, for the same cell shown in Figure 5.

EPFL

solid nano-crystal Cell

Device ID: 2303 #13
Mar 28, 2003 2:56 PM
Reporting Spectrum: AM1.5 Global

Device Temperature: 25.0 ± 1.0 °C
Device Area: 0.778 cm²
Irradiance: 1000.0 W/m²

NREL X25 IV System
PV Performance Characterization Team

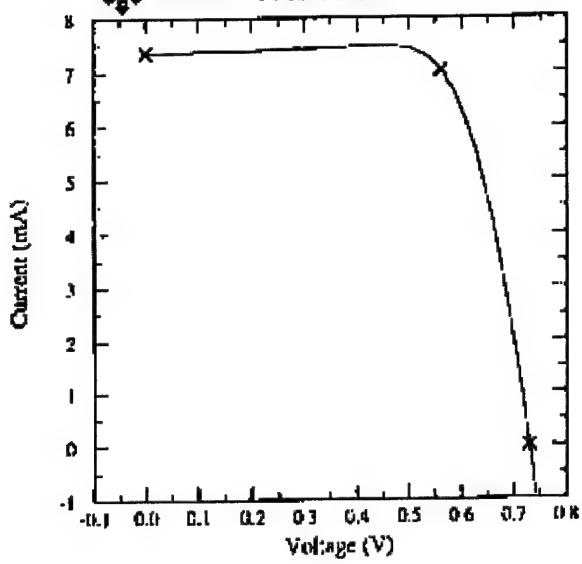

V_{oc} = 0.7295 V
I_{sc} = 7.3607 mA
J_{sc} = 9.4656 mA/cm²
Fill Factor = 73.23 %

I_{max} = 7.0185 mA
V_{max} = 0.5607 V
P_{max} = 3.9354 mW
Efficiency = 5.06 %

Fast. Forward to Reverse
Capacitive charging"

Figure 11. I-V curve of a 5.06% efficient polymer electrolyte solar cell, measured by NREL.

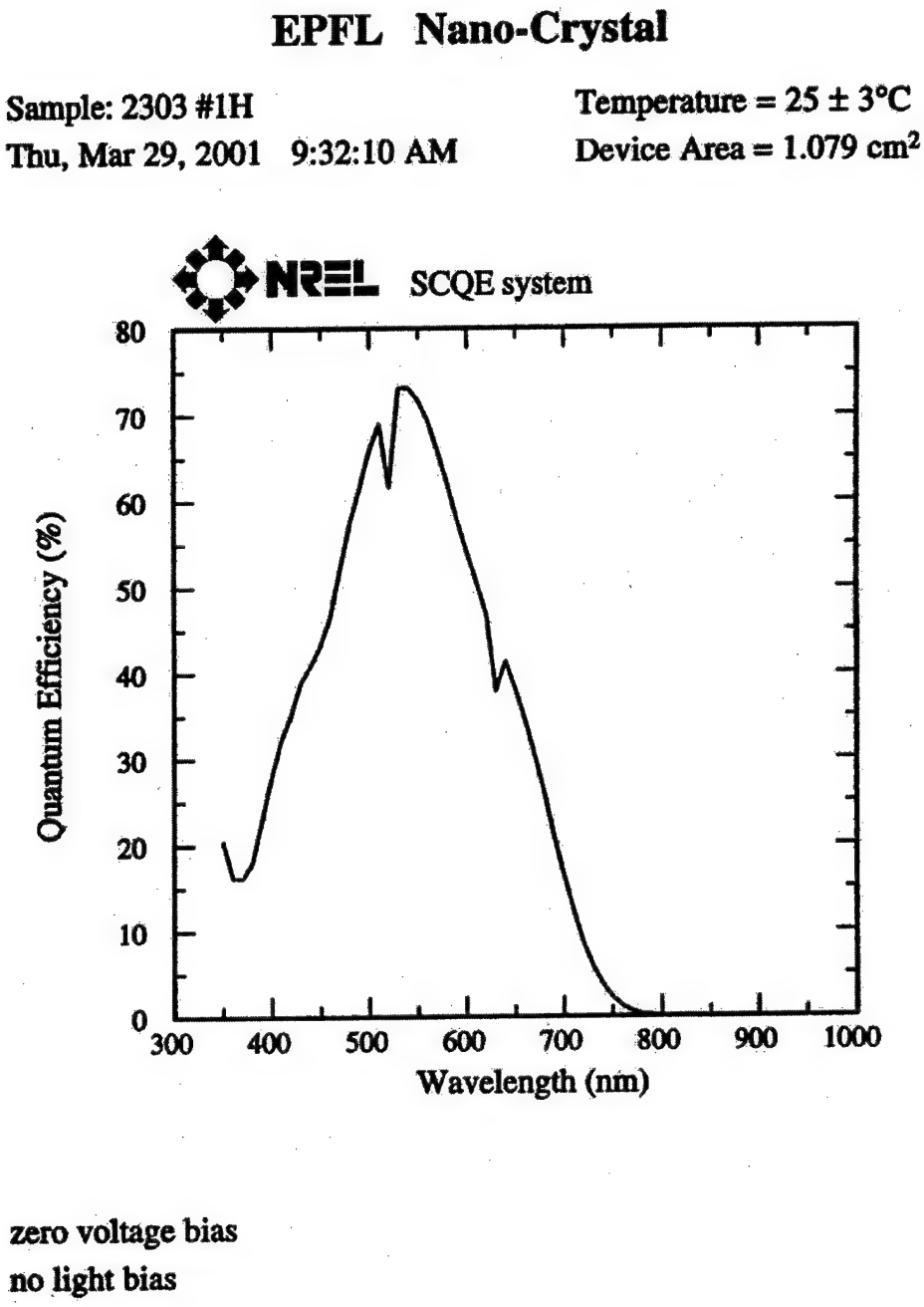

Figure 12. IPCE spectrum of the polymer electrolyte cell.

During this period, we learned also that certain types of hole conductor cells temporarily decreased slightly their short circuit current up on storing them in dark for several days. A systematic study has revealed that the performance of such cells can be regained by re-exposing them to AM 1.5 simulated sunlight. Such experiments have been conducted with cells stored up to 25 days in darkness. In all cases, we have noticed that the drop in cell efficiency caused by storing cells under darkness was regained by a short exposure to sunlight. It is worth noticing that, in most cases, the small drop in short circuit current density is compensated by an improved OCV.

By tuning the electrolyte composition, TiO_2 layer thickness and its porosity and beneficially making use of the cell's UV activation process, we could reach close to 5% solar conversion efficiency, by early March 2002. A typical set of this data is presented in Table 1 shown below, exceeding the 5% efficiency milestone.

Table 1: Flexible Solar Cell Measurements
TiO_2 layer: transparent layer; porosity 70%; 12 - 13 □m thick layer on polished Ti foil
Electrolyte: Z 95 (65% PMII, 0.1 M I_2; 0.45 M NMB and 35% valeronitrile)
Dye: Z 907 (in mixed solvent: acetonitrile: t-butanol = 1:1)
Seal: special O-ring type gasket (13 □m)

Time	**0th day**	**1 day (dark)**	**2 days (dark)**	**3 days (dark)**	**45 min ST***
OCV, mV	605	632	640	643	655
I_{sc}, mA/cm^2	10.9	10.9	10.8	10.9	11.5
F.F.	0.682	0.704	0.711	0.709	0.697
Efficiency %	4.50	4.83	4.94	4.95	**5.26**

* ST = Illumination for a brief period under simulated sunlight using Suntest lamp, at 55°C.

An example of a current voltage curve obtained at NREL during the measurements on July 17, 2002 is shown in Figure 9. The conversion efficiency obtained was 5.4 %. Subsequent spectral response measurements carried out by NREL showed the yields to be underestimated due to spectral mismatch. After correcting for the spectral mismatch the efficiency figure is 5.7 %, well over the 5% limit that was imposed by the milestone. We studied also the beneficial effect of UV and visible light soaking on the cell efficiency .
Size scale up of cells and fabrication of devices for demonstration purposes has been also undertaken in this project. The main aims were:

-increasing the active solar cell area without compromising on its output.
-designing a larger area solid state cell with the possibility of sealing it against ambients and.
-designing a solid new solid polymer electrolyte based on ionic liquids and fluorinated polymers as gel forming agents.

Following the request expressed by the of USAF representatives at the review meeting in Lausanne in May 2002, a scaled up version of the flexible cells were produced to serve as demonstration cells for the Air Force contractor. Instead of the 0. 5 - 1 cm^2 sized devices produced in the first 2 years of the project, a cell design with an active area of over 2 cm^2 was developed and several cell samples were produced and supplied.

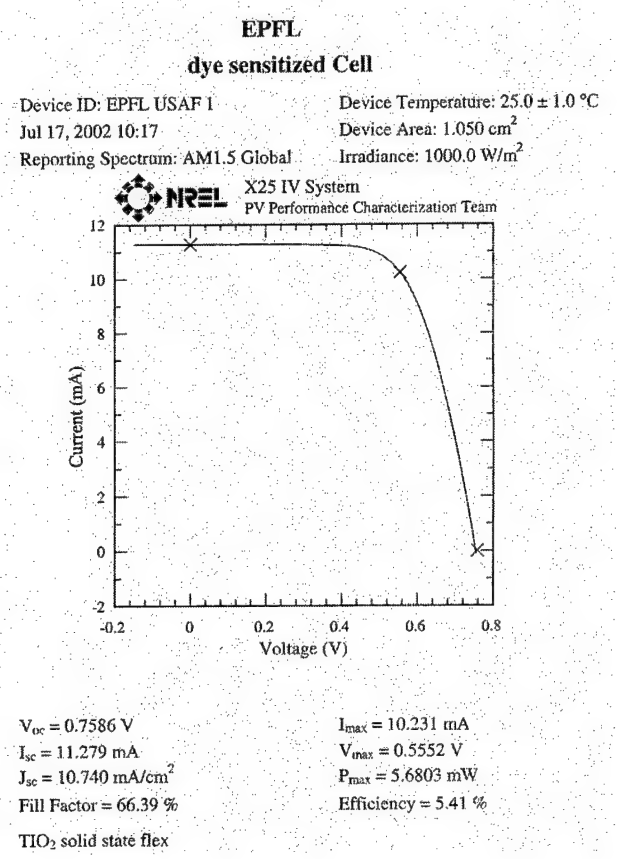

Figure 12: Example of a photo-current voltage curve of a solid state dye sensitized flexible solar cell tested at NREL.

2 Major research advances in 2003

During the year 2003, the focus of research in LPI-EPFL is set on improving the DSC conversion efficiency to higher conversion efficiency targets. This involved making new and better dyes, electrolytes, TiO_2 layers and developing better cell fabrication protocols. In this line of action, by January 2003, EPFL could already produce glass based cells of 1.98 cm^2 area showing 8.07% solar conversion efficiency. This was achieved by using a mono-proton N719 dye, modified electrolyte and a 16□m thick double layer of TiO_2 (12 + 4 □m). In February 2003, a modified dye coded N719-1.5H^+ was also tested. By adjusting the number of protons in the dye, it was possible to modulate the current density and OCV to optimum values. While this optimization of the proton content of the dye and the lithium iodide concentration of the electrolyte allowed augmenting the conversion efficiency to 8.23%, it became clear that the system based on the red dye N-719 and the 1376 electrolyte was approaching its performance limits. In order to make further significant gains in cell efficiency, more profound alterations in this molecular photo-conversion system were needed that would allow to increase substantially the open circuit photo-voltage and short circuit photocurrent of the device. Fortunately we have been able to make substantial progress in both areas, which will now be outlined in more detail.

2.1 The use of self-assembly facilitating agents to increase the open circuit photovoltage of the photovoltaic cell.

The ruthenium dye N-719 i.e. *cis* –RuL2(SCN)2 (L= 2,2-bipyridyl- 4,4'dicarboxylate) is adsorbed at the TiO2 surface *via* 2 of the 4 carboxylate groups. The spatial configuration of the adsorbed dye at the (111) oriented surface of the TiO2 nanocrystals has been assessed by FTIR analysis and molecular dynamics calculation. The dye monolayer is disordered and the lateral repulsion of the negatively charged dye molecules is attenuated by spontaneous co-adsorption of counter ions. It is desirable to increase the order of the dye monolayer at interface and render it denser. The goal is to make the dye layer insulating in order to block the dark current at the interface. The resulting gain in open circuit voltage can be calculated from the diode equation:

$$\mathbf{V_{oc} = (nRT/F)\ ln[(i_{sc}/i_o) -1]} \quad \mathbf{(1)}$$

where n is the ideality factor whose value is between 1 and 2, i_o is the reverse saturation current and R and F are the ideal gas and Faraday's constant. Using for the ideality factor of the dye sensitized solar cell a value of 1.5, the reduction of the dark current by a factor of 10 would result in a voltage increase of 90 mV boosting the conversion efficiency of the cell by at least 15 %.

We have recently discovered a number of agents, which when used as co-adsorbents facilitate self- assembly of the N-719 dye at the TiO2 oxide surface rendering it more impermeable and reducing in this fashion the dark current of the cell. Some representative structures for such self-assembly facilitating agents, which are presently under evaluation, are shown below:

APA

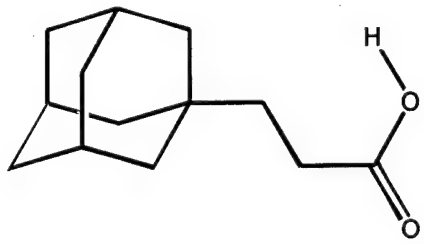

DPA

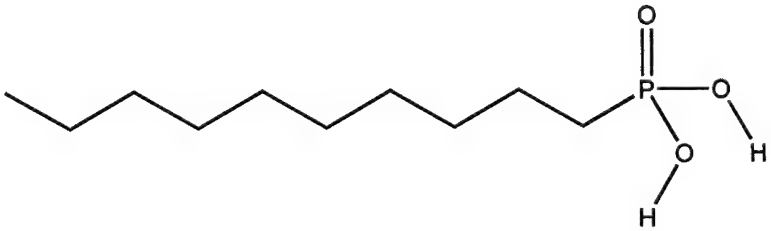

PBOC

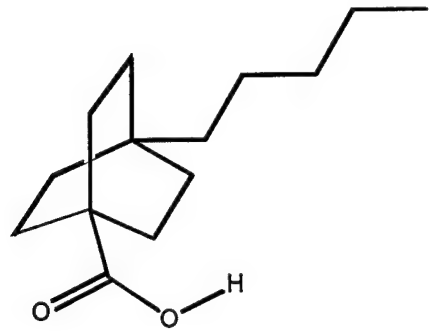

Apart from these carboxylic and phosphonic acids we have also investigated several cationic species. Amongst those, guanidinium thiocyanate, has shown the most promising results so far. Replacing the LiI in the standard 1376 electrolyte by 0.1 M of guanidinium thiocyanate reduces the dark reduction current at the mesoporous TiO2 electrode, measured at - 0.7 V polarization against the counter electrode, by a factor of 8 –10. As a result, the cell voltage and the overall efficiency of the device increases substantially.

A typical performance obtained with guanidinium thiocyanate assisted self-assembly of the N-719 sensitizer is summarized in Figure 13 The photocurrent action spectrum shows incident photon to current conversion efficiencies exceeding 80% in the 450 to 600 nm wavelength range which is close to the absorption maximum of the dye. The cell showed a short circuit photocurrent of 16 mA/cm^2, an open circuit voltage of 805 mV and a fill factor of 0.732, corresponding to an air mass 1.5 (1000 W/m^2) solar to electric power conversion efficiency of 9.43 %. These data were measured without any antireflective coating. Using an antireflective coating increased the overall conversion efficieny to 9.8%.

Photocurrent action spectrum obtained with 719 sensitizer

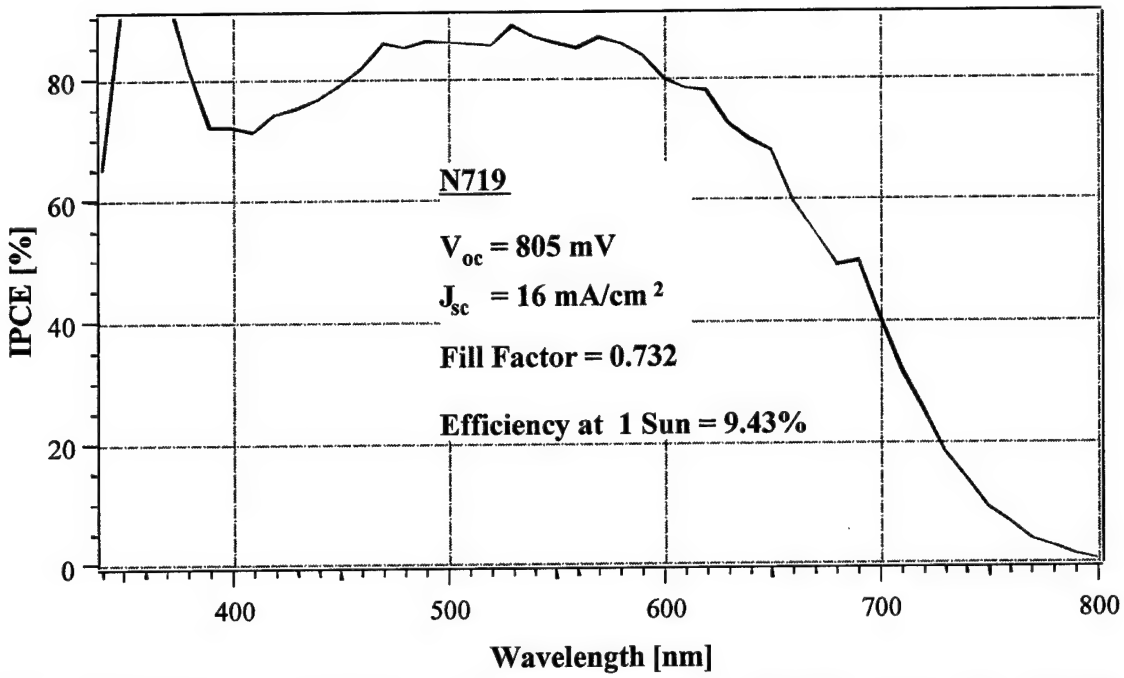

Figure 13: Photocurrent action spectrum and photovoltaic performance of a dye sensitized cell whose performance wasenhanced by using guanidinium thiocyanate as self assembly assisting agent.

2.2 Improving the quality of the TiO_2 nanocrystals

The cell performance has been further improved by judiciously increasing the total TiO_2 layer thickness to 21 □m and modifying the basic particle size of the thick layer to 20nm. The 21□m layer is made up of a 16□m layer of 20 nm-sizedTiO_2 and a 5□m thick scattering layer. This combination significantly improved the cell yield and the typical results are provided below in Figures 14 and 15. Figure 16 shows a typical flexible dye sensitized solar cell under operation.

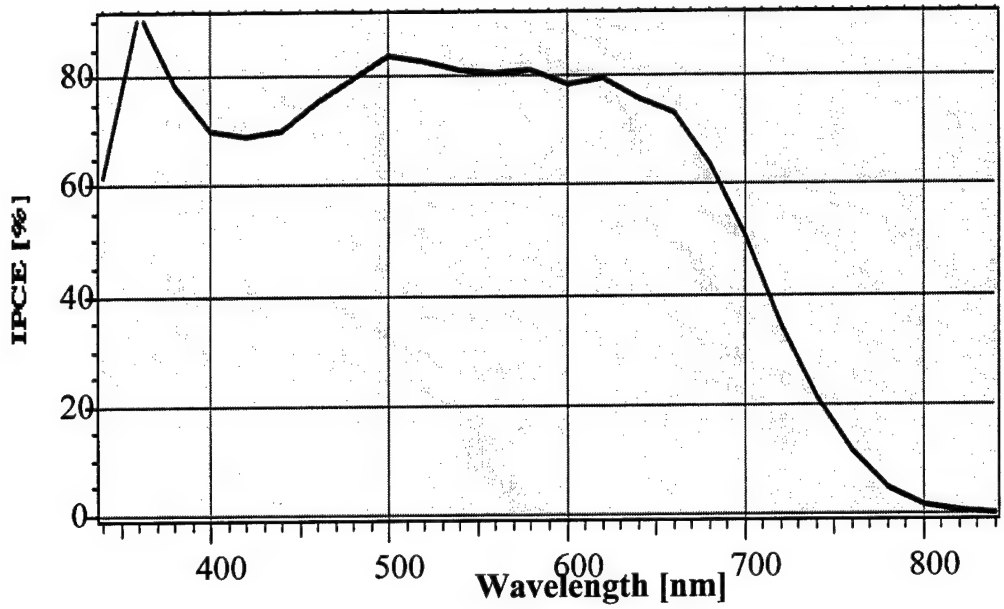

Figure 14: Photocurrent action spectrum obtained with the N719 dye attached to a 16 + 5 μm nanocrystalline TiO_2 film. The incident photon to current conversion efficiency is plotted as a function of the wavelength of the exciting light. The IPCE of this cell is 83% and the short circuit current density is 16.9 mA/cm^2, at AM1.5 (1000 W/cm^2) illumination.

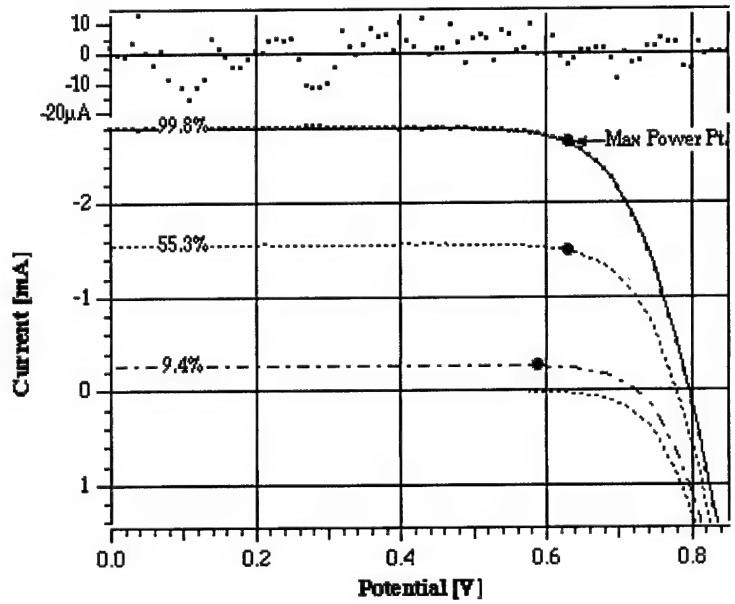

Figure 15: I-V curves of the solar cell which showed excellent performance: OCV = 795.65 mV; 17.77 mA/cm^2; Fill Factor = 0.748 and Conversion efficiency = 10.58%.

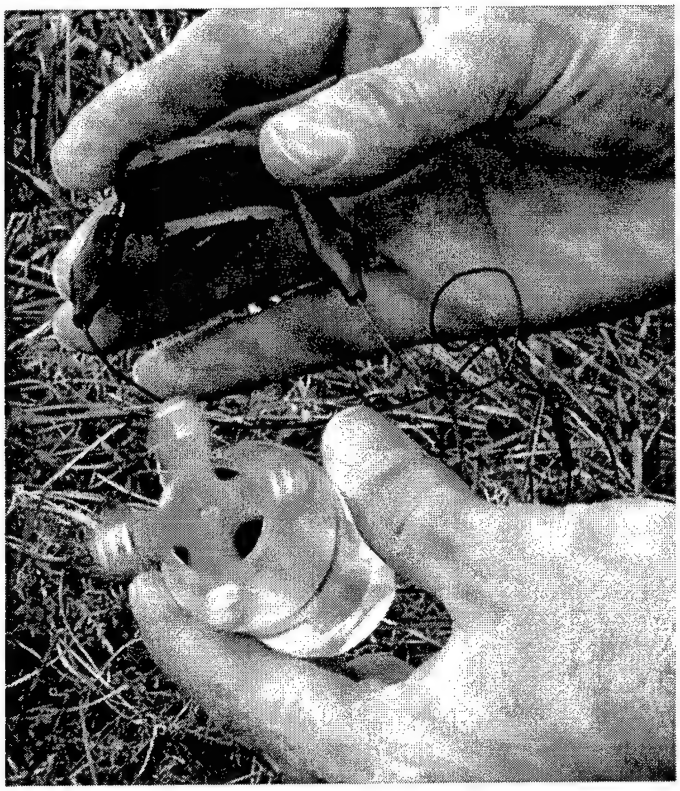

Figure 16: A flexible dye sensitized solar cell under sunlight operation.

3 Future work

Work in the near term will focus on reaching the 12 % efficiency limit, which is the first milestone for the continuation project.

3.1.Development of new panchromatic sensitizers.

While improvements in performance have been obtained recently using self-assembly assisting agents are remarkable it will be very difficult to achieve efficiencies much beyond 11% with the standard N-719 sensitizer unless the redox system is changed. Alternatively if the present iodide based redox system is maintained, introducing panchromatic sensitizers can boost the efficiency of cells further. To give 15 % conversion efficiency, these should be designed to yield at least 24 mA/cm2 short circuit current under full sunlight and fill factor as well as open circuit voltage values similar to those that are presently obtained. The short circuit current can be calculated from the overlap integral of the solar emission with the phototocurrent action spectrum of the cell as shown in the scheme below.

Overall Solar to Electric Power Conversion Efficiency (AIR MASS 1.5 SUNLIGHT 100 mW/cm^2)

$$\eta = I_{SC}\ [mA/cm^2] \times V_{OC}\ [V] \times ff$$

$$I_{SC} = \int_0^{\infty} IPCE(\lambda)\, I_{sun}(\lambda)\, d\lambda$$

$I_{sun}(\lambda)$ = spectral intensity of solar emission

Fortunately there are candidates that fulfill the spectral and stability requirements for such panchromatic sensitizers. We have seen that the structures of tetradentate ruthenium dyes that we have developed for this purpose. We have discussed above already the strategies that has been applied in the conception of these new sensitizers having enhanced near IR response.

Work in the near term will focus on reaching the 12 % efficiency limit, which is now in very close reach.

4. Meetings, Visit, Conferences.

1. Dayton, Ohio Annual Project meeting, June 2001.
2. EPFL Lausanne, Annual USAF-EPFL project meeting May 2002.
3. EPFL, Lausanne, Annual USAF-EPFL project meeting, August 2003.

5. Publications

(1) A remarkably stable quasi-solid-state dye-sensitized solar cell based on an amphiphilic ruthenium sensitizer and a polymer gel electrolyte,
Peng Wang, Shaik M. Zakeeruddin, Jacques E. Moser, Md. K. Nazeeruddin, Takashi Sekiguchi and Michael Grätzel, *Nature Mater*, **2003**, 2, 402- 407.

(2) Investigation of Sensitizer Adsorption and the Influence of Protons on current and voltage of a Dye SensitizedNanocrystalline TiO2 Solar Cell,
Md. K. Nazeeruddin, R. Humphry-Baker, P. Liska, and M. Grätzel, *J. Phys. Chem.*, **2003**, 127, 8981-8989.

(3) A Swift Dye Uptake Procedure for Dye Sensitized Solar Cells Md. K. Nazeeruddin, R. Splivallo, P. Liska, P. Comte and M. Grätzel, *Chem. Commun*, **2003**, 1456 – 1457.

(4) Conversion and Storage of Solar Energy using Dye-sensitized Nanocrystalline TiO2 Cells, Md. K. Nazeeruddin and M. Grätzel,
Comprehensive Coordination Chemistry 2, **2003**, Volume 9, Chapter 9.16, edited by M. Ward, Elsevier Science Ltd.

(5) Dye-Sensitized Solar Cells Based on Mesoscopic Oxide Semiconductor films, Md. K. Nazeeruddin and M. Grätzel, *Molecular and Supramolecular Photochemistry* Series, Volume 9, edited by V. Ramamurthy and K. S. Schanze, Marcel-Dekker, **2003**, 301-343.

PART II DETAILED REPORT ON THE EXPERIMENTS PERFORMED UNDER THE CONTRACT AND PROCEDURES USED

A. Dye sensitized Solid State Cells, General Procedures and Specific Details on Organic Hole Conductors

This chapter discusses in more detail the structure of the dye-sensitized solar cell solid-state and its key components, the photo electrode, the sensitizer, the hole transporting material, and the counter electrode. The materials required for each component are scrutinized, showing the multidisciplinary approach of this type of solar cell. Finally the kinetics of the electron transfer processes involved in the light energy conversion process is reviewed. Several of the procedures and structures discussed here apply also to the solid electrolyte cells discussed in Chapter B.

A.1 Introduction and Presentation of the Device Structure

In contrast to the sandwich design of the solid or liquid electrolyte solar cell between two glass sheets covered by a transparent conducting oxide TCOs, solid-state the sensitized heterojunction cell based on a hole transfer material posses typically a monolithic structure. Each layer is deposited on top of the other and contacts are positioned on the same substrate. In the following the key components of the sensitized heterojucntion cell will be described in more detail.

i) <u>The photoelectrode</u>
The dye-sensitized oxide is typically deposited on a highly doped, transparent conducting oxide (TCO), which allows light transmission while providing sufficient conductivity for current collection. Recently organic polymers of high conductivity deposited onto plastic foil find increasing application as substrate for flexible devices. Metal foils show conductivities superior to the TCOs and polymers. However, because of their opacity the illumination of the cell has to be arranged in this case through the counter electrode.

The surface of TCO should make a good mechanical and electrical contact with the porous TiO_2 film. From dark current measurements of TiO_2/spiro-MeOTAD it is known that the hole conductor is forming an ohmic contact with the back contact layer (SnO_2:F). To reduce dark current losses due to short circuit of electrons in the current collector with holes in the hole conductor, a thin under layer of TiO_2 is introduced between the SnO_2 layer and nanocrystalline TiO_2 layer. This thin compact layer does furthermore improve the mechanical adhesion of the porous TiO_2 film on the substrates, especially for SnO_2 layers of low haze, i.e. low surface roughness and thus less contact area.

The TiO_2 semiconductor has three functions in the dye-sensitized solar cell: it provides the surface for the dye adsorption, it functions as electron acceptor for the excited dye and it serves as electron conductor. Colloid preparation and layer deposition have been developed to optimize the TiO_2 for these functions. Most important for the performance of dye-sensitized solar cells was the development of a mesoporous semiconductor structure. This becomes evident considering the limited light capture of a dye monolayer on a flat surface. For an extinction coefficient (ε) around $1\text{-}4\times10^5$ the cross section for light absorption, given by

$$\sigma = \varepsilon \cdot 1000 \cdot \frac{\ln(10)}{N_A} \qquad (2)$$

is between 0.0038 and 0.15 nm^2. This is smaller than the area occupied by the sensitizer (1-2nm^2), i.e. only a few percent of the incoming light can be absorbed. On the other hand deposition of multilayer of dye on the surface in order to increase its light absorption is not of advantage, since outer dye layers act only as light filter, with no contribution to injection. In contrast mesoporous structures based on particles of 10-20 nm provide surface areas 1000 times larger than the apparent geometric one, depending on film thickness and porosity. The enhanced light absorption leads to a drastically improved light harvesting efficiency (LHE):

$$LHE = 1 - 10^{-A} = 1 - 10^{-\Gamma \cdot \sigma} \quad (3)$$

Where $\Gamma$is the surface coverage [molecules/cm^{-2}] of the dye coverage and σ denotes its absorption cross section [cm^2/molecule] (scattering by the film is neglected).

IntrinsicTiO_2 is an isolator that is n-doped and therefore becomes conductive by electron injection of the adsorbed dye. Electronic contact between the nanoparticle is established by sintering the nanoparticle together, enabling the entire surface-adsorbed molecular layer to be accessed electronically. The interconnection of the nanoparticle by the sintering process allows the deposition of a mechanically stable, transparent film of typically a few micron thickness. Increase of the free electron concentration in the dark is not necessary and may even be detrimental for the photo electrochemical behavior of the TiO_2.

Amongst several semiconductors studied for photo electrochemical applications, TiO_2 is by far the most commonly used, because of its energetic properties, its stability, and the Lewis acidity of the surface, which allows attachment of dyes. It is furthermore a low cost material that is widely available. TiO_2 is used in its low-temperature stable form (pyramid-like crystals) anatase, as rutile shows non-negligible absorption in the near-UV region (350–400 nm). This excitation within the band gap leads to generation of holes, which are strong oxidants and cause long-term instability issues in the solar cell.

ii) <u>The sensitizer</u>

The dye is the photoactive element of the photovoltaic device, harvesting the incident light for the photon-to-electron conversion. To be used as sensitizer for a single junction photovoltaic cell the dye must fulfill the following requirements:

- For a single junction photovoltaic cell the dye should absorb ideally all the photons of the solar spectrum below a threshold wavelength of ca 900 nm. More than 50 % of the solar energy is emitted in the region from 400 to 800 nm. A shift of the dye spectrum to longer wavelength will not yield higher energy conversion efficiencies as the loss in photovoltage is not fully compensated by the gain in photocurrent.

- The extinction coefficient of the dye should be high throughout the entire absorption spectrum, in order to absorb most of the light with a minimum quantity of dye material. Since the white light harvesting efficiency is limited by the absorption in the weaker absorbing regions, maintaining a high extinction coefficient at wavelengths different from the maximum absorption peak is particularly important.

- The excited state lifetime of the dye must be long enough to ascertain efficient electron injection. In general this requirement is not a limiting factor, as electron injection occurs on the sub nanosecond time scale and thus can compete efficiently with other excited state decay processes.

- For efficient electron injection to occur the oxidation potential of the dye excited state $\phi^0(S^+/S^*)$ needs to be more negative than the conduction band potential of the semiconductor ($\phi_{fb}=\phi_{cb}$ for nano-size particles).

$$\phi^0(S^+/S) < \phi_{cb} + \frac{\Delta E_{0,0}}{F} \quad (4)$$

Where $\Delta E_{0,0}$ is the excitation energy of the dye, ϕ_{cb} the conduction band edge of the semiconductor and F the faraday constant. On the other hand the oxidation potential of the dye-oxidized state $\phi^0(S^+/S)$ has to be more positive than the oxidation potential of the regeneration system.

$$\phi^0(S^+/S) < \phi(D^+/D) \quad (5)$$

Recently it has been shown that the excess of vibrational energy of the dye acquired during the excitation could be used in the electron injection process.[1-3] Therefore, dyes with lower (S^+/S^*) energy than the conduction band, but excited with photons that bring them in a vibronic level that lies above the conduction band edge are also able to inject in the semiconductor.

- To ascertain efficient electron injection and high operational stability the dye needs to be firmly anchored to the TiO_2 surface. Groups such as carboxylate, phosphonate or sulfonate are commonly used for the surface attachment onto oxide semiconductors. Therefore standard dyes bear attachment groups, which enable chemisorption of the dye on the TiO_2 surface. With decreasing distance of the dye to the surface the electron injection rate increases. The rate can be further accelerated when the π-system of the dye in the excited state can be delocalized into the semiconductor. So far dye adsorption from solution is the most convenient method for the dye uptake.

- The dye must possess long-term stability for reproducible device characterisation as well as for future commercial applications, which requires cell lifetimes of 20 years with 10^8 redox turnovers under illumination. Despite intensive research in the field of sensitizer engineering so far no dye has been reported that may replace the ruthenium complex *cis*-$[Ru^{II}(dcpby)_2(NCS)_2]$ as standard dye for the application in dye-sensitized solar cells. This is mainly due to the enhanced stability of the ruthenium complex compared to other sensitizers.

A vast variety of different sensitizers have been examined so far. In the context of artificial photosynthesis natural dyes such as chlorophyll[4] and different porphyrins[5] were used. Organic dyes with high extinction coefficient such as cyanines and

Xanthenes are known from their application in photographic films for the sensitization of AgCl crystals and were also used as sensitizers in photo electrochemical devices to create photocurrent. The photochemical properties of merocyanine dyes and their application in the dye-sensitized solar cell has been intensively studied by Nüesch.[6,7] Inorganic particles of nanometer scale (quantum dots) have been recently used in photo electrochemical cell as well as in SSD.[8] This type of sensitizer offers the advantage of choosing the region of adsorption by tuning the size of the nano particle.

The highest efficiencies for dye-sensitized solar cells were reported for devices based on $(Bu_4N)_2[Ru(dcbpyH)_2(NCS)_2]$.[9] This dye was also mainly used in this work and was obtained by reaction of the fully protonated form, the N3 dye, with 0.5 dye mole equivalents of t-butylammonium hydroxide. The N3 is attached to the TiO_2 via two of the four carboxyl groups situated trans to the NCS ligand.[10] The dye adsorption onto TiO_2 follows the Langmuir theory with a binding constant of $K=5\cdot10^4 M^{-1}$.[11] The area occupied by one molecule at the anatase surface at full monolayer coverage is 1.65 nm^2.

iii) <u>The hole transport material.</u>
The hole conductor regenerates the oxidized dye after electron injection into the semiconductor, and transports the positive charge to the counter electrode. To function efficiently the following requirements have to be fulfilled.

- The work function of the hole conductor must be smaller than that of the sensitizer:

$$\phi(D^+/D) < \phi^0(S^+/S) \quad (6)$$

Since the maximum photovoltage obtainable is related to the position of the hole conductor's redox potential, $\phi(D^+/D)$ should be as positive as possible. On the other hand the difference of the two potentials should be large enough to provide sufficient driving force for the dye reduction and therefore an optimal regeneration rate. It is obvious that the redox-couple must be reversible at the counter electrode, while being inert to the TiO_2. Moreover the redox mediator, in particular its oxidized form, must not quench the excited state of the dye, so that the reaction has to be significantly slower than the electron transfer of the dye to the TiO_2.

- The hole conductor should not have any significant light absorption in the visible range, to avoid internal filter effects. This property is particularly important when illuminating the device through the counter electrode, or when using reflecting counter electrodes.

- The hole conductor must be processible, without destruction of the dye adsorbed on the TiO_2. Typical deposition techniques for organic semiconductors are thermal evaporation, electrochemical deposition, and different coating techniques, such as spin coating, dip coating or tape casting. For the formation of stable amorphous films, materials with relatively high glass melting temperatures are needed. Regarding the filling of the TiO_2 pores with the organic semiconductor, low molecular weight molecules are preferred to polymers.

- The hole transport material (HTM) should be able to transport a current of an at least 20 mA/cm^2 without diffusion limitation or significant ohmic losses. This is a very stringent requirement to fulfill for most of the organic semiconductor systems, which typically show a rather low conductivity in the undoped state. The limiting current depends on the thickness dx of the charge-transporting medium, the number of charge carriers dn and the mobility μ, which is a material constant:

$$J_n = \mu \cdot k \cdot T \cdot \frac{dn}{dx} \quad (7)$$

  To avoid resistive losses, the conductivity of the organic film can be enhanced by increasing the number of charge carriers through oxidative doping and by adjusting the layer thickness of the hole conductor.

The holed conductor Spiro-MeOTAD, (2,2', 7,7'-tetrakis(N, N-di-*p*-methoxyphenyl-amine)-9,9'-spirobifluorene) was designed based on the standard hole transport material N, N'-diphenyl-N, N'-bis (3-methylphenyl)-1,1'-biphenyl-4, 4'diamine (TPD). The structural modifications allowed for the tuning of the molecular properties for application in organic devices: the thermal stability of the glassy state could be drastically improved by connecting two TPD units via a spiro centre.[12-14] Due to the increased steric demand of the spiro molecule, solution and crystallization properties are changed without significant change of the electronic properties of the base molecule. Compared to TPD, spiro-MeOTAD has a 60°C higher glass transition temperature, which enables the formation of stable amorphous films. While films of TPD are more or less crystallized after two months, pure spiro-MeOTAD film will stay in the amorphous state for years. However, the introduction of the spiro center also increases the melting point to 246 °C, which makes it impossible to produce layers of spiro-MeOTAD by thermal evaporation in UHV. The standard deposition technique is therefore spin coating of a solution of spiro-MeOTAD in chlorobenzene.

The substitution of TPD with two metonym substituents leads to a seven times higher hole mobility of the material.[15] TPD molecules containing methoxy substituents show an improved stability of the corresponding radical cation, which has been assigned to increased electronic overlap of the molecular orbitals caused by the electron withdrawing methoxy groups. Spiro-MeOTAD contains 8 methoxy substituents and shows a 0.1 V higher oxidation potential, compared to the unsubstituted structure.

The reduced form of the hole conductor is pale yellow and absorbs in the UV (λ_{max}=372 nm). Its four oxidation states can be obtained via chemical oxidation with [N (p-C_6H_4Br)][$SbCl_6$].[16] The spectrum of spiro-MeOTAD$^+$ shows an intense band at 511 nm and a shoulder at 700 nm. The spiro center connects two identical molecule units in a perpendicular arrangement and acts as an electronic barrier. Therefore the spectrum of the spiro-MeOTAD^{2+} is similar to the mono cation but with a doubled extinction coefficient. According to Weissörtel[14] the diradical cation of spiro-MeOTAD shows absorption maxima in $CHCl_3$ at 511 nm (ε=40100) and 1400 nm (ε=32200), while Spiro-MeOTAD^{4+} exhibits an absorption maxima at 865 nm (ε=118000).

The mobility of the spin-coated spiro-MeOTAD has been studied by Poplavsky[17] by means of time-of-flight (TOF) measurements, dark-injection space-charge-limited current transients and steady-state current-voltage characteristics. The voltage dependent room temperature

mobilities for film thickness ranging 4000 nm to 135 nm were determined to be in the around of 10^{-4} cm^2/Vs. Contrary to earlier results published by Bach[18] employing smaller molecules of the same structural type as spiro-MEOTAD, the charge transport has been found to be a non-dispersive process. Analysis of the temperature-field behavior of the time-of-flight mobility based on the Gaussian Disorder Model developed by Bässler et al.[19] revealed higher energetic disorder for the methoxy-substituted compound (spiro-MeOTAD) than for the non-substituted analogue. The comparison of similar molecules with and without spiro center revealed that the spiro-concept leads to high morphologic stability, without deteriorating its electronic properties.[18]

The conductivity of a pure, 1 μm thick film spiro-MeOTAD film is in the range of $M\Omega/cm^2$. The relative low charge mobility has been compensated for by doping of the hole conductor film using tris (p-bromopheny) ammoniumyl hexachloroantimonate [N $(p\text{-}C_6H_4Br)_3][SbCl_6]$.[20] This oxidative doping of spiro-MeOTAD via a one-electron transfer increases the dark conductivity by many orders of magnitude.

iv) The counter electrode.

The counter electrode has ideally a high conductivity and exhibits an ohmic contact to the hole conductor, which requires work function matching of hole conductor and counter electrode. A large built-in potential between the electrode materials corresponding to a large difference in work function of the two materials decreases the Uoc considerably. Noble metals with high work function, such as gold and platinum as well as carbon and conducting polythiophene polymers were found to form an ohmic contact with spiro-MeOTAD.[16] Gold and platinum are typically applied by thermal evaporation in UHV or by sputtering in the case of platinum which is a very controllable technique and therefore reproducible. However it is vigorous for the organic surface and there is some concern about chemical modification of the organic surface.[16,21] Metal counter electrodes have the advantage of reflecting the light[1] transmitted by the photo electrode which cause a second traversal of the dye-sensitized film, thus enhancing light absorption for a given amount of dye. Inert metals which do not chemically react with the organic semiconductor are, however, known for their diffusion on the surface and into the interior of the organic even at room temperature.[22-24] This mechanism is highly dependent on the evaporation parameters such as evaporation rate and evaporation temperature.[25] Carbon and in particularly organic polymers have lower conductivities than the metals. Both carbon and conducting polymers are typically applied in form of pastes by screen-printing or tape coating. The definition of small electrode areas is difficult with this wet deposition techniques and the resulting devices are less reproducible. Carbon can also applied in form of pressed graphite.[26] This technique is very fast and can be easily reversed. It is however complicated to apply in case of subsequent sealing. Gold electrodes were used in present work for the sake of simplicity and reproducibility. Metal films serve moreover as an oxygen barrier and can thus protect the organic material underneath. Better stability of gold electrodes compared to graphite electrodes were also observed in other SSD.[26]

A.1.2 Electron Transfer Dynamics

[1] Gold is an excellent reflector for the IR(800nm-30μm: 98%). In the visible region an opaque gold film is still reflecting about 40% of the incident light. Evaporated platinum films have a reflectance of 60-75 % between 400-800 nm.

Dye-sensitized solar cells are working on the basis of differential kinetics. The presence of a local electrostatic field is not required to achieve good charge carrier collection efficiencies. This distinguishes nanocrystalline devices from conventional photovoltaic cells where successful operation is contingent upon the presence of a potential gradient within the p-n junction. Redox processes involved in light energy conversion are shown in Fig. 17.

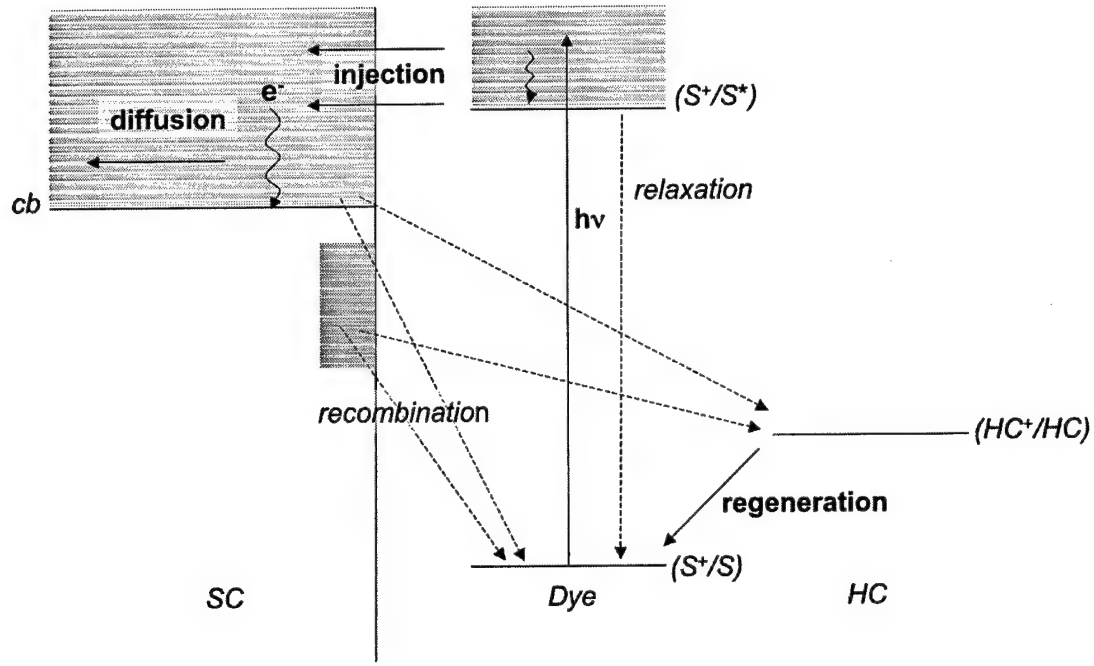

$S\|SC + h\nu$	$\rightarrow S^*\|SC$	excitation
$S^*\|SC$	$\rightarrow S^+\|e^-_{cb}(SC)$	injection
$S^*\|SC$	$\rightarrow S\|SC + h\nu' + \Delta$	relaxation
$S^+\|SC + HC$	$\rightarrow S\|SC + HC^+$	regeneration
$S^+\|e^-_{cb}(SC)$	$\rightarrow S\|SC$	recombination
$S^+\|e^-_{cb}(SC)$	$\rightarrow S^+\|e^-_{cb}(TCO)$	percolation

Figure 17. Electron transfer processes at the dye-sensitized heterojunction

Recent studies of the *electron injection* dynamics from the electronically excited state of Ru (II) polypyridyl complexes into the conduction band of the TiO_2 demonstrated that the electron injection is occurring in the ultra fast time regime (fs to ps) and that the dye cation radical is formed with a yield of nearly 100 %.[27-30] Assuming, that the injection kinetics does not significantly change upon replacement of the electrolyte mediator by the solid-state charge transport material,[31] the injection of electrons by the sensitizer in the solid-state solar cell is expected to show similar characteristics as have been determined for the electrolyte cell. The rate of electron injection has been shown to depend on a variety of parameters, such as the length of the spacer between electron donor and acceptor,[32] the density of acceptor states,[33] and the electronic coupling between the dye and the semiconductor.[34] Moser et al. have shown that the exciting wavelength has an influence on the quantum yield of the electron injection, implying that electron injection can take place from hot vibrational states.[2,3,35] The competition between relaxation of the dye excited state and the injection reaction is contra dictionary to Kasha's rule.[36]

The electron movement in the nanocrystalline TiO_2 to the back contact (*percolation*) is significantly slower than TiO_2 single crystals. This has been demonstrated by photocurrent transient measurements after UV illumination of TiO_2 particles, which showed decay times of milliseconds to seconds.[37]
Recapture of conduction band electrons by the oxidized ruthenium complex is also slow, occurring typically in the micro to millisecond time domain. This slow *recombination* rate has been assigned to the weak overlap of the d-Orbital localized on the Ru metal and the TiO_2 conduction band, which are involved in this recombination process. Other recombination pathways are more important for the function of the cell and will be discussed in more detail in chapter 5.

The dynamics of the *interception* of the oxidized dye by the hole conductor have been found to proceed with a broad range of time constants from 3 ps$<\tau<$1 ns.[38] Multiple phases of injection process were assigned to the heterogeneous nature of the heterojunction, incomplete pore filling and the thereby resulting lateral hole migration between neighbouring dye molecules[39,40] not in contact with the regeneration material. The hole injection quantum yield has been calculated to be 50 % after 900 ps. At longer times, around 10 ns, the efficiency of hole transfer approaches unity.

References to Chapter A.1

[1] F. Lenzmann, J. Krüger, S. Burnside, et al. *J Phys Chem B* **2001**, *105*, 6347-6352.
[2] J.-E. Moser and M. Grätzel. *Chimia* **1998**, *52*, 160-162.
[3] J.-E. Moser, M. Wolf, F. Lenzmann, et al. *Zeitschrift für Physicalische Chemie* **1999**, *212*, 85-92.
[4] A. Kay, R. anHumphry-Baker and M. Gratzel. *J Phys Chem* **1994**, *98*, 952-959.
[5] A. Kay and M. Grätzel. *J Phys Chem* **1993**, *97*, 6272.
[6] F. Nüesch, J. E. Moser, V. Shklover, et al. *J Am Chem Soc* **1996**, *118*, 5420-5431.
[7] F. Nüesch and M. Grätzel. *Chem Phys* **1995**, *193*, 1-17.
[8] R. Plass, S. Pelet, J. Krueger, et al. *J Phys Chem B* **2002**.
[9] M. K. Nazeeruddin, R. Humphry-Baker, P. Liska, et al. *sibmitted for publication* **2003**.
[10] K. S. Finnie, J. R. Bartlett and J. L. Woolfrey. *Langmuir* **1998**, *14*, 2744-2749.
[11] A. Hagfeldt and M. Graetzel. *Acc Chem Res* **2000**, *33*, 269-277.
[12] J. Salbeck, F. Weissörtel and J. Bauer. *Macromol Symp* **1997**, *125*, 121-132.
[13] J. Salbeck, N. Yu, J. Bauer, et al. *Synthetic Metals* **1997**, *91*, 209-215.
[14] F. Weissörtel. Ph. D. Thesis, 1996.
[15] J. S. Facci, M. Abkowitz, W. Limburg, et al. *J Phys Chem* **1991**, *95*, 7908-7914.
[16] U. Bach. Ph.D. Thesis, EPFL, 2000.
[17] D. Poplavskyy and J. Nelson. *J Appl Phys* **2003**, *93*, 341-346.
[18] U. Bach, K. Decloedt and M. Grätzel. *Adv Mat* **2000**, *12*, 1060-1063.
[19] H. Bässler. *Phys Stat Sol B* **1993**, *175*, 15.
[20] M. Abkowitz and D. M. Pai. *Phil Mag B* **1986**, *53*, 193.
[21] A. Ioannidis, J. S. Facci and M. Abkowitz. *J Appl Phys* **1998**, *84*, 1439-1444.
[22] M. Probst and R. Haight. *Appl Phys Lett* **1997**, *70*, 1420-1422.
[23] R. Willecke and F. Faupel. *JOURNAL OF POLYMER SCIENCE PART B-POLYMER PHYSICS* **1997**, *35*, 1043-1048.
[24] R. Willecke and F. Faupel. *Macromolecules* **1997**, *30*, 567-573.

[25] A. C. Dürr, F. Schreiber, M. Kelsch, et al. *Adv Mater* **2002**, *14*, 961-963.
[26] B. O'Regan, F. Lenzmann, R. Muis, et al. *Chem Mater* **2002**, *14*, 5023-5029.
[27] Y. Tachibana, J. E. Moser, M. Graetzel, et al. *J Phys Chem* **1996**, *100*, 20056-20062.
[28] R. Eichberger and F. Willig. *Chem Phys* **1990**, *141*, 159.
[29] J. Kallioinen, V. Lehtovuori, P. Myllyperkiö, et al. *Chem Phys Lett* **2001**, *340*, 217-221.
[30] C. Bauer, G. Boschloo, E. Mukhtar, et al. *J Phys Chem B* **2001**, *105*, 5585-5588.
[31] J. R. Durrant, Y. Tachibana, I. Mercer, et al. *Z Phys Chemie-Int J Res Phys Chem Chem Phys* **1999**, *212*, 93-98.
[32] J. B. Asbury, E. Hao, Y. Wang, et al. *j Phys Chem B* **2000**, *104*, 11957-11964.
[33] B. Langdon, V. MacKenzie, D. Asunskis, et al. *J Phys Chem B* **1999**, *103*.
[34] K. Kalyanasundaram and M. Gra¨tzel. *Coord Chem Rev* **1998**, *77*, 347–414.
[35] J. Moser, D. Noukakis, U. Bach, et al. **1998**.
[36] M. Kasha. *complex molecules* **1950**, 14-19.
[37] A. Hagfeldt and M. Grätzel. *Chem Rev* **1995**, *95*, 49-68.
[38] U. Bach, Y. Tachibana, J.-E. Moser, et al. *J Am Chem Soc* **1999**, *121*, 7445-7446.
[39] P. Bonhôte, E. Gogniat, S. Tingry, et al. *J Phys Chem B* **1998**, *102*, 1498-1507.
[40] T. A. Heimer, S. T. D'Arcangelis, F. Farzad, et al. *J Inorg Chem* **1996**, 5319-5324.

A.2 Device Preparation Procedures

This chapter discusses the materials and technique used for the preparation of solid-state dye-sensitized solar cells. Although, the hole conductor based device uses a monolithic design, other embodiments discussed in subsequent chapters employ similar procedures for several key steps, such as the preparation of the nanocrystalline semiconductor oxide films. The TiO_2 photocathode, the hole conductor film and the counter electrode are fabricated successively in a multi-step processes, employing wet and dry processing techniques.

A.2.1 Materials

Unless otherwise stated all chemicals were purchased from Aldrich (Switzerland) and at least reagent grade, respectively puriss. p.a. for solvents. Chlorobenzene and Acetonitrile, used for the preparation of the spin-coating solution contained less than 0.01% and 0.1 % H_2O (Karl-Fisher Analysis) respectively and were stored under inert atmosphere until use. Stock solutions of additives for the spin-coating solution, such as $Li[(CF_3SO_2)_2N]$ in acetonitrile, were prepared and stored in dry atmosphere.

Tert.butylpyridine (*t*BP) were purchased from Fluka, purified by distillation (Fischer column) and stored under dry atmosphere until use. The standard dyes N3 ([Ru (2,2'-bipyridyle-4, 4'-dicarboxylate) $_4(NCS)_2]H_4$) and N749 (black dye) were supplied by Solaronix (Aubonne, Switzerland) and were dissolved in a 1:1 mixture of acetonitrile:tert.-butanol or in ethanol The deprotonated form of the dye (N719, [Ru (2,2'-bipyridyle-4,4'-dicarboxylate)$_2$(NCS)$_2]H_2(Bu_4N)_2$) was obtained by adding two dye equivalents of a solution of 40% tert.butylammonium hydroxide in H_2O to the dye solution. All other dye solutions used were supplied by Dr. Mhd. Nazeeruddin and Dr. S. Zakeeruddin (LCMB, EPFL) and were used as received. Details on in house dye synthesis are given separately below.

Di-isopropoxytitanbis(acetylacetonate) (TAA), used as precursor for the spray-pyrolytic deposition of compact TiO_2 layers was purchased from Fluka. The TAA was stored under inert atmosphere and was diluted with ethanol to a final concentration of 0.2 M prior to use. Under normal atmospheric conditions the color of the precursor solutions changed from yellow to orange. Although current-voltage characteristics of layers prepared from aged solutions and from fresh solutions did not show any significant difference, precursor solutions were always prepared freshly before use.

The hole conductor 2,2',7,7'-tetrakis(N,N-di-p-methoxyphenyl-amine)-9,9'-spirobifluorene (spiro-OMeTAD) was supplied by Covion Organic Semiconductor GmbH, Frankfurt/Germany (purity>99.8 % HPLC analysis) and was used as received.

Screen-printable TiO_2 colloids pasts for the preparation of the nanocrystalline TiO_2 layers were prepared by P. Compte following the procedure described by Barbé et al.:[1]

1. *precipitation* (hydrolysis of Ti-alkoxides using 0.1 M HNO3)
2. *peptisation* (heating at 80 °C for 8 h) followed by filtering
3. *hydrothermal growth/autoclaving* (12)
4. *sonification* (ultrasonic bath, 400 W, 15x2 s)

5. *concentration* (45°C,30 mbar)
6. *binder addition* (carbowax/Polyethyleneglycol, M_w=20 000

The porosity, particle size and specific area for the different TiO_2 colloids used in the present work are summarized in Table 2. Compared to the TiO_2 films in solid electrolyte cells TiO_2 films for hole conductor cells have a higher porosity to facilitate the filling of the porous network with the spiro-MeOTAD. Upon dye uptake the effective porosity of the TiO_2 film is reduced by about 25 %. The decrease in porosity caused by the dye deposition is .[2]

Colloidname	Porosity [%]	Particle Size [nm]	Specific Surface [m^2/g]
JDD1x-S7	69.3	15	104
RCO1x-S1	65.3	15	105
PC100x-S2	66	19	83
PC117	65.1	19.5	83
PC131	65	15	104

Table 2. Physical parameters for different nanocrystalline films prepared and characterised by P. Comte. The pore size and specific surface area have been derived from N_2 adsorption experiments (BET). The porosity was calculated from the ratio of the cumulative pore volume V_p, to the total volume V_{tot}, which is given by $V_{tot}=V_P+mx\rho(TiO_2)^{-1}$, where m is the mass and ρ □□□ densitiy of anatase $\rho(TiO_2)$=3.85g/cm

A.2.2 General Device Assembly

Figure 18 shows the two different types of device employed for the studies. The first contains four small diodes, each having an active area of 0.16 cm^2. The second is a larger device with an active area of about 1cm^2. The device carrying four active diodes has been used for device parameter screening purposes. The large device has been used for physical characterisations, such as the impedance studies, as it allows the encapsulation of the photovoltaic active area. Compared to the small diode device the large device has been improved concerning resistive losses and definition of the active area. This becomes evident when comparing the photovoltaic characterics of the two device types measured with and without mask. The difference in performance for the small diode device is around 10 %, whereas it is negligible for the large cell. Furthermore it is gratifying that there was no loss in performance for the large cell, despite of the scale up in size.

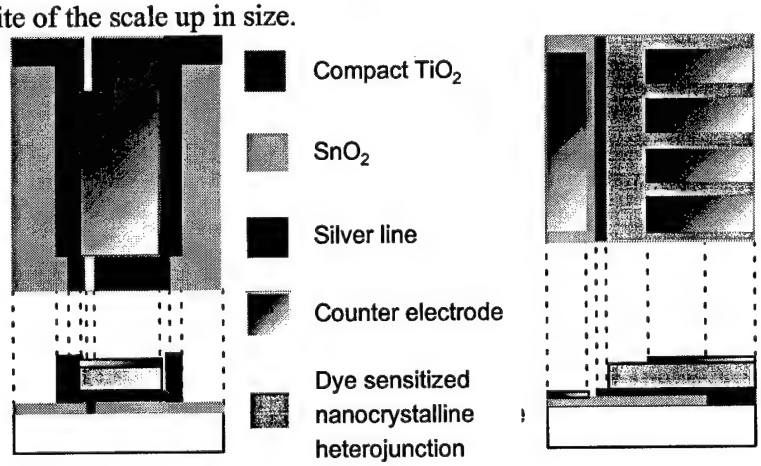

Figure 18: Schematic presentation of the large active area and small active area device.

i) TCO substrates

Unless otherwise stated, TCO substrates were structured by chemical etching using Zn granulate (20 mg/cm^2) in combination with either 4N HCl or 2 M citric acid (1 ml/ cm^2). Scotch© tape was used to mask a TCO area for the back contact in the final device. The use of HCl has the advantage of a fast removal of the SnO_2 layer. After two treatments during 3 minutes the SnO_2 is completely removed. However for some types of TCO substrates and for fine structuring HCl is too vigorous, leading to very irregular etching borders. In this case citric acid has been used, which allows a more exact structuring but requires a longer reaction time of up to 45 minutes. The structured TCO layers were purified by subsequent sonification in various solvents (1 * acetone, 2 * ethanol, 1 * Hellmanex® II (2 % in H_2O), 3 * H_2O, 2 * ethanol) which a duration of 10 min each time. Cleaned substrates were stored in pure ethanol. Prior to deposition of TiO_2 the layers were additionally cleaned by a UV/Ozone treatment (UVO-Cleaner®, Model No. 256-220, Jelight company Inc.) for 15 minutes.

ii) Choice of different TCO's

An effective TCO should have high electrical conductivity combined with low absorption of visible light. However the decrease of resistivity is correlated with a decreased transmission for a given material. Correspondingly the two parameters have to be optimized for the application of interest. In particularly for device used without compact TiO_2 layer the interfacial and material-compatibility properties of the TCO are also important, determining the attachment of the deposited material to the TCO.

The TCO should pass the demanding processing conditions for the device preparation without change of its physical properties. The resistance of TCO's will increase, if heated to high temperatures and for long time. However, the TCO typically remains stable up to temperatures slightly above the optimized deposition temperature. Fluorine doped SnO_2 films are generally very stable, so that the softening of the glass substrate is more limiting than any thermal decomposition of the conducting layer. In contrast indium tin oxide (ITO) films, used in particularly for the preparation of OLED's, show significant losses of conductivity upon heating over 200°C.

A selection of commercially available TCO's has been compared concerning their optical and electronic properties as well as their thermal stability. As a quantitative measure (figure of merit) for the performance of the TCO the ratio of the resistance to the transmission of 550 nm radiation has been used. A small value indicates better performance of the TCO. Table 3 demonstrates that all glass types are thermally stable except for the Asahi glass. The Solaronix glass and the TEC8 glass showed the best performance. However, at the time of these experiments the Solaronix glass was not available on larger scales and the chemical structuring of the TEC8 glass is difficult. For reasons of availability Asahi glass has been used for device parameter screening purposes, avoiding sintering temperature over 450°C. For high performance devices TEC 8 and Solaronix glass were employed.

Glass type	T_{550} [%]	R_0 [Ω/□]	R_1 [Ω/□]	R_2 [Ω/□]	R_0/T [Ω/□]
Solaronix (9 Ω/□, 1mm)	85	8.4	8.6	8.8	0.10
Asahi, (10 Ω/□, 1mm)	82	13.5	12.5	60.2	0.16
NSG (12 Ω/□, 1mm)	82	12	12.9	14	0.15
Tec8 (8 Ω/□, 3mm)	80	7.7	7.7	7.9	0.10
Tec15 (15 Ω/□, 3mm)	82	13	14.6	14.3	0.16

Table 3: Comparison of TCO substrates commonly used for the preparation of SSD and DSSC, with T=Transmission at 550 nm, R_0 = initial resistance, R_1 = resistance after first sintering, R_2= resistance after second sintering, and R_0/T = figure of merit. In parenthesis behind the glass type the nominal resistance of the glass is given as well as the thickness of the glass. Resistance measurements have been performed using the four-point technique.[3, 4] The sintering involved heating at 500 °C for 10minutes (heating rate 10 min). Solaronix glass was provided by Dr. Meyer (Solaronix SA) and Asahi glass by Dr. Uhlendorf (INAP).

iii) Deposition of blocking TiO_2 layer

Compact films of TiO_2 were deposited by aerosol pyrolysis of the precursor TAA®, according to the procedure described by Kay[5] and Kavan.[6] The samples were heated to 450 °C (NiCr/Ni thermopile) on a temperature-controlled hotplate and the precursor solution was sprayed from a distance of 20 cm using a chromatographic atomiser (Glas Keller, K1596). For layers of about 100 nm thickness 30 spray processes of roughly 75 µl precursor solution with an interval of 10 sec were performed, which corresponds to an overall consumption of 0.09 ml/cm^2. The interval between each spray process allows the complete evaporation of precursor solvent and to restore the original substrate temperature. Thin 1 mm float glass, structured by a sandblast, was used as mask to cover lines of SnO_2 for later contact formation. The substrates were thermally equilibrated on the hotplate for 5 minutes prior to the spray-coating process and left for at least 10 minutes after the deposition to complete the transformation of the precursor to TiO_2 and to evaporate residual organics.

Layer thickness measured by electron microscopy was approximately constant for 20 to 30 spray applications. Nevertheless, layers prepared by 30 repetitions of the spraying process were more homogeneous and dense, and give more reproducible current-voltage characteristics than the thinner layers. The compact nature of the TiO_2 layer manifests itself by a perfect blocking of anodic reactions on the bare TiO_2 electrode. Cathodic reactions take place at higher overvoltages as expected from the n-type of the layer. The resulting TiO_2 layer possesses mainly anatase character[6] and is presumably n-doped.

iv) Nanocrystalline TiO_2 layers

20 mm broad stripes of TiO_2 paste were deposited by manual screen-printing, respectively squares of 2*0.8 cm^2 for the large area device. After the coating step the films were allowed to settle for about 30 minutes at room temperature under normal atmospheric conditions in a dust free container. The layers were then fired to remove organic additives and to sinter particle to a mechanically adhering and electrically conducting film. A special sintering program has been followed to obtain reproducible grain growth and phase transformation during the sintering. The temperature program consists of heat ramps and isotherms, that are chosen to separate the combustion of the additives and the sintering in time. This is done in order to avoid contamination due to carbon inclusions, a problem, which may occur if organics are trapped in pores, which close during calcination before they can burn off. The upper sintering temperature, which is typically 500-600 °C, is determined by the physical properties of the substrate. The firing atmosphere is affecting the doping of the TiO_2. Firing an oxide in a reducing atmosphere such as hydrogen for example may create oxygen vacancies, which leads to n-type doping. Previous work by Kay[5] has shown that best results for the TiO_2 colloids are obtained for sintering in dry air or under a constant flux of oxygen.

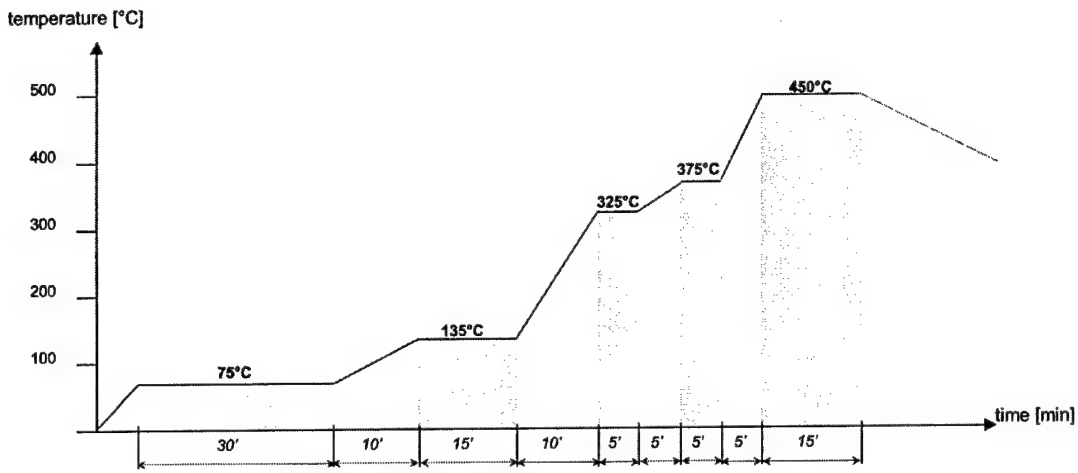

Figure 19: Temperature program for sintering of screen-printed films.

TiO_2 films of different thicknesses were realized using appropriate screens in combination with pastes of different TiO_2 colloid contents and different amounts of organic additives. As the filling of the pores is not only dependent on the properties of the pores in the nanocrystalline network but also on a variety of other parameters, such as post treatments of the TiO_2, the dye coverage or the properties of the spin-coating solution, a pre-estimation of the pore filling is difficult. The layer thickness of the TiO_2 has been therefore optimized for a given set of colloid, dye and spin-coating solution on the base of the indirect measure of the photovoltaic performance. If not otherwise specified no scattering particles were added to the TiO_2 pastes and the films obtained where highly transparent.

In general TiO_2 films were subjected to a $TiCl_4$ treatment. This treatment has been shown to increase the injection of electrons into the TiO_2 and thus the current that is delivered by the solar cell. The positive effect has been assigned to the increased surface area for dye adsorption and to the formation of a native surface TiO_2 layer of higher purity. Furthermore Ti complexes in $TiCl_4$ solution are believed to condense at interparticle necks, thereby increasing the interparticle connection and the electron percolation. However the treatment

causes a decrease of the average pore size and the porosity. Therefore the $TiCl_4$ concentration and time of treatment has to been optimized with respect of the demand of pore size.

50 µl/cm^2 of a 0.02 M $TiCl_4$ solution were applied to the nanocrystalline film for 12 hours at room temperature in a dust free environment. Contact areas were protected with adhesive tape. Afterwards the samples were washed with a large amount of distilled water and sintered for a second time for 15 minutes at 450 °C (ramp: 10 minutes).

v) Sensitizer deposition

TiO_2 films were stored in a desiccator over silica gel until the final assembly of the solar cell. Before the dye uptake TiO_2 layers were then again heated to 450 °C for 15 minutes. The firing leads to a partially dehydroxylated, highly activated surface for dye adsorption. Typically the nanocrystalline TiO_2 films were soaked in the corresponding dye solution for 24 hours in the dark prior to the spin-coating process.

vi) Effect of dye structure

Beside the requirements for an efficient sensitizer discussed in chapter 2, the dye structure has also an influence on the quality of the junction between the TiO_2 and the hole conductor. For related organic devices, such as LEDs, the consequences of the introduction of organic molecules on the band energy position, morphology, and stability (hydrophobicity) of organic/inorganic contacts have been studied in detail. Goncalves-Conto et al.[7] have demonstrated that the improved wetting of ITO substrates by organic semiconductors can enable adsorption of self-assembled monolayers (SAM) of appropriate molecules. Similarly the spin-coating of the hole conductor leads to films of better quality when the deposition has been established on the dye-sensitized TiO_2 instead of the pure TiO_2. A dye with organic chains pointing towards the pores might therefore facilitate the filling the nanoporous network by the hole conductor.

On the other hand Bauer[2] has shown that the introduction of a spacer between attachment group and redox center of the dye is slowing down the injection rate. This has no significant impact on the quantum yield of electron injection, which remains high as long as it is faster than the competing deactivation reactions of the excited sensitizer. However, voluminous organic chains pointing towards the hole conductor might have a similar influence on the interception kinetics, and what is even more important, might shield the TiO_2 surface and therefore affect also recombination kinetics.

The effect was studied using a series of heteroleptic ruthenium dyes, where one of the bipy ligands of the standard N3 sensitizer was substituted by hydrophobic groups. The structures of the complexes are presented in Figure 20 along with the abbreviations used.

---

[2] unpublished results

R	Abbreviation
$-CO_2H$	N3
$-CH_3$	N3_C_1
$-CH_3$, $-C_9H_{10}$	N3_C_1C_9
$-C_4H_9$	N3_C_4
$-C_9H_{10}$	N3_C_9
$-C_{12}H_{13}$	N3_C_{12}

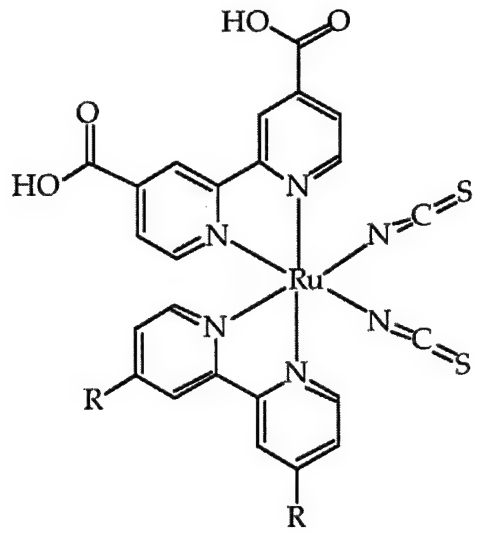

Figure 20: Hydrophobic dye structures with aliphatic chains of different length. All dyes were synthesized by Md. K. Nazeeruddin and S. M. Zakeeruddin.

These hydrophobic dyes show an absorption spectrum similar to the N3 dye in ethanol solution, but possess a 18 % lower molecular extinction coefficient[3]. Upon adsorption to the TiO_2 surface the dye spectra are blue shifted, with a maximum absorption around 505 nm, while the corresponding absorption maximum of the N3 and the N719 dye is about 515 nm. The kinetics of the adsorption have been found to alter slightly for the different dyes.[8] However a typical time for dye uptake was 24 h, which is long enough to reach the adsorption equilibrium.

Figure 21 summarizes the photovoltaic parameters of SSD sensitized with the different hydrophobic sensitizers. A clear trend is observed, showing improved performance for increased chain length of the sensitizer. For comparison the results for the standard N3 sensitizer are also shown. Note that for N3_C4 as the organic side chain is branched rather than linear.

[3] personnal communication Md. K. Nazeeruddin

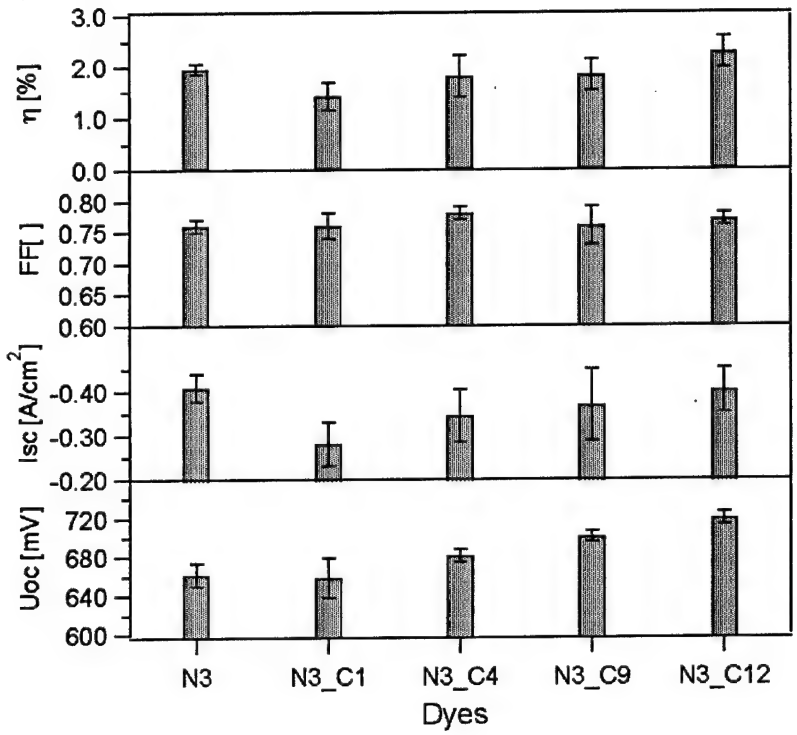

Figure 21: Comparison of the photovoltaic performance of different hydrophobic heteroleptic ruthenium sensitizers at 10 % Sun. The TiO_2 film thickness of the SSD was 2 μm and the hole conductor composition was 0.2 M in spiro-MeOTAD, 0.13 mM in $Li(CF_3SO_2)_2N$, 0.18 M in tBP and 0.76 mM in $N(p\text{-}C_6H_4Br)_3SbCl_6$. The composition of the hole conductor film will be discussed more in detail below. Comparison at 10% Sun has been chosen to avoid masking of the sensitizer performance by charge transpor limitations of the photocurrent in the hole conductor.

As the photochemical and electrochemical properties of the members of the hydrophobic dye series are very similar, the hydrophobic substituent is expected to play an important role in the formation of the heterojunction,. In a similar study with solid electrolyte based solar dye sensitized solar cells,[9] the improved performance of these devices was correlated with lower interfacial charge recombination as a result of a lateral interaction of the long chains of the sensitizer. The influence of the hydrophobic dyes on the recombination dynamics in the SSD has been studied employing nanosecond laser experiments. The differences in the recombination kinetics were rather small and did not exceed an order of magnitude.[8] However, the long chains are expected to shield the inorganic oxide surface, forming an organic environment which might be advantage for the filling of the pores with the organic holeconductor and therefore for the quality of the heterojunction. While the exact mechanism for the improved performance is not clear these experiments demonstrate the importance of the dye structure on the interfacial charge separation process.

vii) Deposition of the spiro-MeOTAD

The samples were removed from the dye solution, washed in the same solvent which was used for the dye uptake and dried under an argon flow. 100 (150) μl of spin-coating solution were applied to the sample of large (small) sample geometry and a thin film was formed by rotating the sample at 1500 rpm for 30 s with an acceleration of 200 rpm. The samples were then dried in argon for 45 min and in vacuum for one hour at (0.1 mbar), before being transferred into a vacuum chamber to apply a thin gold contact layer via thermal evaporation.

viii) Thickness of the hole conductor film

In previous work the concentration of the spin coating solution was maximized to obtain a spacing layer between dye-sensitized heterojunction and the Au counter electrode. The highest solubility of 400 mg/ml was obtained with the solvent chlorobenzene. In other solvents of comparable physical properties, such as toluene or p-xylol, the solubility of spiro-MeOTAD was significantly lower. Spin coating using solvents with low boiling points such as THF yielded films with inhomogeneous thickness distribution.[10] shows the SEM cross-section of the solid-state dye-sensitized heterojunction with a spiro-MeOTAD film on top of the TiO_2.

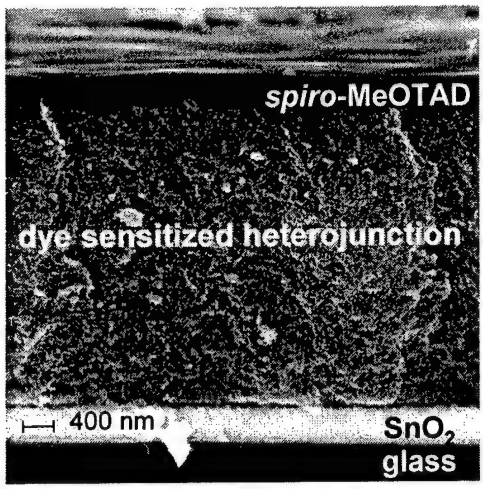

Figure 22: Scanning electron micrograph (SEM) showing the cross section of the solid-state dye-sensitized heterojunction between TiO_2 and spiro-MEOTAD.

It can be observed that the hole conductor forms a barrier layer on top of the TiO_2.Depending on the doping level this layer may considerably increases the resistance of the device. Hence it should be made as thin as possible while still forming a pinhole free barrier layer. The thickness of organic film on top of the TiO_2 is depending on the spin coating parameters, such as spin coating speed and concentration of the spin coating solution

From the SEM cross section in Figure 22, a thickness of about 400 nm can be determined for the hole conductor film on top of the TiO_2, which has been prepared from a 0.2 M spin-coating solution. Figure 23 shows the effect of the hole conductor concentration on the thickness of this layer. Assuming that the relation between concentration of spin coating solution and thickness is similar for the deposition of the hole conductor onto the nanocrystalline TiO_2, a reduction of the concentration of 50 % is expected to result in a film of about 200 nm on top of the nanocrystalline film. Photovoltaic experiments revealed no increased risk of short circuit formation when a spin coating solution containing 0.1M spiro-MeOTAD instead of 0.2 M was employed. However, reducing the thickness of the hole conductor spacer layer between the nanocrystallineTiO_2film and the gold back contact gave made the photocurrent response to light intensity more linear.

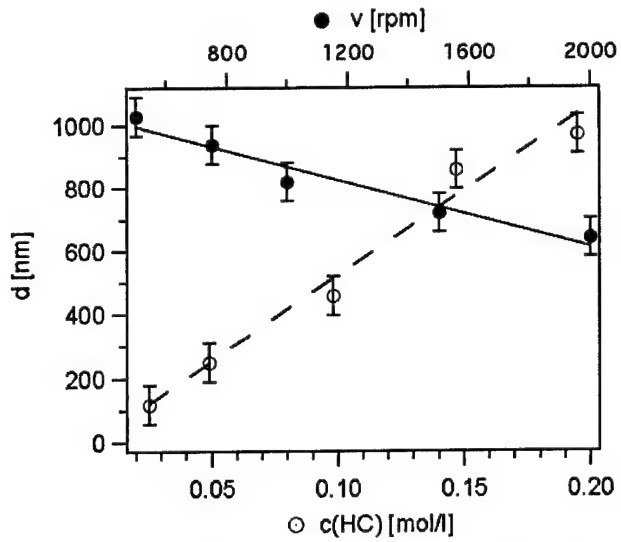

Figure 23. Effect of the the spiro-MeOTAD concentration in the spin coating solution (○) and the spin coating (●) speed on the thickness of the resulting hole conductor film. The thickness of the dried film after spin coating on a bare glass substrate was determined by means of an alpha-step apparatus.

ix) Deposition of counter electrode

The metal contact electrode was deposited by thermal evaporation at a vacuum of $5x10^{-6}$ mbar using a Edwards evaporator (Vacotec Auto 560). Evaporation rates were 0.1 – 0.2 nm/s for the first 0.2 nm and 0.5 – 0.7 nm/s until the desired layer thickness was reached. The thickness of the layer was monitored by a quartz balance setup (FTM7 Film Thickness Monitor). A metal mask was used to define the contact areas on the sample.

Thicker gold layers are of advantage due to their higher reflectance and conductivity. Correspondingly best performance was observed for the thickest counter electrode in a device series with gold layers varying between 10 and 70 nm. The enhanced performance for thicker films was the result of increased short circuit currents. Devices with 20nm gold film showed 22 % higher short circuit currents at 10 % Sun than devices with a 10 nm gold film. A 10 nm gold film is transparent, whereas a 20 nm is opaque. The performance change for variation of the layer thickness over 20 nm is less important because the optical properties do not change as drastically as between 10 and 20 nm. However the deposition of thicker films involves a very long evaporation time and thus longer thermal stress for the devices. Gold films of about 100 nm become mechanically instable and tend to peal off. Devices were therefore typically made with a gold counter electrode of 30 nm thickness.

x) Sealing of device

As for most of the organic devices, sealing is necessary to improve long-term stability devices and protect the active surface against ambienst. The devices have been sealed employing two techniques:

- Encapsulation of the active area with Mylar 25 MC2 (DuPont) by thermal lamination. Mylar 25 is a one-side metallised polyester film, overcoated on both sides with a heat sealable PVDC copolymer.

- Coverage with a 2 mm glass sheet and sealing with a combination of the heat sealable Surlyn film and the epoxide Torr Seal® (Varian Vacuum Products) as shown in figure 24. This encapsulation method is therefore very similar to the one used for the solid electrolyte cell.

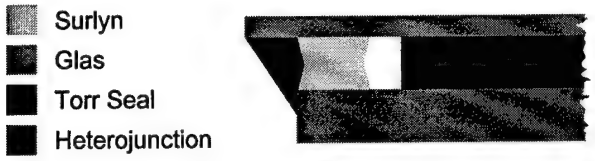

Figure 24. Illustration of sealing with Surlyn and Torr Seal.

Samples sealed with Mylar 25 MC2 showed lifting of the PVDC coating after a few days and loss of laminate bond strength. The second sealing was mechanically stable over a long time and has been further tested immersing the device in a water bath. No water leakage could be observed during a period of two hours. The sealing is therefore efficient in protecting the device against environmental conditions. Moisture included during device preparation, will be encapsulated as well. Hence it is important to exclude moisture and impurities during the cell preparation as much as possible.

A.2.3 Conclusions of the procedures outlined in section A.2

The procedures described above include:

1. the structuring and cleaning of the transparent conducting oxide (TCO) current collector
2. the deposition of the compact underlayer by spray pyrolysis
3. the deposition of the nanocrystalline TiO_2 by screen-printing and the dye uptake
4. the spin-coating of the hole conductor with following drying and
5. the deposition of the counter electrode by thermal evaporation.

The total preparation time is on the average 43 h/device. Hence the preparation of the hole conductor cells is more time consuming than that of the solid electrolyte cell. The increased time demand is caused by the structuring of the current collector, the deposition of the compact underlayer, the spin coating process and the time for the drying of the cell prior to the evaporation of the Au contact. In terms of an industrial application a drastic reduction of the preparation time is expected from automation of several deposition steps, similarly as it has been already established for the electrolyte cell. This includes in particular the automatic screen-printing. Further gain in preparation time as well as in precision is expected from substrate structuring using a laser instead of the chemical etching method. Time intensive steps such as the dye uptake and the drying after the hole conductor deposition can be accelerated by increasing the temperature of the dye solution respectively the drying chamber. The dye uptake from an ethanol solution at 80°C is already an established method, reducing the time for the dye uptake from several hours to 30 min. The drying of the hole conductor film at increased temperatures should be accompanied by studies of the morphology of the hole conducting film to avoid crystallization of this material.

The dye structure was found to play an important role in the formation of the heterojunction. A series of heteroleptic ruthenium complexes, where tow of the four carboxyl groups of the N3 standard dye were exchanged by aliphatic chains of differing length, was studied in the SSD. A correlation of the photovoltaic performances with the chain length of the aliphatic chain was obtained. No significant influence of the chain length on the recombination dynamic was observed. The effect was thus rationalized in terms of an improved wetting of the long-chain dye sensitized TiO_2 by the organic hole conductor.

The excess spiro-MeOTAD material, which does not penetrate into the pores of the TiO_2 forms an isolating organic film between TiO_2 and counter electrode. This film on top of the heterojunction is important to avoid short circuits, but it increases the resistance of the cell. The thickness of this spacer layer was optimized with respect of a functional spacer layer on the one hand, and low film resistance on the other hand. The thickness of the hole conductor was controlled via the spin coating parameters, in particularly the speed of the coating process and the concentration of the spin coating solution.

References for section A.2

[1] C. Barbé, F. Arendse, P. Comte, et al. *J Am Ceram Soc* **1997**, *80*, 31557-71.

[2] N. Papageorgiou, C. Barbe and M. Gratzel. *J Phys Chem B* **1998**, *102*, 4156-4164.

[3] P. Hemenger. *Rev Sci Instrum* **1973**, *44*, 698.

[4] D. Schroder. Semiconductor material and device characterization; Wiley, 1990.

[5] A. Kay. Ph.D., EPFL, 1994.

[6] L. Kavan and M. Grätzel. *Electrochimica Acta* **1995**, *40*, 643.

[7] S. Goncalves-Conto, M. Carrard, L. Si-Ahmed, et al. *Adv Mat* **1999**, *11*, 112-115.

[8] M. Stalder, Travail Diplôme, EPFL, 2002.

[9] S. M. Zakeeruddin, M. K. Nazeeruddi, R. Humphry-Baker, et al. *Langmuir 18* **2002**, *18*, 952-954.

[10] J. Krüger. Diplomarbeit, Universität Heidelberg, 1998.

B. Dye sensitized Solid State Cells, General Procedures and Specific Details on Rigid and Flexible Cells Based on Solid State Electrolytes.

Many of the technical points outlined in the previous chapter apply also to the dye sensitized solar cells based on solid electrolytes. Hence a good part of the experience gained from these studies benefit directly subsequent work on solid-state electrolytes. It became clear during the

first phase of the project that the latter would be a suitable choice to realize light weight flexible devices having conversion efficiencies. In the following we shall focus on procedures and experiments that are specific to the rigid and flexible version of electrolyte based cells. The phenomenal progress realized recently in the fabrication and characterization of nanocrystalline materials has opened up vast new opportunities for these systems. Contrary to expectation, devices based on interpenetrating networks of mesoscopic semiconductors have shown strikingly high conversion efficiencies, which compete with those of conventional devices

B.1 Device structure

The flexible embodiment of the hole conductor or solid electrolyte cell was shown already in Figure 5. It employs a thin titanium foil instead of the conducting glass as the current collector that supports the dye-derivatized TiO_2 nanocrystals. The deposition of the compact underlayer of TiO2 is not necessary for this device since a blocking layer of TiO2 is spontaneously formed by oxidation of the titanium foil. The counter electrode in this case is a transparent conducting plastic film.

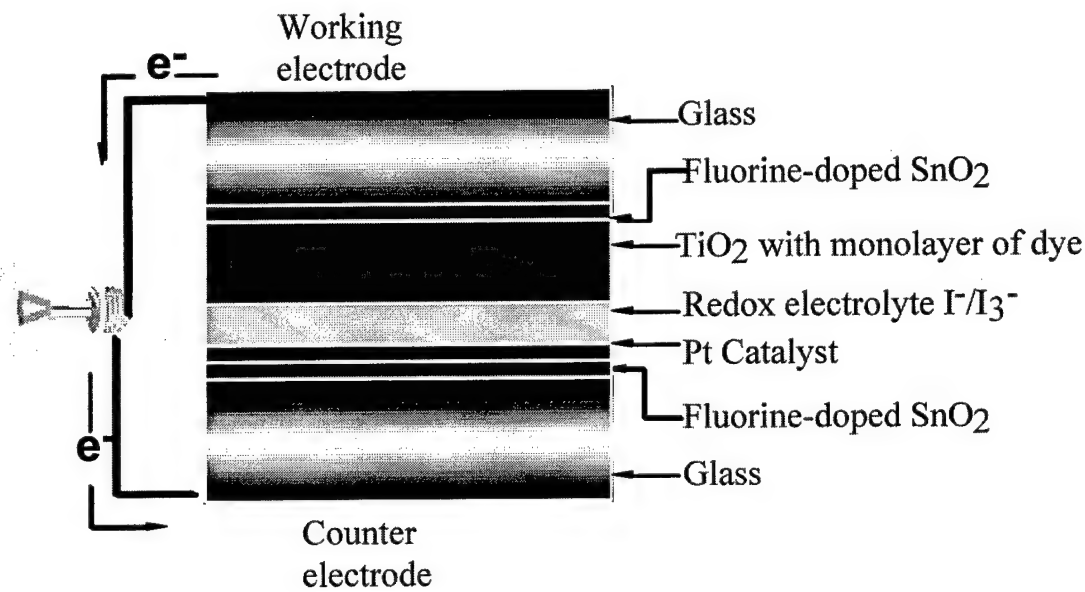

Figure 25: Device structure with rigid TCO collectors used to optimize DSC performance

For routine measurements aimed at performance optimization photovoltaic cells based on rigid TCO current collectors were also employed. The cell configuration is shown in Figure 25. The conversion efficiency of the two devices was found to be very similar, differences being caused mainly by the light transmission of the transparent counter-electrode and the light absorption by the triiodide containing electrolyte. In the following sections we shall provide details on the procedures applied to obtain the new record conversion efficiency of 10.6 percent shown in Figure 15.

B.2 Performance optimization

B.2.1 TiO2 particle synthesis, Preparation of 18-nm-Sized TiO_2 Colloid.

An amount of 12 g (0.2 mol) of acetic acid was quickly added to 58.6 g (0.2 mol) of titanium IV iso-propoxide (97%, Aldrich) under stirring at room temperature.The modified precursor was stirred for about 15 min and poured into 290 mL water as fast as possible with vigorous stirring (700 rpm). A white precipitate is instantaneously formed. One hour stirring was performed to achieve a complete hydrolysis reaction.

After adding 4 mL of 65% nitric acid, the mixture was heated from room temperature to 78 °C within 30 min and peptized for 120 min at the same temperature under reflux. Peptization begin 10 min after the colloid reach 78°C.Then, water is added to the cooling liquid mixture to adjust the volume to be 370 mL. The resultant mixture was kept in a 570 mL titanium autoclave and heated at 250 °C for 12 h (pressure : 70 atm !). After cooling down at room temperature the TiO2 colloid was aggregated and the pH was 2.5.

Subsequently, 2.4 mL of 65% nitric acid was added to reach pH 1.0 and dispersed with a 200 W ultrasonic titanium probe at a frequency of 30 pulses of 2 seconds during 2 minutes (repeated 3 times with stirring between series of pulses). The resultant colloidal solution was concentrated with a rotary-evaporator to contain 16 wt% TiO2. Finally, it was centrifuged to remove nitric acid and washed with ethanol three times. The particles were characterized by transmission electron microscopy and the results are shown in Figure 26.

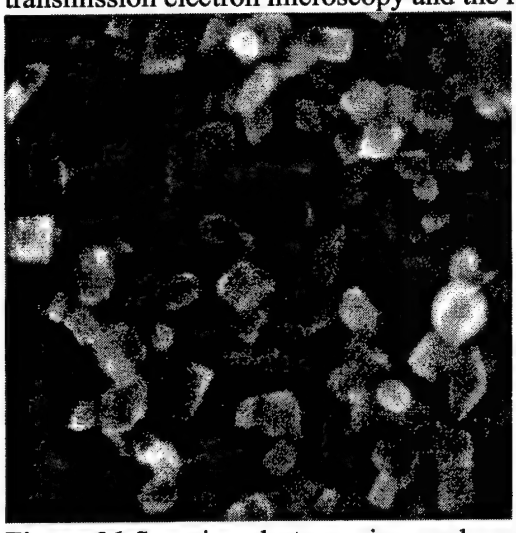

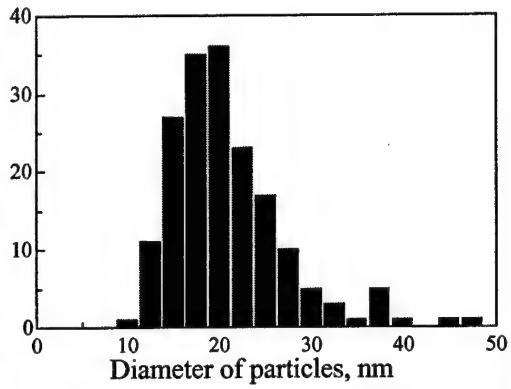

Figure 26 Scanning electron micrograph and particle size distribution for a TiO2 anatase colloid prepared at 230 °C, which has given optimal photovoltaic performance so far.

B2.2 Paste preparation for flexible solar cell

MIX41-S1 :

a Mixture of 82wt% TiO2 anatase 18nm colloid and 18 wt% anatase CCI 400 nm colloid.

1. 18 nm colloid in HNO3 0.1 M:

- concentrate to 16 wt% (16g TiO2 /100g colloid) in a rotavap apparatus at 50°C and 70 Torr.
- add 200 ml ethanol in order to flocculate the TiO2.
- transfer to 2 tubes for centrifugation and centrifuge 30 min at 5000 rpm. After remove the supernatant
- add in each tube 100 ml ethanol and redisperse roughly with a spatula and ultrasonic –bath (10 min).
- centrifuge again.
- Repeat the washing and centrifugation one more time (3 centrifugations in total)
- Transfer the TiO2 precipitate to Büchi vessel

2. <u>CCI 400nm colloid in water pH 2.6</u>
   - put 17.6 g CCI 400nm at 20wt% (3.5g TiO2) in a tube for centrifugation and add 50 ml ethanol
   - centrifuge and wash 3 times with 50 ml ethanol like the 18 nm colloid
   - add the 400nm colloid precipitateto the 18 nm colloid in the Büchi vessel (vol 1 liter)

3. <u>Paste preparation :</u>
   - add 35g EthylCellulose 30-50 mPas (Fluka) at 10wt% in ethanol.
   - add 49g EC 5-15 mPas at 10wt% in ethanol
   - add 56.9 g terpineol anhydrous (mixter of isomer, Fluka)
   - add ethanol to a total volume of 300 ml
   - break big and sticky aggregates with a spatula
   - put the Büchi vessel on a magnetic stirrer and stirr over night at 40°C.
   - disperse with an ultra fast mixer at 15000rpm 1 minute
   - disperse with an ultrasonic probe (200W) 2 min by pulses of 2 sec and intervals 2 sec.
   - Repeat the mixing and ultrasonic probe 2 times more.
   - Evaporate ethanol with a rotavap at 50°C and 120 to 30 Torrs (increase the vacuum with time), until all ethanol is evaporated.
   - Homogenize on a 3 roll-mill 2 times 15 min.

4. <u>Paste composition :</u>

TiO2	16g+3.5g	23 wt%
EC 30-50	3.5g	4.1 wt%

EC5-15	4.9g	5.8 wt%
Terpineol	56.9g	67.1 wt%

5. Films thickness:

   8 μm on screen 36T and 4.5 μm on screen 61T (61 wires/cm)

   Thickness for high efficiency flexible cell on titanium foil :
   20 – 21 μm, 2 x 8μm on 36T and 1 x 4.5 μm on 61T

B.2.3 Sensitizer preparation

The procedures applied for the synthesis and purification of the dye are reported in detail in appendix 1 of this report. Here we restrict ourselves to present a typical example for the heteroleptic hydrophobic ruthenium complex Z-907 whose structure coded N3_2C9 was shown in Figure 20.

In a typical one pot synthesis of Z-907, $[RuCl_2(p\text{-cymene})]_2$ (0.1 g, 0.16 mmol) was dissolved in DMF (50 ml) and to this solution dnbpy (0.133 g, 0.32 mmol) was added. The reaction mixture was heated to 60 °C under nitrogen for 4 h with constant stirring. To this reaction flask H_2dcbpy (0.08 g., 0.32 mmol) was added and refluxed for 4 h. Finally, excess of NH_4NCS (13 mmol) was added to the reaction mixture and continued the reflux for another 4 h. The reaction mixture was cooled down to room temperature and the solvent was removed by using rotary-evaporator under vacuum. Water was added to the flask and the insoluble solid was collected on a sintered glass crucible by suction filtration. The solid was washed (5 □ 20 ml) with pH 12 aqueous solution, distilled water and diethyl ether and dried. On a Sephadex LH-20 column the complex was further purified with methanol as an eluent. ^1H NMR (δ_H/ppm in CD_3OD) 9.72 (d, 1H), 9.28 (d, 1H), 9.08 (s, 1H), 8.92 (s, 1H), 8.55 (s, 1H), 8.42 (s, 1H), 8.28 (d, 1H), 7.88 (d, 1H), 7.70 (t, 2H), 7.40 (d, 1H), 7.05 (d, 1H), 2.95 (t, 2H), 2.75(t, 2H), 1.95 (m, 2H), 1.40 (m, 26H), 0.90 (t, 6H). Anal. Calc. for $RuC_{42}H_{52}N_6O_4S_2$: C, 57.99; H, 5.98; N, 9.66%. Found: C, 57.90; H, 5.97; N, 9.61%.

B.2.4 Electrolyte preparation

Two electrolytes were employed either in liquid form or solid form. Solidification was achieved by adding the copolymer polyvylinidene fluoride/hexafluoropropylene (PVDF-HFP) whose structure was shown above on page 7. The addition of the gelling agent did not affect significantly the performance of the device. The electrolytes had the following composition.

Electrolyte 6197
0.60M BMII, 0.02M I2; 0.5 tBuPy, 0.10 GRh, AN:VN (85:15)

Electrolyte 6141
0.60M BMII, 0.03M I2; 0.5 tBuPy, 0.10 GRh, AN:VN (85:15)

The abbreviations signify:

BMII: 1-butyl-3-methyl-imidazolium iodide (synthesized according to our published procedure)
I2: Iodine (Merck, Suprapure)
4-tBuPy: 4-tert.-butyl pyridine (Fluka, distilled on a Fischer Spaltrohr apparatus)
GRh,: Guanidiniumthiocyanate (Aldrich, recrystallized)
AN,: acetonitrile (Merck Uvasol)
VN : (Fluka, distilled on a Fischer Spaltrohr apparatus)

B.2.5 Preparation of counterelectrodes

Previous work at LPI has indicated that the iodine/triiodide reduction reaction is not reversible on all materials indiscriminantly, this including Pt. The kinetics are solvent dependent, being most facile in water and acetonitrile and increasingly more sluggish in all other organic solvents tested in the lab, also evidenced by the wide variation of exchange current densities reported on smooth platinum cathodes extending over three or four orders of magnitude. In view of the use of multicomponent organic electrolytes in our photovoltaic cells there is a need to minimize the energy efficiency losses and the performance limitations imposed on the system by iodine reduction on the counterelectrode (CE).

The specific temperature regime and procedure developed here for the thermal decomposition of platinum-chloride precursors (platinum-bromide or possibly other Pt compounds) from anhydrous isopropanol (or possibly other organic solvents), produces an electrode interface that is a selective catalyst for iodine/triiodide reduction in organic electrolytes, matching the kinetics reported in aqueous iodide/iodine systems. This technology produces catalytic electrodes that are electrochemically/chemically stable in their operating environment, in addition to providing superior mechanical endurance or robustness, good adherence to substrate. The catalyst has been structurally characterized as nanosized platinum metal clusters. The very low platinum loadings (less than $3\mu g/cm^2$), render these electrodes optically transparent and economy in the quantity of platinum used is an additional advantage.

However, the application of the catalyst is limited so far to the substrates that can withstand the high temperature preparation conditions required. The heating stage of the catalyst formation (385 ^oC) is tolerated by F doped SnO2 coated glass surfaces or layered graphite sheets, but not so well by e.g. polymer based laminated surfaces, which may exhibit low sheet resistance at room temperature, though will warp or oxidize when heated. Therefore, a low temperature catalyst preparation is indispensable to the promotion of other substrates as candidates for the further development of solar cells of particular characteristics or of broader design/construction options.

Under a recent development project, the desire to impart flexibility to the solar panel, has led to significant modifications of the materials comprising the photoelectrode: the mesoporous TiO2 layer was deposited on Ti metal sheet. This obviously obstructs the photoelectrode illumination of the cell, which should now be back-side illuminated. In turn, the success of CE illumination mode rests on the very low optical absorbance of the CE in the useful range of the spectrum combined with sufficiently high triiodide kinetics and finally long term performance stability of the electrode. The above challenges formed the objectives of this work.

Moreover, flexible Pt and Ti/Pt sputtered-polymer based sheets were envisaged for use as CE and were tested for kinetic performance as received (no treatment or conditioning), in solid polymer type electrolyte.

In order to fulfill the requirements of low temperature surface catalysation, CE flexibility, in addition to transparency (minimum absorbance of the solar spectrum by the CE for back-side illumination cell development), conducting polymer laminated flexible as well as transparent sheets (M. Cevey) have been surface catalyzed by the conducting polymer Pedot, using a variety of preparation techniques/conditions and were subsequently tested for their kinetics performance under electrochemically controlled conditions, in addition to applied as CE in experimental sealed and open solar cell performance tests.

Pedot and the Pedot/polystyrene sulfonate water dispersion commercial product found novel applications to CE fabrication, solar cell tests were conducted with Pedot electrochemical preparations on TCO glass or other cast surfaces, and graphite/Pedot/Pss composite pastes were developed with very low sheet resistance, intending to solve limitations due to the series resistance, kinetic resistance and low temperature CE casting directly on the prepared photoelectrode plate.

i) Experimental methods

Electrochemical impedance spectroscopy was employed on symmetric thin-layer cells, in order to determine the kinetic performance of the electrodes. The experimental cells, in brief, consisted of two conducting glass plates of approx. 1 cm^2 which were configured as a sandwich using a 20 micron thick mylar separator with an opening of 0.1 cm^2 cut into it. The charge transfer resistance R_{ct} value of the electrode under study, can be taken as the half of the real component of the impedance, which appears as the semicircle at the high frequency end of the spectrum. The labeled 'Maxell' solid polymer electrolyte was used for the catalytic activity evaluations as reflecting the optimum in the electrolyte state-of-the- art.

Electrochemical preparation of Pedot was done using the Edot monomer solution (10 mM) in acetonitrie and in the presence of 0.1M N-ethyl,-N-methyl-imidazolium imide as electrolyte. Cyclic voltammetry and chrono-coulometry were applied to produce the electropolymerization of Edot. The voltammetry in Figure 27 depicts the anodic (>1V AgCl) electropolymerization of Edot to Pedot on a conducting electrode substrate. The verification of the Pedot on the electrode surface was consequently performed by the voltammetric cycling (Figure 28) in the vicinity of the less positive de-doping potential, where the normally reversible doping current peaks would appear. Alternatively, the chrono-coulometric (or amperometric) pulse deposition of Pedot was applied, typical current profiles of which are shown Figure 28.

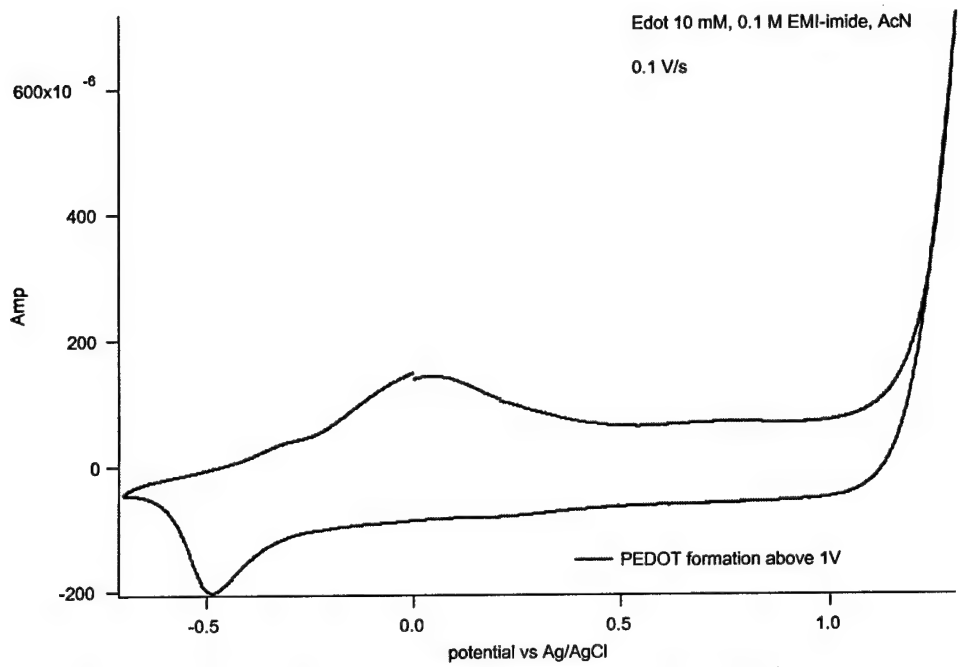

Figure 27: current voltage profile for Edot electropolymerization

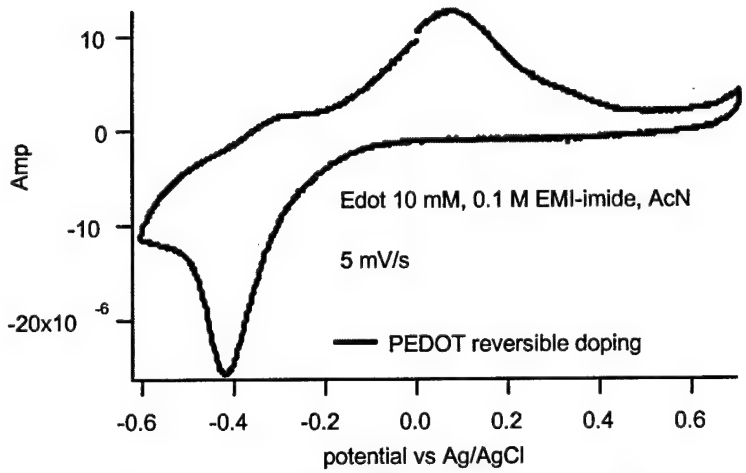

Figure 28: Pedot reversible doping by cycling the potential

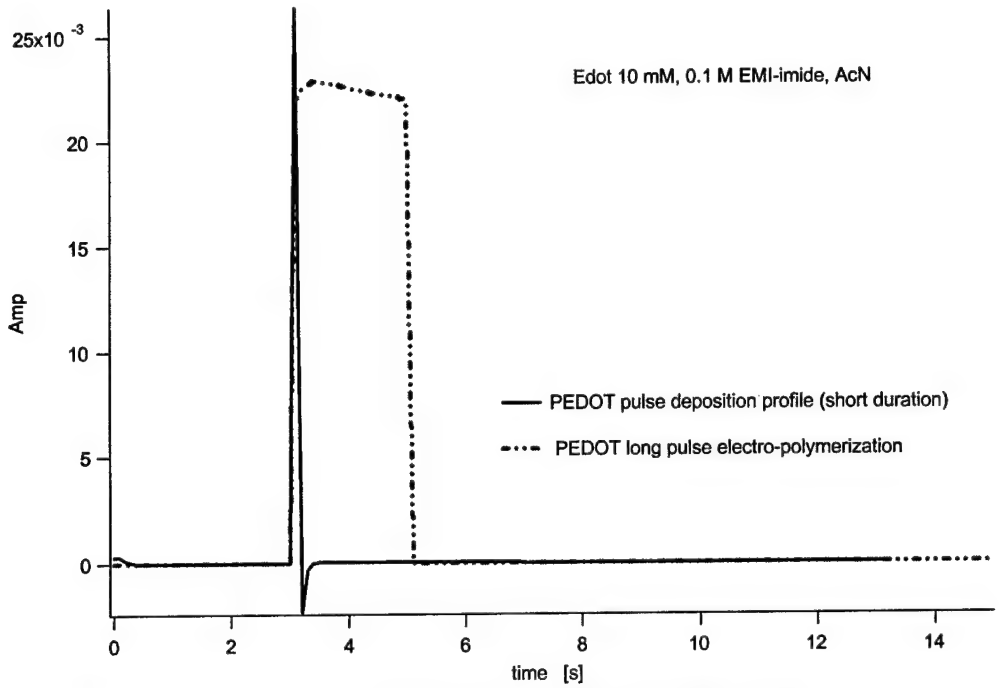

Figure 29. Electrodeposition of Pedot by applying a voltage pulse

ii) Experimental results and discussion

The required performance characteristics of the CE are determined by the maximum current delivered by the solar cell under short circuit conditions, which current nanocrystalline photoanode technology limits at $20mA/cm^2$. Considering a tolerance for the voltage loss on the counter-electrode as being < 10mV, one arrives at a $R_{ct} < 0.5$ Ohm cm^2 threshold for the charge-transfer resistance. This value corresponds to an exchange current density $J_o > 2.6x10^{-2}A/cm^2$ on the basis of the formula $R_{ct}=RT/nFJ_o$, which assumes the linear approximation of the current-overpotential equation, where n=2 for reaction $I_3^- + 2e = 3I^-$.

a) Flexible sputtered Pt / polymer sheet CE (source Konarkatech) testing for catalytic activity:

A multiply-regenerated thermal cluster catalyst on TCO glass served as the electrode of reference for kinetic performance comparisons. The above described impedance technique gave an average value of 1.75 Ohm cm^2 for the kinetic resistance per electrode in Maxell electrolyte. The corresponding value for the sputtered Pt on polymer laminate received (unspecified) varied between 3.6 – 5.0 Ohm cm^2. The electrocatalysis evaluation experiments were conducted under the same conditions as the thermal reference sample and no surface preparation, rinsing, polarization or electrochemical conditioning was performed on the received test samples.

A second set of electrodes received were specified as Pt5A, Pt5ATi5A and Pt10ATi5A, which presumably were alternate multi-layer coatings of 5 to 10 Angström of sputtered Pt and Ti metal, as denoted by their name. The recorded kinetic resistance values were as follows:

Pt5A: 6.2, Pt5ATi5A : 5.3 and Pt10ATi5A: 14.5 Ohm cm^2

It is noteworthy that the refreshing of the electrolyte in the thin-layer test cell produced lower kinetic resistance for the series as e.g. for the case of Pt10ATi5A, 14.5 initially decreased to 7.5 in a subsequent run of the same test. This phenomenon may also suggest that a chemical surface pretreatment involving iodide or even pure organic solvent could substantially improve the as received catalytic performance of such layer preparations.

b) Surface catalysis by electrochemical Pedot deposition.

The first attempts to catalyze the rigid cto surface with electrochemically prepared Pedot consisted in the *in situ* electro-polymerization of the Edot monomer in organic solution. The working cto electrode was cycled between 0.5 and 2V AgCl and the gradual build up of the blue surface coating was observed. The dedoping of the conducting doped material was observed at –0.4V thus verifying the doped (and less colored) state of the produced deposits. This method produced blue colored electrode surfaces with poor mechanical strength, albeit with reasonable catalytic activity (4 Ohm cm^2) as also confirmed by the feedback from LPI co-workers with data from solar cell I-V tests. The uniformity of the deposit was not always good and unclean cto surfaces were very prone to incomplete coatings and blemishes. Additionally, the control of the Pedot loading was not possible at low levels and therefore unsuitable for the preparation of transparent layers. In conclusion, the dendritic growth of the pedot resulted in poor adhesion to the substrate and the total Pedot mass had a considerably low dispersion over the surface, thus reducing the strength and the quality of the catalyst.

Transparent coatings were produced using a pulse technique, such as chrono-coulometry for very short times i.e. below 1s, e.g. 0.3 s at 5-10 mA/cm2 could produce light coatings that were acceptable in terms of absorbance (M.Cevey absorbance tests) as well as in kinetic performance (Cevey-P. Liska sealed cell tests). These catalyst depositions could be done on any flexible electrode supplied with ease and reproducibility. The independent impedance evaluation of week old deposits gave 4 – 5 Ohm cm^2 depending on the loading. It was also observed that freshly made electrodes had better performance in the solar cell (< 3 Ohm cm^2 by impedance). The pulse deposition improved markedly the mechanical strength of the layer and its resistance to abrasion.

However, there are still lingering questions regarding the longer term stability of this successful performance. It must be said that although the operational potential of the CE within the solar cell (ca. 0.1V AgCl) is far enough positive to the dedoping limit of the material, thus avoiding the direct electrochemical dedoping to the non-conducting state, Pedot has been reported as being able to form charge transfer complexes with iodine.

For standard measurement on flexible cells the transparent counter electrode consisted of an ITO layer on a PEN (poly-ethylenenaphthalate) substrate. The Pt was electro-deposited form a solution of 5 mM $H_2PtCl_6.6H_2O$ in water. The voltage applied was 1.8 V and the duration of the galvanic deposition was 20 –60 s.

B.2.6 Assembly of flexible cells.

The titanium foil used as current collector for the anode had a thickness of 32 micron and was supplied by Konarka. It was cleaned in an ultrasound bath first in water and than technical grade ethanol.

At first a 200 nm thick layer of compact TiO2 was deposited on the foil by spray pyrolysis as described in section A.2.2(iii). Subsequently a 18 –19 nm thick layer of the TiO2 nanoparticles (MIX-41) was deposited by screen printing as outlined above and sintered for 15 minutes at 500 °C The film was finally activated by treatment with a 5x 10^{-2} M solution of TiCl4 in water (applied volume 65 µl/cm2) in the oven for 30 minutes at 70°C.

The films was immersed for 2 days in a solution of 3.5 x10^{-3} M N-719 dye (proton content 1.5 H^{+}/molecule) to ascertain complete adsorption of the sensitizer. The electrode was laminated with the ITO/PAN counter-electrode using Surlyn as an adhesive. The electrolyte was filled through a hole that was drilled in the titanium foil.

Acknowledgement.

We thank the European Office of the U.S. Air Force for supporting this work under contract No F61775-00-C0003

Appendix 1

Engineering of Efficient Sensitizers for Nanocrystalline TiO_2 -Based Solar Cells

Md. K. Nazeeruddin and M. Grätzel

Contents | Page number

Appendix 1	1
Contents	1
1. Introduction, Principles and Definitions	**4**
1.1. Dye-sensitized Solar Cell Fabrication	4
1.2. Operating Principles of the Dye-sensitized Solar Cell	6
1.3. Incident Photon to Current Efficiency	8
1.4. Open Circuit Photovoltage	8
1.5. Fill Factor	9
1.6. Power Conversion efficiency	9
1.7. Solar Radiation and Air Mass	9
1.8. Photophysical Properties of Metal Complexes	9
2. Red sensitizers	**11**
2.1. Synthesis	11
2.1.1. Apparatus and Chemicals	11
2.1.2. Synthesis of ligand 4,4'-dicarboxy-2,2'-bipyridine ($dcbpyH_2$) (N1)	11
2.1.3. Synthesis of cis-dichloro bis(4,4'-dicarboxy-2,2'-bpy)Ru(II), (N2)	12
2.1.4. Synthesis of cis-dithiocyanatobis(4,4'-dicarboxy-2,2'-bpy)Ru(II), (N3)	13
2.1.5. Synthesis of (N712).	14
2.1.6. Synthesis of (N719)	14
2.2. Purification of N-3 and N719	15
2.2.1. Materials	15
2.2.2. Column packing	15
2.2.3. Sample preparation and indroduction onto the column	15
2.2.4. Isolation of the product	16
2.3. Characterization	16

2.3.1. Physical properties 16
2.3.2. Electronic spectroscopy 17
2.3.3. Emission studies 19
2.3.4. Determination of pK_a. 19
2.3.5. Electrochemistry 23
2.3.6. NMR Spectroscopy 24
2.3.7. ^{13}C NMR 25
2.3.8. HPLC data 26
2.3.9. Resonance Raman data 27
2.3.10. FTIR studies 28
2.3.10.1. Photoacoustic FTIR spectra 28
2.3.10.2. Surface chelation 30
2.3.11. Thermal behavior of the dyes 33
2.3.11. 1. Thermal behavior of the free dyes 33
2.3.11.2. Thermal behavior of the dyes on TiO_2 38
2.3.12. Photovoltaic performance 38
2.3.12.1. Influence of protons on power conversion efficiency of the cell 38
2.3.12.2. Effect of LH-20 column Purification on photovoltaic efficiency 39
3. Hydrophobic Sensitizers **43**
3.1. Synthesis 43
3.1.1. Materials 43
3.1.2. Synthesis of $[Ru(H_2dcbpy)(dmbpy)(NCS)_2]$ N820 43
3.1.3. Synthesis of $[Ru(H_2dcbpy)(dhbpy)(NCS)_2]$ N823 44
3.1.4. Synthesis of $[Ru(H_2dcbpy)(dnbpy)(NCS)_2]$ Z907 44
3.1.5. Synthesis of $[Ru(H_2dcbpy)(tdbpy)(NCS)_2]$ N621 44
3.2. Characterization 45
3.2.1. Synthetic Studies 45
3.2.2. NMR spectral data 47
3.2.3. $^{13}CNMR$ 48
3.2.4. ATR-FTIR Spectral data 49

3.2.5. Electronic Spectra 49
3.2.6. Emission Spectra 51
3.2.7. Electrochemical data 52
3.2.8. Photovoltaic performance 54
3.2.9. Photovoltaic stability 56
4. Ruthenium sensitizers with antenna and extended π-system 58
4.1. Synthesis 58
4.1.1. 4,4'-di-(2-hydroxy-2-(3-methoxyphenyl)ethyl)-2,2'-bipyridine 58
4.1.2. 4,4'-di-(2-(3-methoxyphenyl) ethenyl)-2,2'-bipyridine (DMPEbpy) 59
4.1.3. Synthesis of [Ru(H_2dcbpy)(BMPEbpy)(NCS)$_2$] (Z910) 60
5. Panchromatic Ruthenium Sensitizers 61
5.1. Synthesis 61
5.1.1. 4',4''-Diethoxycarbonyl-2,2':6',2":6",2'"-quaterpyridine 62
5.1.2. Synthesis of [Ru(L^1)Cl_2] 62
5.1.3. Synthesis of [Ru(L^1)(SCN)$_2$] 62
5.2. Characterization 63
5.2.1. Synthetic Studies 63
5.2.2. NMR Spectroscopy Studies 63
5.2.3. IR spectral data 63
5.2.4. Electrochemical Studies 64
5.2.5. Electronic Spectra 64
5.2.6. Emission Spectra 64
5.3. Photovoltaic data 65
6. New sensitizers 66
References 68

1. Introduction, Principles and Definitions

The dye-sensitized solar cell technology developed at EPFL contains broadly five components: (1) conductive mechanical support, (2) semiconductor film, (3) sensitizer, (4) electrolyte containing I^-/I_3^- redox couple, and (5) counter electrode with a platinum catalyst.[1] A cross section of the dye-sensitized solar cell is shown in Figure 1. The total efficiency of the dye-sensitized solar cell depends on optimization and compatibility of each of these components constituents. To a large extent, the nanocrystalline semiconductor film technology along with the dye spectral responses is mainly responsible for the high efficiency.[2-4] The high surface area and the thickness of the semiconductor film yield increased dye optical density resulting in efficient light harvesting. The sensitizers display a crucial role in harvesting of the sunlight. To trap solar radiation efficiently in the visible and the near infrared region of the solar spectrum requires engineering of sensitizers at a molecular level.[4] The electrochemical, photo-physical properties of the ground and the excited state of the sensitizer plays significant influence on the charge transfer dynamics at the semiconductor interface.[5] In this ***appendix*** we concisely illustrate dye-sensitized solar cell fabrication and definitions, and comprehensively synthetic protocols and characterization of various sensitizers developed at EPFL.

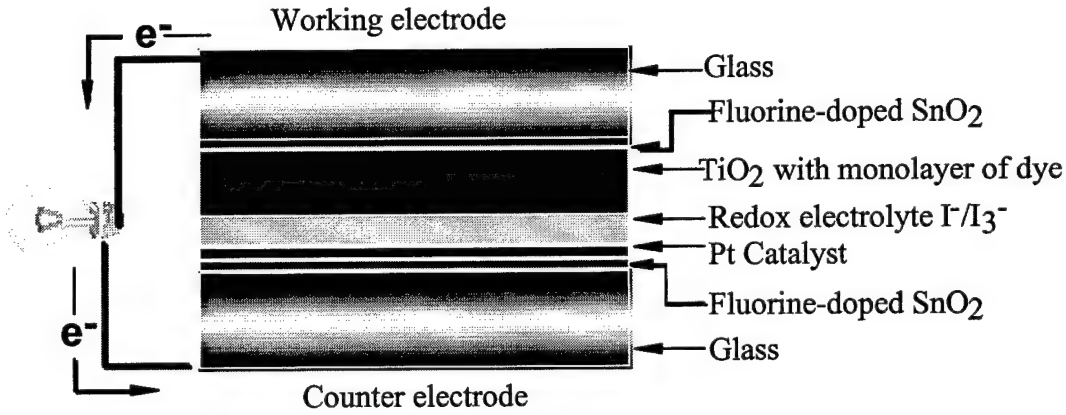

Figure 1. Schematic representation of the cross section of a dye sensitized solar cell.

1.1. Dye-sensitized Solar Cell Fabrication

An optimized colloidal suspension of TiO_2 was produced using a hydrothermal technique, developed at EPFL.[6] The advantage of this procedure is the ease of control of the particle size, the nanostructure and the porosity of the resultant semiconductor substrate. The procedure

involves the hydrolysis of the titanium alkoxide precursor producing an amorphous precipitate followed by peptisation under in acid or alkaline water conditions to produce a sol, which is subjected to hyrdrothermal Ostwald ripening in an autoclave. The temperature of the hydrothermal treatment has a decisive influence on the particle size and on pore size distribution. The standard sol, treated for about 12 hours at 230 °C in the autoclave has an average particle diameter of 15 nm and the most frequent pore size is about 10 nm.

The nanocrystalline TiO_2 films were prepared by depositing TiO_2 colloids on a transparent fluorine doped tin oxide conducting glass using either screen-printing or by the doctor blade technique. The films are then dried in air and fired at 450°C. The hot electrodes (≈80°C) were immersed into the dye solution, which were usually prepared in ethanol (2-5 ► 10^{-4} M). The dye deposited film is used as a working electrode. A sandwich cell was prepared with a second conducting glass coated with chemically deposited platinum from 0.05M-hexachloroplatinic acid.[7] The platinum coated counter electrode, and the dye coated TiO_2 film is then put together with a thin transparent film of Surlyn polymer frame (DuPont). The sandwiched electrodes were tightly held and then applied heat (130°C) around the Surlyn frame to seal the two electrodes. A thin layer of electrolyte containing I_3^-/I^- redox active couple in methoxyacetonitrile was introduced into inter electrode space from the counter electrode side through pre-drilled holes. The drilled holes were sealed with microscope cover slide and Surlyn to avoid leakage of the electrolyte solution. A representative module of photoelectrochemical solar cell based on dye sensitized TiO_2 nanocrystalline film is shown in Figure 2.

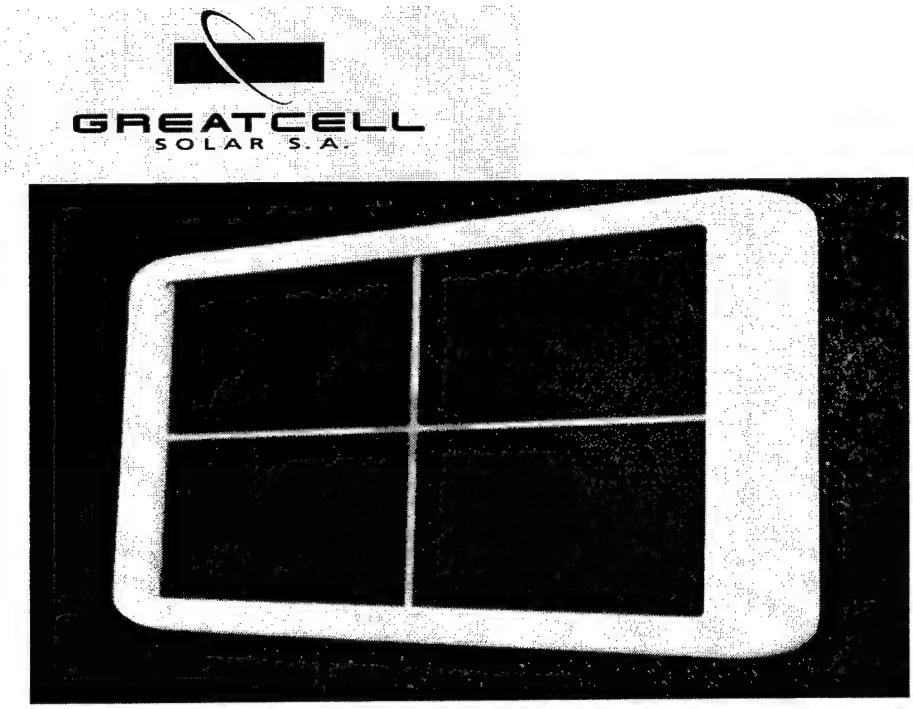

Figure 2. A module of photoelectrochemical solar cell based on dye sensitized TiO_2 nanocrystalline film

1.2. Operating Principles of the Dye-sensitized Solar Cell

The details of the operating principles of the dye-sensitized solar cell are given in Figure 3. Photo-excitation of the metal to ligand charge transfer of the adsorbed sensitizer (equation I) leads to injection of electrons into the conduction band of the oxide (equation II). The oxidized dye is subsequently reduced by electron donation from an electrolyte containing the iodide/triiodide redox system (equation III). The injected electron flows through the semiconductor network to arrive at the back contact and then through the external load to the counter electrode. At the counter electrode, reduction of triiodide in turn regenerates iodide (equation IV) through the donation of electrons from the external circuit, which completes the circuit. With a closed external circuit and under illumination, the device then constitutes a photovoltaic energy conversion system, which is regenerative and stable. However, there are undesirable reactions, which are the injected electrons may recombine either with oxidized sensitizer (equation V) or with the oxidized redox couple at the TiO_2 surface (equation VI) resulting losses in the cell efficiency. For a net forward current under study state illumination processes (II) and (III) must be kinetically more favorable than (V) and (IV).[8]

$$S_{(adsorbed\ on\ TiO_2)} + h\upsilon \longrightarrow S^*_{(adsorbed\ on\ TiO_2)} \quad (I)$$

$$S^*_{(adsorbed\ on\ TiO_2)} \longrightarrow S^+_{(adsorbed\ on\ TiO_2)} + e^-_{(injected)} \quad (II)$$

$$S^+_{(adsorbed\ on\ TiO_2)} + 3/2\ I^- \longrightarrow S_{(adsorbed\ on\ TiO_2)} + 1/2\ I3^- \quad (III)$$

$$I3^-_{(cathode)} + 2e^- \longrightarrow 3I^-_{(cathode)} \quad (IV)$$

$$S^+_{(adsorbed\ on\ TiO_2)} + e^-_{(TiO_2)} \longrightarrow S_{(adsorbed\ on\ TiO_2)} \quad (V)$$

$$I3^- + e^-_{(TiO_2)} \longrightarrow I3^-_{(anode)} \quad (VI)$$

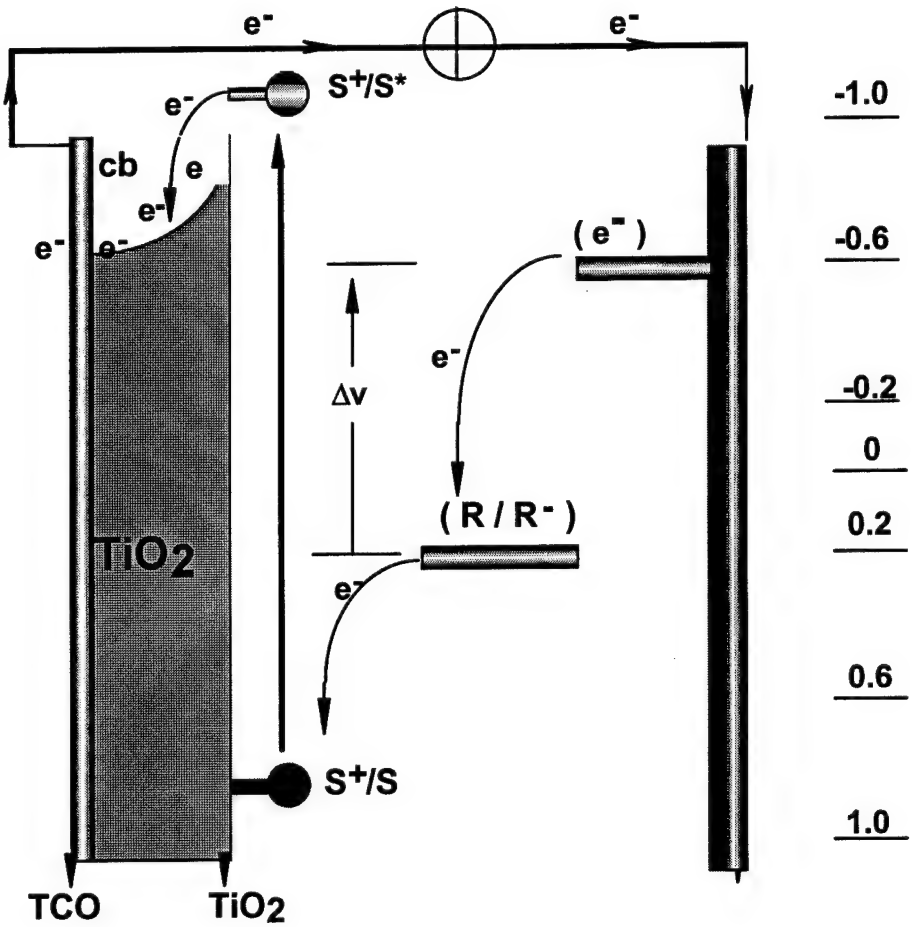

Figure 3. Operating principles and energy level diagram of dye-sensitized solar cell. $S / S^+ / S^*$ = Sensitizer in the ground, oxidized and excited state, respectively. R/R^- = Redox mediator (I^-/I_3^-).

1.3. Incident Photon to Current Efficiency

The incident monochromatic photon-to-current conversion efficiency (IPCE), also called external quantum efficiency defined as the number of electrons generated by light in the external circuit divided by the number of incident photons as a function of excitation wavelength is expressed in the equation (VII).[9] In most cases, the photo-action spectrum overlaps with the absorption spectrum of the sensitizer adsorbed on the semiconductor surface. A high IPCE is a prerequisite for high power photovoltaic applications, which depends on the sensitizer photon absorption, excited state electron injection and electron transport to the terminals.

$$\mathbf{IPCE} = \frac{[(1.25 \times 10^3) \times \text{photocurrent density } [mA/cm^2]]}{[\text{wavelength } [nm] \times \text{photon flux } [W/m^2]]} \qquad \textbf{(VII)}$$

1.4. Open Circuit Photovoltage

The origin of the open-circuit potential (V_{oc}) in dye sensitized solar cells is the subject of much discussion.[10] However, grossly it can be determined by the energy difference between the fermi level of the solid under illumination and the Nernst potential of the redox couple in the electrolyte (Figure 3). The experimentally observed open-circuit potential for various sensitizers is smaller than the difference between the conduction band and the redox couple, likely due to the competition between electron transfer and charge recombination pathways. The decrease in the rate constants for triiodide reduction (k_{et}) at photo-anode should decrease in the dark current and thereby an increase in the open circuit voltage of the cell. For regenerative photoelectrochemical systems, equation (VIII) holds, where I_{inj} is the flux of charge resulting from sensitized injection and n_{cb} is the concentration of electrons at the TiO_2 surface.

$$V_{oc} = (kT/e) \ln (I_{inj} / n_{cb}\, k_{et}\, [I_3^-]) \qquad \textbf{(VIII)}$$

Knowledge of the rates and mechanisms of these competing reactions are vital for the design of efficient sensitizers and thereby improvement of the solar devices.[11-13] Surface modifications also influence significantly the open circuit potential. For example, treatment of dye coated electrodes with base such as ammonia or tert-butyl pyridine increases the open-circuit potential by 200–300 mV due to band edge shift coupled with reduced charge recombination dynamics. On the other hand treatment of the TiO_2 electrodes with small cations such as Li^+ or

H^+ decreases the open circuit potential substantially. This dependence has been attributed to the influence of such ions on the energetics of the TiO_2 conduction band, (relative negative shift of the conduction band edge induced by the adsorption of these cations onto the surface) and therefore on the energetic of electron injection.[14]

1.5. Fill Factor

The fill factor is obtained by dividing the product of current and voltage measured at the power point by the product of short circuit current and the open circuit voltage. The power point is the maximum product of the cell voltage and the photo current obtained on the $I - V$ plot (see figures 25 and 27 for $I - V$ plots). The open circuit voltage (V_{oc}) is the potential of the illuminated electrode, where the short-circuit current (I_{sc}) is zero.

1.6. Power Conversion efficiency

The overall conversion efficiency (η) of the dye-sensitized solar cell is determined by the photocurrent density (i_{ph}) measured at short circuit, the open circuit potential (V_{oc}), the fill factor (ff) of the cell and the intensity of the incident light (I_s) as shown in equation (IX).

$$\eta global = i_{ph} V_{oc} ff / I_s \qquad \text{(IX)}$$

1.7. Solar Radiation and Air Mass

Specific solar radiation conditions are defined by the *Air Mass* (*AM*) value. The spectral distribution and total flux of radiation outside the Earth's atmosphere, similar to the radiation of a black body of 5900 K, has been defined as AM-0. The AM-1 and AM-1.5 are defined as the path length of the solar light relative to a vertical position of the sun above the terrestrial absorber, which is at the equator when the incidence of sunlight is vertical (90°) and 41.8°, respectively. The AM-1.5 conditions are achieved when the solar flux is 982 Wm^2. However, for convenience purpose the flux of the standardized AM-1.5 spectrum has been corrected to 1000 Wm^2.

1.8. Photophysical Properties of Metal Complexes

The photophysics and photochemistry of polypyridyl complexes of ruthenium can be understood with the aid of the energy diagram shown in Figure 4. In these complexes there are three possible excited states: (a) metal centered (MC), which are due to promotion of an electron from t_{2g} to e_g orbitals; (b) ligand centered (LC) that are π-π^* transitions; and (c) charge transfer (CT) excited states, which are either metal-to-ligand (MLCT) or ligand-to-metal (LMCT). An electronic transition from metal t_{2g} orbitals to empty ligand orbitals without spin change allowed, is called a singlet-singlet optical transition. The allowed transitions are identified by large extinction

coefficients. The transitions with spin change are termed singlet-triplet optical transitions, which are forbidden and are usually associated with a small extinction coefficient. However, the excited singlet-state may also undergo a spin flip, resulting in an excited triplet state. This process is called intersystem crossing (ISC). The possible de-excitation processes are radiative and nonradiative. The radiative decay of a singlet and triplet excited states are termed fluorescence and phosphorescence, respectively.[15]

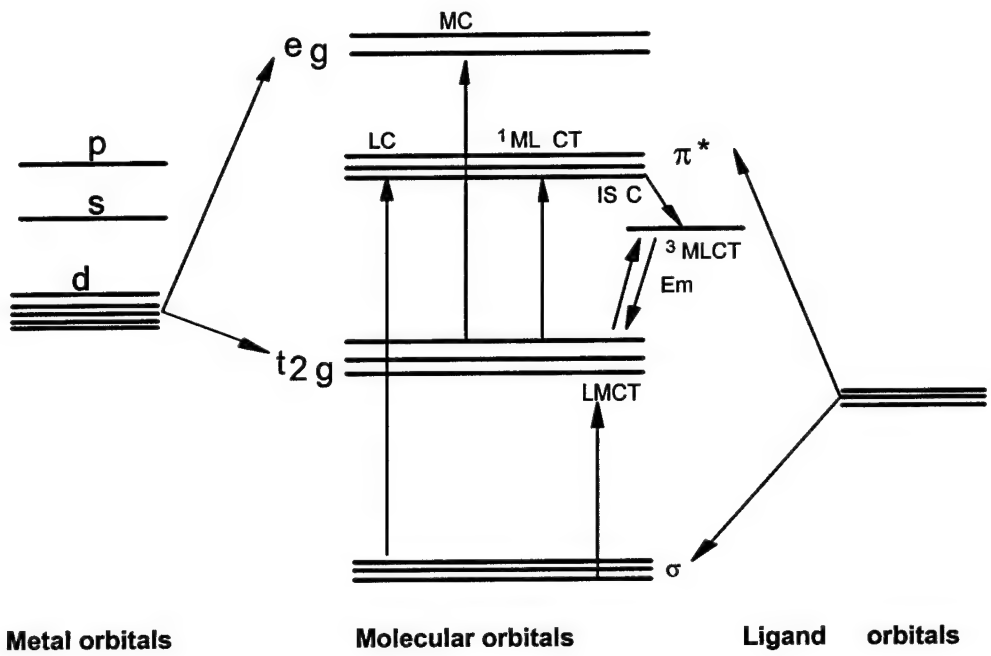

Figure 4. Schematic presentation of a molecular orbital diagram for an octahedral d^6 metal complex involving 2,2'-bipyridyl type ligands in which, various possible transitions are indicated.

The intense colors in 2,2'bipyridyl complexes of iron, ruthenium and osmium are due to excitation of an electron from metal t_{2g} orbitals to the empty π* orbitals of the conjugated 2,2'bipyridyl. The photo-excitation of this metal-to-ligand charge transfer excited state can lead to emission. However, not all complexes are luminescent because of the different competing deactivation pathways.[15-19] The other potential deactivation pathways for the excited dye are donation of an electron (oxidative quenching, equation X) or the capture of an electron (reductive quenching, equation XI) or transfer of its energy to other molecules or solvent (equation XII).

$$D^* + Q \longrightarrow D^+ + Q^- \qquad (X)$$

$$D^* + Q \longrightarrow D^- + Q^+ \quad \text{(XI)}$$

$$D^* + Q \longrightarrow D + Q^* \quad \text{(XII)}$$

The excited state redox potential of a sensitizer plays an important role in the electron transfer process. An approximate value of the excited state redox potential can be extracted from the potentials of the ground state couples and the zero-zero excitation energy (E_{0-0}) according to equations (XIII) and (XIV). The zero-zero energy can be obtained from 77 K emission spectrum of the sensitizer.[20]

$$E(S^*/S^-) = E(S/S^-) + E_{0-0} \quad \text{(XIII)}$$

$$E(S^+/S^*) = E(S^+/S) - E_{0-0} \quad \text{(XIV)}$$

2. Red sensitizers

2.1. Synthesis

2.1.1. Apparatus and Chemicals

Oil bath, hot plate with a stirrer, silicone oil, beakers, conical and round bottom flasks, magnetic-bars and glass rods of various sizes, thermometer, filtration unit, sintered glass (G4) crucibles, Buchner funnel, filter-papers, water vacuum pump, 4,4'-dimethyl-2,2'-bipyridine, $K_2Cr_2O_7$, H_2SO_4, HCl, KOH, NaOH, MeOH, acetone, diethyl ether, ethanol, DMF, rotary evaporator and hydrated ruthenium trichloride.

2.1.2. Synthesis of ligand 4,4'-dicarboxy-2,2'-bipyridine ($dcbpyH_2$) (N1)

Method A

Reaction:

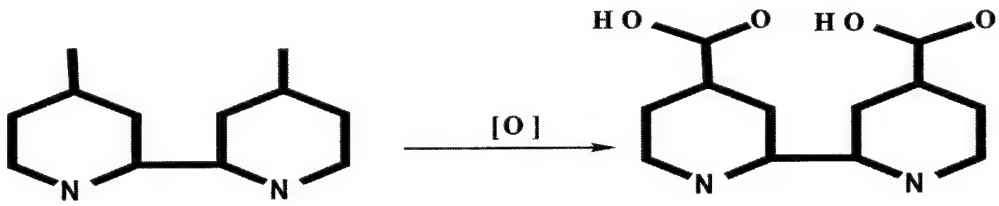

Procedure: The ligand 4,4'-dicarboxy-2,2'-bipyridine (N1), is synthesized by a modification of the Sasse method.[21] 15.0 g of 4,4'-dimethyl-2,2'-bipyridine is dissolved in 800 mL of 4 M H_2SO_4 and cooled in an ice-salt bath to -5 °C. To this solution 32 g of solid $KMnO_4$ is added in

6 portions over a period of 10 minutes while stirring. After an additional half an hour of stirring at the same temperature, another 32 g of $KMnO_4$ is added in a similar manner. The cooling bath is removed and the reaction mixture is heated under reflux on a silicone oil bath for 18 hours with stirring. The mixture is then cooled to room temperature and filtered by suction using a Buchner funnel. The black solid is dissolved in 800-1000 mL of 1 M Na_2CO_3 solution and filtered at atmospheric pressure, through a filter paper supported on a Buchner funnel. The pH of this filtrate was lowered to 2 by slow addition of a 1:1 mixture (by volume) of CH_3COOH and 4 M HCl. The precipitated white solid is collected on a fine porosity sintered glass funnel (G-4) and dried under vacuum at room temperature. Yield 9-9.5 g (45 - 48% of crude ligand).

The ^1H and ^{13}C NMR spectra show that the product contains less than 2 % of 4-methyl-4'-carboxy-2,2'-bipyridine (based on integration of the methyl resonance peak at □ 2.28 against an aromatic doublet at □ 8.78 ppm). The formation of this by-product can be reduced to < 0.01% by further refluxing the crude compound in 500 mL of 6 M HNO_3 solution for 18 hours. Then, the solution is poured into a 1-L beaker containing 600 g of ice cubes and the resulting $dcbpyH_2$ ligand. The white solid is collected on a sintered glass crucible (G-4) and dried under vacuum at room temperature. Yield 8.8 g (44% of the crude ligand).

Method B

To a stirring solution of concentrated H_2SO_4 (125 mL) in a 250 mL beaker, is added slowly 4,4'-dimethyl-2,2'-bipyridine (5 g, 27.1 mmol), while cooling to maintain 25°C. After the addition of all the solid then added $K_2Cr_2O_7$ (24 g, 81.5 mmol) in small portions with efficient stirring such that the temperature remains around 70-80°C (Occasional cooling in a water bath is usually necessary during the addition of $K_2Cr_2O_7$). After the addition of all the $K_2Cr_2O_7$ stirring was continued until the temperature fell below 40°C. At this stage the green viscous reaction mixture was transferred into a beaker containing 500–800 g of ice. A green solid precipitates during the process and settles. Decanted the supernatant liquid and the rest of the product filtered through a sintered glass crucible. The solid was washed with water thoroughly and dried under vacuum. The pale yellow precipitate was suspended in 200 mL of 50% HNO_3 and refluxed for 18 hours. Then the reaction flask was allowed to cool and add was poured into 500 mL of water containing 500 g of ice. The beaker was kept at 5°C for 5 hours. The separated white solid was filtered and dry under vacuum. Yield 6.2 g.

2.1.3. Synthesis of cis-dichloro bis(4,4'-dicarboxy-2,2'-bpy)Ru(II), (N2)

Reaction:

$$RuCl_3(H_2O)_3 + L \xrightarrow[N_2/\,Ar]{DMF} RuL_2(Cl)_2$$

1 mol 1.95 mol

Procedure

Note: The synthesis and all the manipulations should be carried out in reduced light to avoid possible trans isomerization.

Reagent grade N,N'dimethylformamide (500 mL) is added to a 2000 mL three necked, round-bottomed flask fitted with a reflux condenser, a magnetic stir bar and a gas inlet. 5.23 g (0.02 mol) of $RuCl_3(H_2O)_3$ is dissolved in DMF under Argon. After stirring for 15 minutes another 500 mL of DMF is added. To this solution 9.52 g (0.039 mol) of 4,4'-dicarboxy-2,2'-bipyridine ligand as a solid is added. The flask is wrapped completely with aluminum foil and then immersed in an oil bath maintained at 170 - 180 °C. The reaction mixture is refluxed with vigorous stirring for 3 hours in an oil bath at 180 °C. (The temperature is important: at lower temperatures the reaction time significantly increases). The progress of the reaction is monitored by Uv-vis spectra. A small aliquot of the reaction mixture is sampled and diluted with an absolute ethanol (concentration $\approx 1\times10^{-4}$ mol). The Uv-vis absorption spectrum of this solution shows maxima at 565, 414 and 316. At the end of the reaction the relative intensities of these maxima show 1: 1.05 : 3.33. After reaching these ratios ($\approx$ 3 h) refluxing is suspended, while maintaining stirring for a further 1 hour. The reaction mixture is passed through a sintered glass crucible. The solvent DMF is evaporated completely on a rotary evaporator under vacuum. The resulting air stable solid product is stirred in 100 mL of 2 M HCl for 4 hours in darkness and filtered through a sintered glass crucible. After drying, the yield is 11.4 g (86%).

Analysis for $[RuL_2(Cl)_2]$, C 24, H16, N4, O8, Cl2, Ru, Calculated (%) C, 43.67; H, 2.44; N, 8.48; Cl, 10.74: Found: C, 44.02, H, 2.58, N, 8.90; Cl, 10.74.

2.1.4. Synthesis of cis-dithiocyanatobis(4,4'-dicarboxy-2,2'-bpy)Ru(II), (N3)

Reaction:

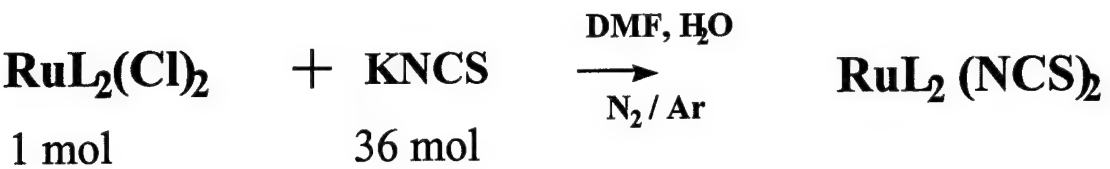

Procedure

58.2 g (0.6 mol) of KNCS is dissolved in 100 mL of distilled water and transferred into a 2000 mL three-necked flask. To this solution, 500 mL of DMF is added and purged with Ar for 15 minutes. 11.0 g (0.017 mol) of $[RuL_2(Cl)_2]$ as a solid is introduced into the flask in darkness, followed by another 500 mL of DMF solvent. The flask is covered with an aluminum foil and refluxed (Oil bath temperature 150°C) for 5 hours. The reaction mixture is allowed to cool and then filtered through a sintered glass crucible, grade 4. The DMF and water solvents are removed using rotary-evaporator under high vacuum. To the resulting viscous liquid, is added 50 mL of water. To this aqueous solution is added ≈ 100 mL of 0.5 M NaOH to give a dark purple-red homogeneous solution. The solution is filtered and the pH of this solution is lowered to 3.3 with a 0.5 M HNO_3 solution giving a dense precipitate. The flask is placed in a refrigerator for 12 hours at -4 °C. After allowing it to reach room temperature the solid is collected on a sintered glass crucible by suction filtration. Washed (3 x 20 mL) with pH 3.5 water, that is prepared with the same acid as previously used and air dried. Yield 9.0 g (85%).

Analysis for the $[RuL_2(NCS)_2].4(H_2O)$ C 26, H24, N6, O12, S2, Ru, Calculate in (%) C 40.15; H 3.11; N 10.80; S 8.24: Found: C 39.65, H 3.13, N 10.53; S 8.67.

2.1.5. Synthesis of tetrakis tetrabutylammonium *cis*-dithiocyanatobis(-2,2'-bipyridine-4,4'-$(COO^-)_2$)Ru(II), (N712).

0.5 g of the complex N3 was introduced into a 250 ml conical flask containing 50 ml of distilled water. To this solution was added dropwise 10% tetrabutylammoniumhydroxide solution till the pH of the solution shows a stable reading of pH 7. At this stage, the solution was filtered through a sintered glass crucible and the solvent was removed on a rotary-evaporator. The resulting viscous liquid was dissolved in methanol and precipitated by the addition of 1:1 diethyl ether and petroleum-ether mixture. The precipitated hygroscopic solid was dried under vacuum for 24 hours.

Analysis for the $(TBA)_4[RuL_2(NCS)_2].4(H_2O)$ C 90, H162, N10, O12, S2, Ru, Calculated C 62.07; H 9.38; N 8.04. Found: C 61.85, H 9.03, N 7.93.

2.1.6. Synthesis of bis tetrabutylammonium *cis*-dithiocyanatobis-2,2'-bipyridine-4-COOH,4'-COO⁻- ruthenium(II), (N719).

Complex N719 is a nonhygroscopic air stable solid, which is the doubly protonated species of complex N712. It was obtained by titrating complex N712 with a 0.05 M nitric acid solution. In a typical synthesis, 1 g. of complex N712 was weighed into a 100 ml round bottom flask and dissolved in 10 ml of distilled water. The pH of this solution was lowered to 4.3 by the addition of 0.05 M nitric acid. At this pH most of the complex precipitates out and the flask was kept in a refrigerator for 12 hours at –5°C. The flask was allowed to warm to room temperature (25°C), and the precipitate was collected on a sintered glass crucible. The isolated solid was washed once with 5 ml of water. Yield 0.6 g (80%).

Analysis for the $(TBA)_2(H)_2$ $[RuL_2(NCS)_2].4(H_2O)$ C 58, H92, N8, O12, S2, Ru, Calculated C 53.5; H 7.5; N 8.61. Found: C 53.65, H 7.47, and N 8.93.

2.2. Purification of N-3 and N719

2.2.1. Materials

N3 or N719 (0.2g)

Tetrabutylammonium thiocyanate (0.2 g)

Tetrabutylammonium hydroxide 30-Hydrate (0.82 g)

Sephadex LH 20 (70 g)

Chromatography Gravity column with a Teflon stopcock. The column size is 45 cm length and 3 cm internal diameter.

2.2.2. Column packing

Sephadex LH 20 (70 g) gel was placed into 1000 ml conical flask containibg 600 ml of water and was allowed to swell for 24 h. The water was decanted and another 500 ml of distilled water was added then the gel was added to the column with gentle tapping (Note: the gel should not be stirred with a magnetic stir bar, which reduces the flow rate significantly).

2.2.3. Sample preparation and indroduction onto the column

N-3 (0.2 g) was dispersed in 4 ml of water in a 10 ml flask to which was added a solution of tetrabutylammonium hydroxide 30-Hydrate (0.82 g) with stirring. Then was added tetrabutylammonium thiocyanate (0.2 g). After stirring few minutes, the solution was filtered using a G4 sintered glass crucible. The filtered solution was charged onto the column with a glass pipette. Distilled water was used for elution. Figure 5 illustrates the separation of different bands.

There are two minor bands, which separate from the main band. The final separation between the main band to the minor one is 5 cm. The main fraction absorption spectrum shows three bands at 310, 372 and 502 nm, the 372 nm band optical density is 4% lower than the 500 nm band.

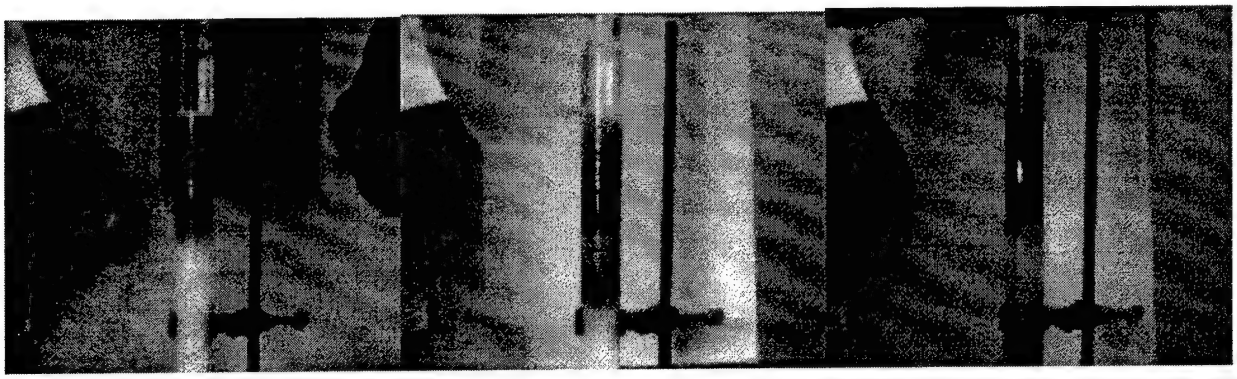

Figure 5. Purification of N3 dye on a Sephadex LH-20 column

2.2.4. Isolation of the product

The main fraction was collected into a conical flask. The pH of the solution shows 10-12, which was lowered to pH 4.3 with a 0.05 M HNO_3 acid solution. At this pH most of the complex precipitates and the flask was kept in a refrigerator at –5°C for 12 hours. After allowing the flask to room temperature, the separated solid was collected on a G4 sintered glass crucible. The solid was dried under vacuum for 12 hours. Yield 80%. The nmr spectrum of the isolated product shows that the complex contains two protons and two tetrabutylammonium cations. Scheme 1 shows chemical structures of N3, 719 and 712 dyes. The separated product N719 was purified using the same conditions for two times more in order to obtain the best photovoltaic performance (see Figures 26 and 27 in photovoltaic section).

2.3. Characterization

2.3.1. Physical properties. In solid state the complexes N3, N719 and N712 are stable in air at 35 °C and can be stored in a drawer for months. These complexes are highly soluble in DMF, DMSO, methanol and alkaline water. The chloride ligands in complex N2 are labile and forms diaqua complex in water and solvento complexes in coordinating solvent like DMSO.

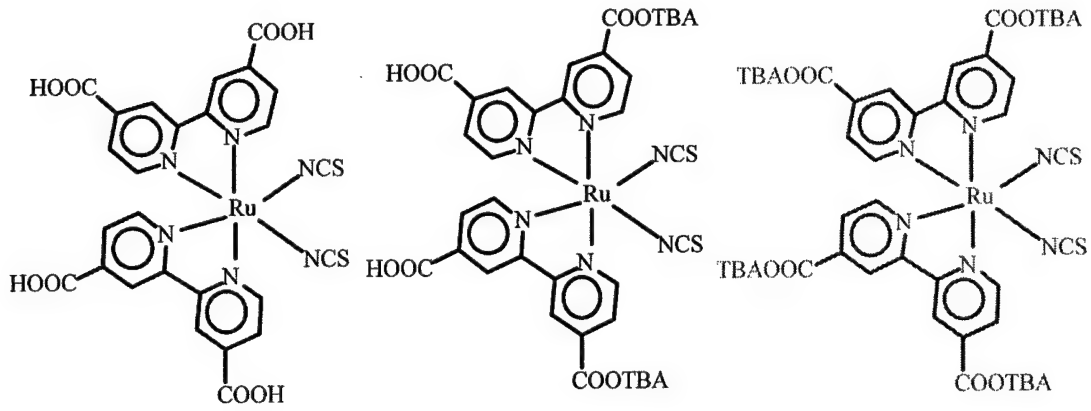

N3 N719 N712

Scheme 1

2.3.2. Electronic spectroscopy. Figure 6 show a comparison of the absorption spectra of N3, N719 and N712 complexes in ethanol solution. The two broad visible bands in N3 at 538 and 398 nm are assigned to metal-to-ligand charge-transfer (MLCT) origin. The bands in the UV at 314 nm with a shoulder at 304 nm are assigned as intra ligand (π-π^*) charge transfer transitions.[22] Deprotonation of the COOH groups blue shifts the (π-π^*) charge transfer band from 314 to 308 nm (not shown in the figure) and the low energy MLCT band shifted to higher energy by 20 nm, from 538 to 518 nm. The blue shift is due to an increase in the energy of the LUMO of the ligand, causing the (π-π^*) and dπ-π^* transitions to occur at higher energies.[23] On the other hand, the low energy MLCT band in N719 complex blue shift only by 3 nm (535 nm) compared to the N3 complex because the LUMO in N719 is already dictated by the presence of two protonated COOH groups similar to the N3.

The absorption spectra of the three complexes anchored on 7-μm thick TiO_2 nanocrystalline electrode were shown in Figure 7. The low energy MLCT maximum in N712 is considerably red shifted upon adsorption onto TiO_2 nanocrystalline electrode compared to the solution spectra.[24] This is due to the fact that on the electrode the carboxylate groups bind to the TiO_2 surface in which Ti^{4+}acts as proton. The position of the low energy MLCT band of N3 and N719 complexes in solution and anchored on TiO_2 nanocrystalline electrode is very similar because of the presence of protons in solution and Ti^{4+} in the adsorbed state. It is interesting to note that the rate of adsorption for N3 is much faster than the N719, which in turn is faster than the N712. For N712, dye adsorption on TiO_2 was very slow even if the dye concentration is 1

mM, due to its high solubility in organic solvents, which displaces the equilibrium between adsorption and desorption. Nonetheless, the dye loading increased significantly by increasing the dye concentration 100 times that shifts the equilibrium.[25]

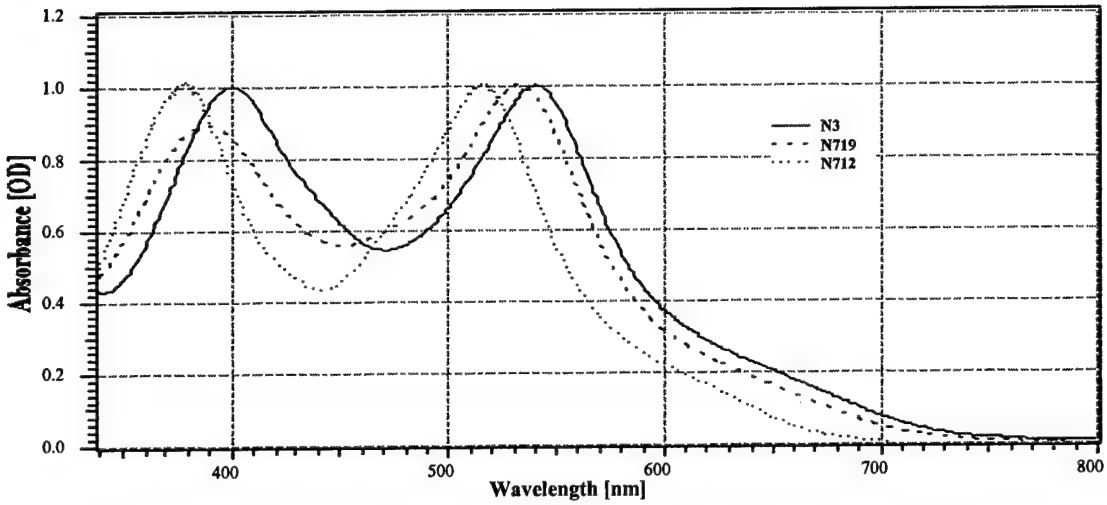

Figure 6. Absorption spectra of N3, N719 and N712 dyes in ethanol solution

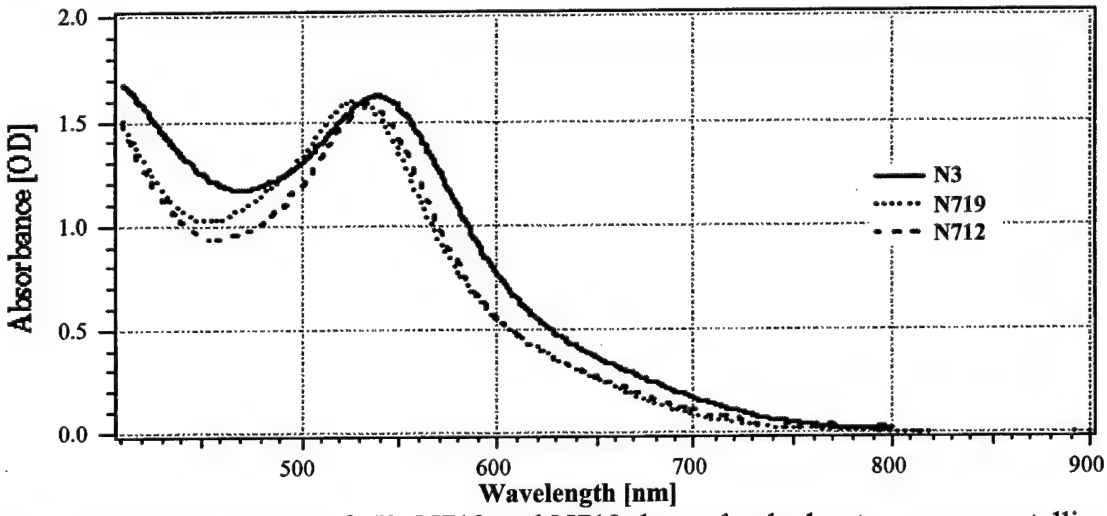

Figure 7. Absorption spectra of N3, N719 and N712 dyes adsorbed onto a nanocrystalline 7 μm thick TiO_2 films.

The absorption and emission spectral properties of complex N712 as a function of solvent polarity are gathered in Table 1. The most intense lowest energy MLCT feature in N712 varies from 500 nm (in H_2O), 510 nm (in CH_3CN) to 540 nm (in C_3H_7CN). The observed 40 nm blue shift in water compared to C_3H_7CN could be due to the combination of two factors. Firstly, due to the H-bonding of solvent molecules to the lone pair electrons of the thiocyanato sulfur, as previously noted for cyanocomplexes of Ru and other related systems.[26] Secondly, the

interaction of the dielectric constant of the solvent with the change in dipole in the excited state of the dye is known to show solvatochromism.[27] It is interesting to note that the variation in energy/peak position of the MLCT bands of complex N712 in different solvents is significantly larger when compared to the π-π* bands.

Table 1. Absorption and emission spectral properties of complex N712 in different organic solvents at room temperature. The emission spectra of complex N712 was obtained by exciting at λ 510 nm .

Solvent	Abs. max.(nm)	Em. max.(nm)	Dielectric constant(e)
H_2O	500	720	100
CH_3CN	510	730	37.5
C_2H_5OH	518	750	24.55
C_2H_5CN	530	775	27.2
C_3H_7CN	540	800	20.3
1:1C_3H_7CN/C_2H_5CN	536	790	20.3 /27.2
DMSO	540	890	46.68

2.3.3. Emission studies. The complex N3 has an emission maximum at 813 nm, with a short excited state lifetime of 30 ns. The short excited state lifetime of complex N3 could be due to presence of protons on carboxyl groups enhancing the non radiative channel.[28] The emission quantum yield of complex N3 is 0.0004. On the other hand complexes N719 and N712 show a more intense luminescence at 770, 800 nm, respectively. The red shift of the low energy absorption and emission maxima of complex N3 compared to N719 and N712 is due to the lower π* orbital of 4,4'-dicarboxy-2,2'-bpy ligand in the protonated form. These assignments are further corroborated by the electrochemical studies. Solvent dependence of the emission maxima of the complex **3** has been gathered in table 1.

2.3.4. Determination of pK_a. The pK_a's of complex N3 were determined by UV-VIS and emission measurements over the pH range 1 - 11. A stock solution ($5x10^{-5}$ M) was prepared in

100 cm^3 of 5:1 H_2O / ethanol mixture containing 0.1 M $NaNO_3$. Since the neutral complex was insoluble in water 20% of ethanol was added in order to avoid the precipitation. The initial pH of the solution was adjusted to 11 by adding 0.2 M NaOH solution. The pH of the solution was lowered by the addition of HNO_3 solution. The acid was added in such away, that throughout the entire measurements the total volume of added acid was negligible. The UV-VIS spectrum of each solution was obtained after adding acid and allowing the solution to equilibrate for five minutes. The emission spectra were measured at room temperature by exciting into the lowest-energy MLCT band (550 nm).

The complex N3 at pH 11 shows visible MLCT bands at 500 and 370 nm, and the high energy π-π^* band at 308 nm. The ground state pK_a's can be determined from the relationship between the change in the optical density or the peak maximum with the pH for a given wavelength.[29] When acid is added to an alkaline solution of complex N3, changes in the electronic spectrum occur as shown in Figure 8. Upon lowering the pH from 11 to 1, the MLCT transition band shifts from 500 to 520 nm with three clean isosbestic points at 515, 406 and 380 nm. The intra-ligand transition shifts from 308 to 312 nm with an isosbestic point at 305 nm. Figure 9 shows the comparable titration curve, obtained by plotting the λ max (MLCT) change at 525, 400 and 310 nm vs. pH for complex N3. The plot shows the expected sigmoidal shape, with the pH at the inflection point giving the ground state pKa value of 3 ± 0.1 and another at pH 1.5 ± 0.1. These values we assign to the pK_{a1} and pK_{a2} of the dcbpy ligand.[30] Back-titration of the same solution quantitatively regenerated the original spectrum.

In complex N3 there are two 4,4'-dicarboxy-2,2'-bipyridine ligands which could give four separate acid base equilibria, if the dissociation is stepwise. On the other hand, if the dissociation were simultaneous one would expect one equilibrium constant. The fact that we observe two separate equilibria in complex N3, suggests that the pyridyl subunits are non equivalent. Scheme 2 presents the simplified two-step equilibrium of complex N3.

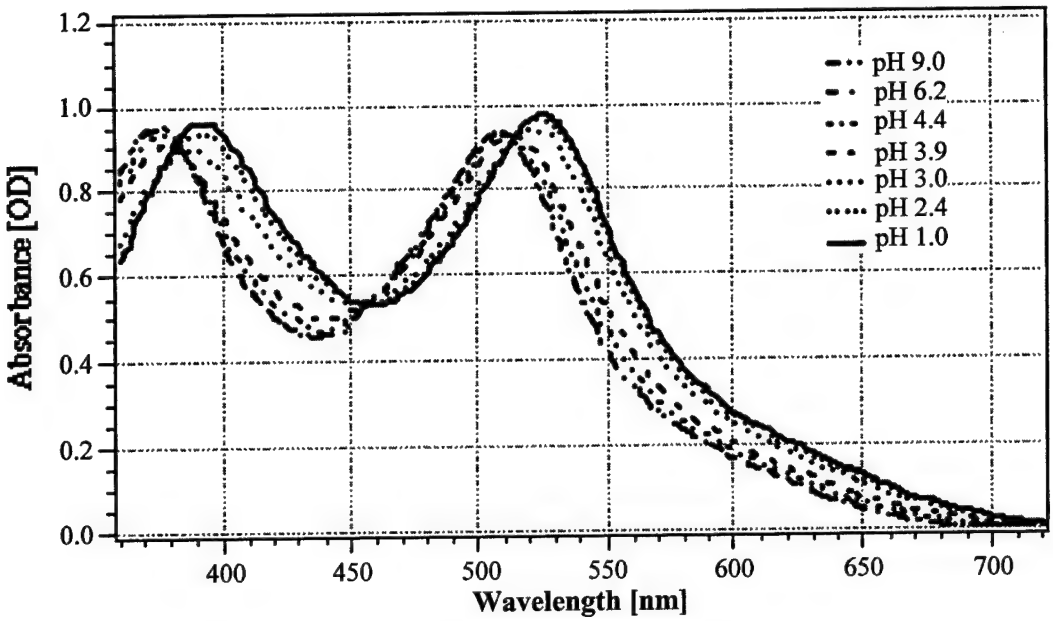

Figure 8. Absorption spectral changes of complex N3 as a function of pH at (1) pH = 1, (2) pH = 2.4, (3) pH = 3, (4) pH = 3.9, (5) pH = 4.4, (6) pH = 6.2 and (7) pH = 9.0.

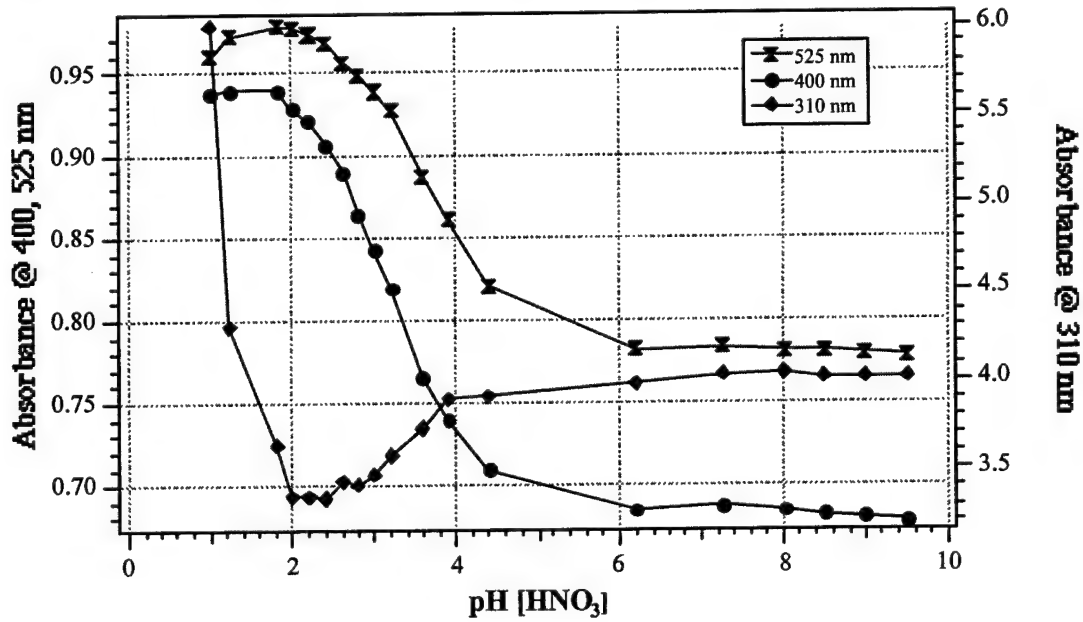

Figure 9. Plot of absorbance change as a function of pH in complex N3 at 310, 400 and 525 nm.

$$(NCS)_2Ru^{II}(COOH)_2(COO^-)_2 \underset{-\,2H^+}{\overset{pK_a2 = 1.5,\ +\,2H^+}{\rightleftharpoons}} (NCS)_2Ru^{II}(COOH)_4$$

$$(NCS)_2Ru^{II}(COO^-)_4 \underset{-\,2H^+}{\overset{pK_a1 = 3,\ +\,2H^+}{\rightleftharpoons}} (NCS)_2Ru^{II}(COOH)_2(COO^-)_2$$

Scheme 2

The excited state pK^*_a of complex N3 was obtained by spectrofluorimetric titration method. Complex N3 shows an emission maxima at 770 nm in alkaline pH and red shifts to 814 nm, upon lowering the pH to 1. Figure 10 shows the change in the emission intensity and maxima with pH. The emission intensity and lifetime decreases with decreasing pH.[30] Figure 11 shows a plot of the emission quantum yields as a function of the pH in water-ethanol solvent mixture for complex N3. The curve shows a single and sharp inflection point at pH = 3 to give an apparent excited state pKa*.

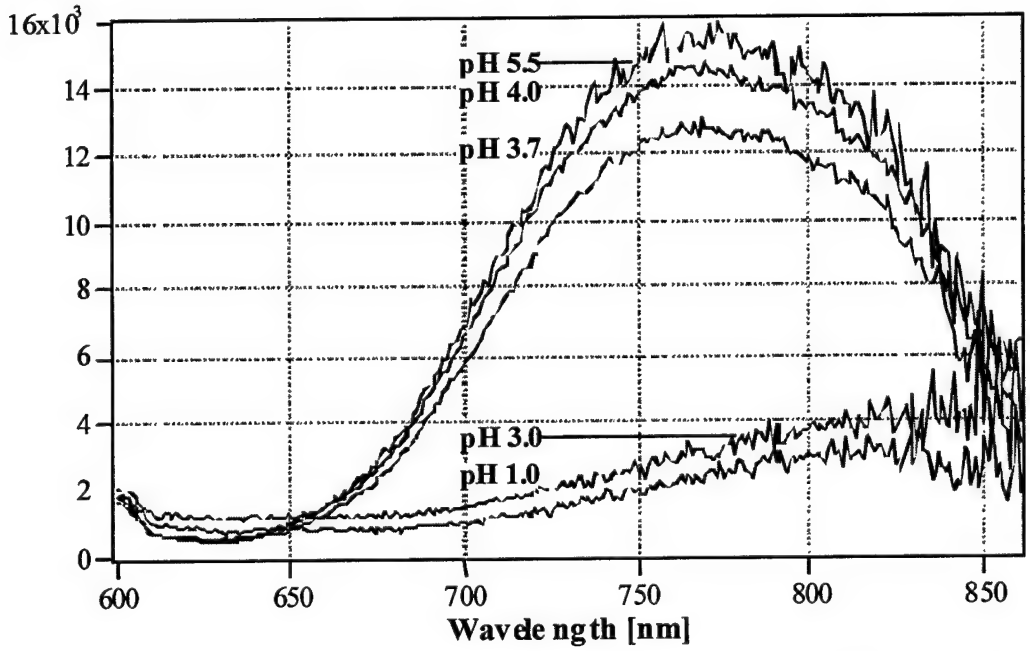

Figure 10. Emission spectral changes of complex N3 as a function of pH between = 1 to 5.5. For clarity purpose, spectral data at higher pH are not shown in the figure.

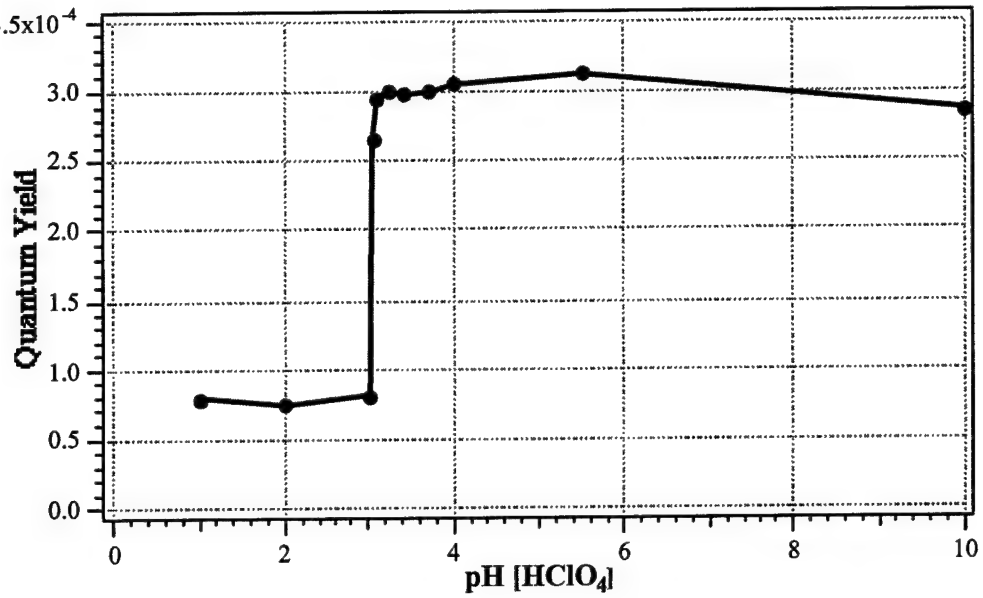

Figure 11. pH dependence of emission quantum yield in complex N3 in 4: 1 ethanol and H_2O mixture containing 0.1M NaCl, Excited at 490 nm

2.3.5. Electrochemistry. Cyclic voltammogram of complex N3 was measured in DMSO solvent with 0.1 M tetrabutylammonium trifluromethanesulfonate as supporting electrolyte in the potential range between +1.2 to -1.5 V. The complex N3 shows an irreversible oxidation wave at +0.85 V and a reduction wave at -1.27 V vs. SCE. They are due to the oxidation of Ru (II)/(III) and reduction of dcbpy, respectively. The irreversible oxidation wave could be due to the presence of thiocyanate groups whose oxidation potential is very close to the oxidation potential of Ru $^{(II)/(III)}$ in complex N3.

The cyclic voltammetry of complex N712 in acetonitrile shows a quasi reversible wave at 0.57 V vs SCE, which can be readily assigned to the Ru(II)/(III) couple (Figure 12). The oxidation wave is 2 times higher than the reduction wave, suggesting that the complex is not quantitatively regenerated on the time scale of the cyclic voltammogram. On the cathodic side, there is a reversible peak at -1.67 V vs SCE, assigned to the reduction of the dcbpy ligand. The Ru(II)/(III) couple in complex N712 is shifted ca. 290 mV negatively with regard to that of N3 complex due to the replacement of H+ by tetrabutylammonium cation. The negative shift for the dcbpy-based reduction potential is even larger, i.e., about 400 mV compared to that of complex N3. This is ascribed to the combination of two factors, i.e., the increase in the LUMO energy of the ligand caused by the deprotonation and electrostatic effects.

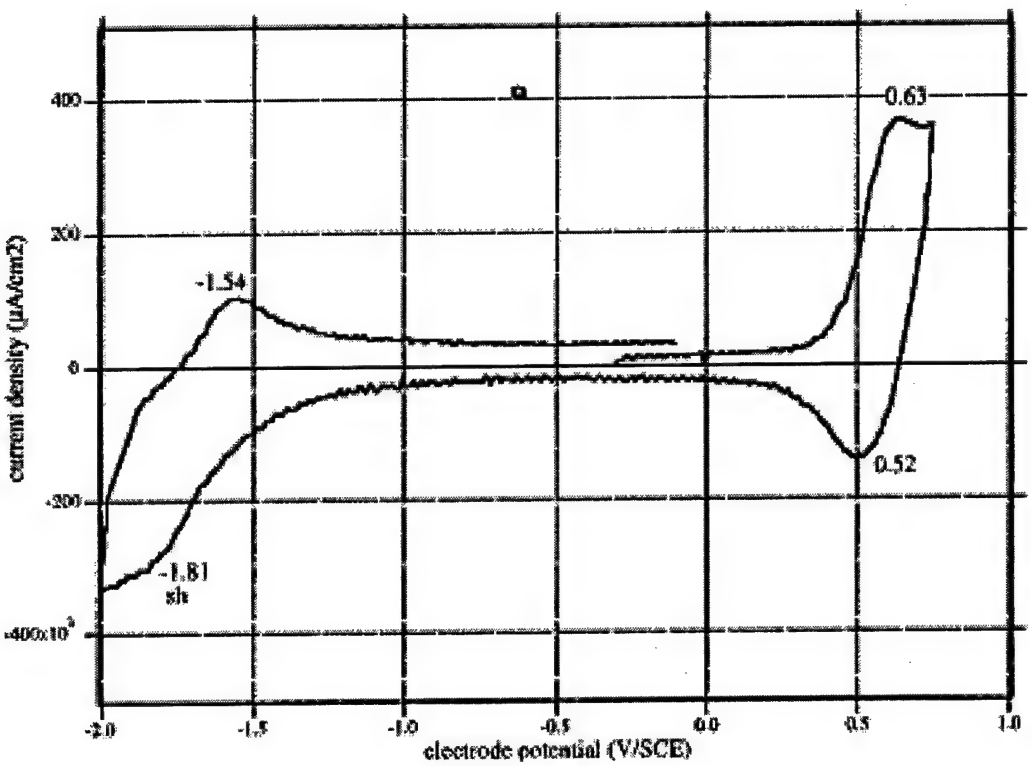

Figure 12. Cyclic voltammogram of complex N712 in CH3CN at room temperature under argon. The solution concentration is 1X10-3 M, with 0.1 M TBATFB electrolyte. The working electrode is a Pt microdisk of 25 *ím* diameter, and the scan rate is 50 V/s.

2.3.6. NMR Spectroscopy. Proton NMR spectral data of the ligand, N3, N719 and N712 are collected in Table 2. The NMR data of these complexes in CD_3OD solution shows 6 peaks in the aromatic region due to two different dcbpy ring protons, in which two pyridine rings are trans to the NCS ligands and the remaining two are trans to each other. The resonance peaks in the aliphatic region for complexes N719 and N712 are due to tetrabutylammonium cations. The integrated ratio of the aliphatic to aromatic protons shows the presence of two and four tetrabutylammonium cations in N719 and N712 complexes, respectively. The aromatic protons in N712 and N719 are high field shifted compared to the protons in N3 complex. The proton NMR spectra of the N3 complex isolated at pH = 2.5 show extra peaks at lower field, which are due to linkage isomers that are difficult to separate using either column or re-crystallization methods. However, it is striking to note the absence of linkage isomers in N719, which was isolated at pH 4.3. The reason for precipitation of N719 complex at pH 4.3 is the presence of bulky and hydrophobic tetrabutylammonium cations.

Complex/Ligand	6	6'	5	5'	3	3'
dcbpy	8.78 (d)		7.87 (dd)		8.40 (d)	
N2 [$RuL_2(Cl)_2$]	9.84 (d)	7.80 (d)	8.13 (dd)	7.39 (dd)	8.86 (d)	8.69 (d)
N3 [$RuL_2(NCS)_2$]	9.55 (d)	7.82 (d)	8.22 (dd)	7.52 (dd)	8.94 (d)	8.77 (d)
N719 [$RuL_2(NCS)_2$]	9.50 (d)	7.79 (d)	8.23 (dd)	7.55 (dd)	8.95 (d)	8.78 (d)
N712 [$RuL_2(NCS)_2$]	9.52 (d)	7.80 (d)	8.19 (dd)	7.49 (dd)	8.92 (d)	8.75 (d)
Cis [$RuL_2(H_2O)_2$]	9.38 (d)	7.78 (d)	8.18 (dd)	7.50 (dd)	8.90 (d)	8.74 (d)

Table 2. ^1H NMR data in aromatic region for the Ruthenium complexes and the ligand4,4'-COOH-2,2-bipyridine in D_2O solution containing 0.05 M NaOD. In ppm with respect to TMS.

2.3.7. ^{13}C NMR. The proton-decoupled carbon-13 NMR spectrum of complex N719 in the aromatic region is shown in Figure 13. The different carbon resonances in complex N719 were identified by comparison with known bipyridine complexes. The carbon-13 data are particularly useful in N3, N719 and N712 complexes for determining the NCS ligand coordination (N- or S-bonded). It has been reported that S coordination of the NCS ligand to transition metals shields the carbon atom much more than N coordination. S-coordinated NCS ligands show carbon resonances at 120- 125 ppm. The 13C NMR spectrum of complex N719 shows 12 resonance peaks (Figure 13) corresponding to two different pyridine rings and one single peak at 132.84 ppm that we assign to the carbon of N-coordinated NCS.[23] The downfield two resonances at 172.59 and 172.24 are assigned to the carboxylate carbons. There is a negative (1 ppm) chelation induced shift (CIS, compared to the free ligand) for the C-4 carbons because of $d\pi$ donation from the metal center to the ligand. However, C-2 and C-6 carbons show a significant CIS value, 4 ppm, because of the σ bonding formation from the lone pair of electrons on the nitrogen to the empty metal orbitals. The CIS values at C-5 and C-3 are smaller, 1 and 2 ppm, respectively. The two peaks at 159.7 and 158.6 are assigned to C-2 and C-2' carbons, which are near the electron-withdrawing nitrogen of coordinated pyridine. The remaining carbons were assigned on the basis of proton NMR data, and our assignments are consistent with the literature. Aliphatic carbons of tetrabutylammonium cations were observed at 54, 35, 16, and 9 ppm. The proton decoupled Carbon 13 NMR spectrum of N3 and N712 complexes in the aromatic region show similar pattern. Carbon-13 NMR shifts can be used to characterize the electron densities of the

corresponding carbon. The downfield two resonances at 172.59 and 172.24 in the N3 complex are assigned to the carboxylic acid carbons, which are slightly down field shifted compared to the N719 (168.25 and 168.03) ppm and N712 (167.55 and 167.23 ppm), respectively. The high field shift in the N712 complex reflect increase in the electron density due to replacement of electron withdrawing proton by tetrabutylammonium cations.

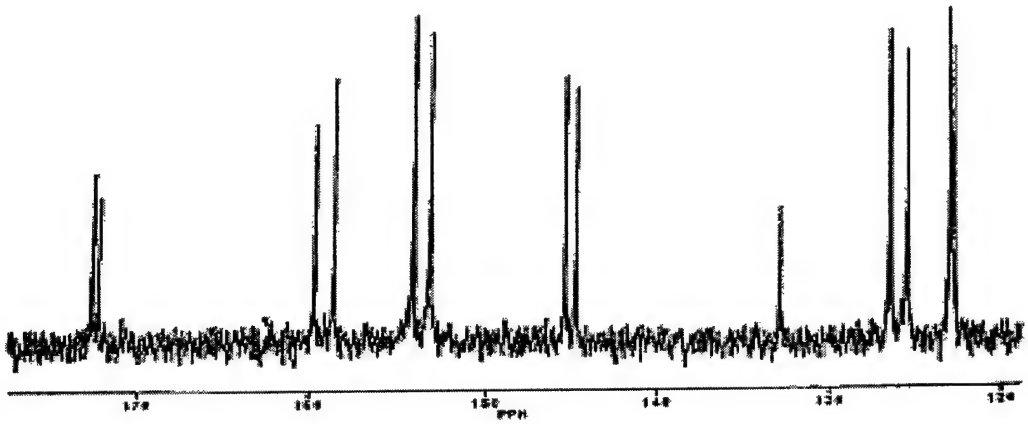

Figure 13. 13C NMR specrum of the (Bu4N)2[Ru(dcbpyH)2(NCS)2] complex in D2O + NaOD (0.1 M) at room temperature.

2.3.8. HPLC data. Identification of trace amounts of impurities and/or isomers by spectroscopic techniques is a difficult task. Therefore, HPLC was applied to separate the impurities prior to spectroscopic analysis. Application of a diode array detector allows the on-line measurement of the absorption spectra. Complexes N3, N719 and N712 were analyzed using reversed-phase chromatography that utilized adsorbent silica gel with a modified surface. The eluent is a polar one, acetonitrile/water mixture. The less polar a compound, the longer is the residence time on the stationary phase and therefore the retention time. A higher content of organic solvent in the eluent decreases the interaction and the retention time. To cover a wide spectrum of polarity, an increasing acetonitrile gradient was applied. A small amount of acid was added to the eluent to displace the dissociation equilibrium of the carboxylate groups to the protonated form. Figure 14, bottom trace, shows the chromatogram of complex N3, at a detection wavelength of 220 nm. The highest peak at 6.14 min belongs to the desired compound N3. Besides this main peak, there are two minor peaks, one at 5.7 min and another at 4.6 min. Interestingly the UV-vis spectra of peaks at 4.6 and 5.7 min are almost identical with that of the peak at 6.14 min. The fact that the absorption spectra are so close, coupled with the small difference in the retention time, is suggestive of the linkage isomers of the thiocyanate ligand. Figure 14, top trace, shows the HPLC

chromatogram of complex N719, where the retention time is the same as that of complex N3. The same retention time could be due to the fast exchange of tetrabutylammonium cations by the protons that are present in the mobile phase. The spectrum corresponding to the other small peak at 5.7 min is very similar to that of the main peak. The chromatographic peaks at about 1 min stem from the solvent front. It is interesting to note the presence of only one minor peak at 5.7 min in complex N719, whereas in complex N3 there are two minor peaks. This shows that, in the process of converting N3 to N719 complex one of the isomers was removed. We have collected the main peak by using a semi-preparative column, and when we re-injected the HPLC-purified sample solution, the chromatogram showed one single peak at the same retention time as the main peak for complex N3. Therefore, we exclude any possibilities of aggregation or decomposition during chromatography giving rise to additional small peaks. This shows that by transforming N3 complex into its tetrabutylammonium salts, we are effectively removing at least one linkage isomer. On the basis of the HPLC data, the minor peaks in complexes N3 and N719 are assigned to the linkage isomers of the NCS ligand. However, isolation of the thiocyanate isomer proved difficult because of the low yield of the reaction.

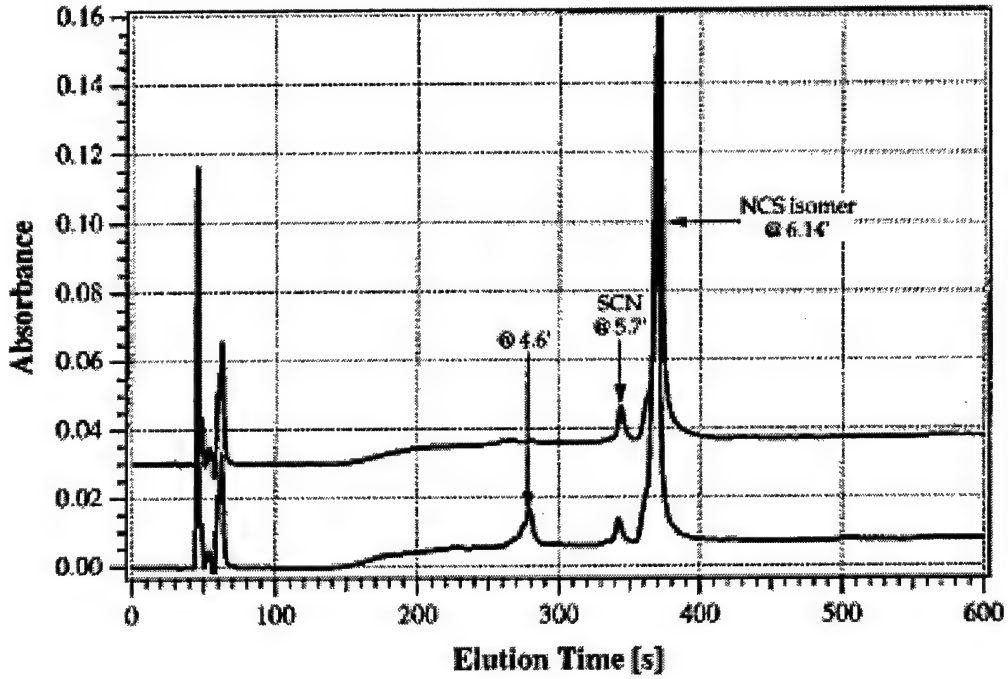

Figure 14. HPLC Chromatogram of the complexes N3 (bottom) and N719 (top).

2.3.9. Resonance Raman data. Laser excitation of of lowest energy MLCT band in N719 complex yields detailed resonance Raman spectra above 1000 cm-1, with bands characteristic of

the coordinated polypyridyl vibrations. Figure 15 shows the Raman spectrum of N719 complex obtained by excitation at 415.44 nm (Krypton laser as excitation source) which gave vibrational modes due to the 4,4'-dicarboxy-2,2'- bipyridine ligand at 1610, 1539, 1471, 1290, 1260, and 1102 ± 2 cm^{-1}. The broad and weak vibrational mode at 2105 ± 2 cm^{-1} is due to the coordinated NCS ligand. The intensity of this band is enhanced significantly compared to that of the solution spectrum.

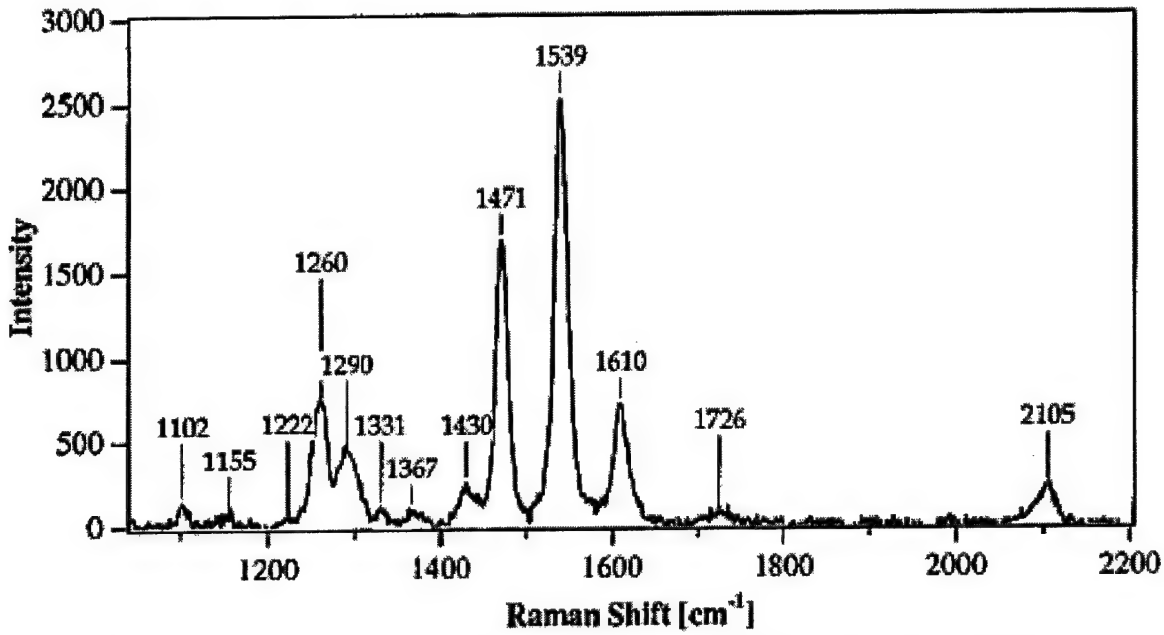

Figure 15. Resonance Raman spectra of N719 complex adsorbed on the TiO_2 surface.

2.3.10. FTIR studies

2.3.10.1. Photoacoustic FTIR spectra of $[Ru(dcbpyH_2)_2(NCS)_2]$ (N3), $(Bu_4N)_4[Ru(dcbpy)_2(NCS)_2]$ (719) , and $(Bu_4N)_4[Ru(dcbpy)_2(NCS)_2]$ (712).

The molecular structures of the N3, 719 and 712 complexes are shown in scheme 1. They differ in the number of protons four, two and zero, respectively. A comparison of FTIR spectra obtained in Photoacoustic (PAS) mode using solid samples of N3, 719 and 712 are shown in Figure 16. The FTIR spectrum of the N3 complex (Figure 16a) show the characteristic band at 2123 cm^{-1} due to υ(NCS) group. The two distinct bands at 1740 and 1708 cm^{-1} are assigned tentatively to the C=O stretching of the cis- (carboxylic groups trans to the NCS ligands) and the trans carboxylic groups (carboxylic groups trans to pyridine). The apparent difference between cis- and trans- carboxylic acid groups in the N3 complex is consistent with its ground state pKa's,

which are found to occur in two steps at 3 (pK_{a1}) and 1.5 (pK_{a2}). These values are assigned to concurrent dissociation of two protons coming from the cis- and trans carboxylic acid groups, respectively. The IR data are also in agreement with ^{13}C NMR spectra discussed in the NMR section. The FTIR, the pK_a and the ^{13}C NMR data unambiguously show that the difference in the cis- and the trans-carboxylic acid groups of the N3 complex is measurable by various spectroscopic techniques. The two peaks at 1273 and 1242 cm^{-1} are assigned to υ(C-O) stretch. The sharp and slightly weaker bands at 1617, 1551 and 1421 cm^{-1} are assigned to the bipyridyl υ(C=C) absorption.

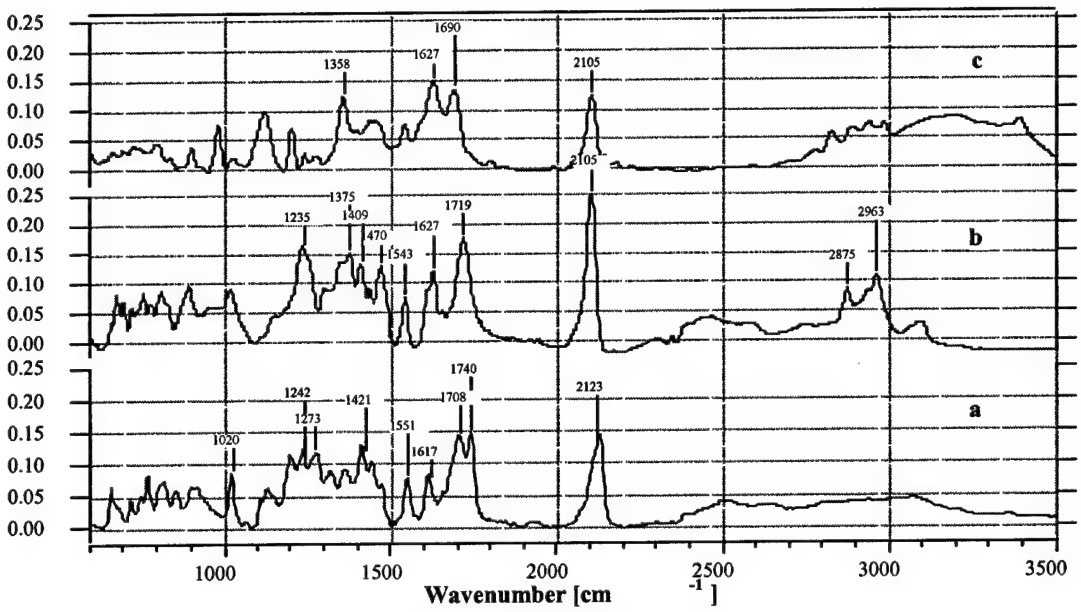

Figure 16. FTIR spectra of N3 (a), N719 (b) and N712 (c) obtained in photoacoustic mode using solid samples.

The photoacoustic FTIR spectrum of the N719 complex (Figure 16b) show presence of carboxylic acid and the carboxylate groups. The bands at 1719 and 1235 cm^{-1} are assigned to the υ(C=O) and υ(C-O) groups, respectively. The other two strong bands at 1627 ($-COO^-_{as}$) and 1375 ($-COO^-_s$) cm^{-1} are assigned to the asymmetric and the symmetric stretch of the carboxylate group, respectively. The bands at 1627, 1543 and 1409 cm^{-1} is assigned to the bipyridyl absorption. The band at 1470 cm^{-1} is assigned to the $\delta(CH_2)$ of the Bu_4N^+ cations.[31] The N712 complex (Figure 16c) show the presence of carboxylate groups at 1690 and 1627 due to the

asymmetric stretch of the cis and the trans carboxlate groups ($-COO^-_{as}$). The corresponding symmetric stretch ($-COO^-_s$) was observed at 1358 cm^{-1}. The bands at 2858, 2931, 2873 and 2960 cm^{-1} in N719 and N712 are assigned to υ(C-H) of tetrabutylammonium symmetric and asymmetric $-CH_2$ and $-CH_3$ groups, respectively.[31] The □(NC) band in N719 and N712 was observed at 2105 cm^{-1}, which is shifted to lower energy compared to the NCS band in the N3 complex (2123 cm^{-1}).

2.3.10.2. Surface chelation of polypyridyl complexes onto the TiO_2 oxide surface.

The carboxylate functional groups of the dye serve as grafting agents for the oxide surface of the TiO_2 films. The grafting of polypyridyl complexes onto the oxide surface, which allows for electronic communication between the complex and the substrate, is an important feature in dye-sensitized solar cell. To achieve high quantum yields of the excited state electron transfer process the dye ideally needs to be in intimate contact with the semiconductor surface. The ruthenium complexes that have carboxylic acid and phosphonic acid groups show electron transfer yields in the range of 80 to 100%. The near quantitative electron injection efficiency indicate a close overlap of the ligand π* orbitals and the titanium 3d orbitals.

The ATR-FTIR spectra of the N3, 719 and 712 complexes measured as a solid and in the adsorbed form onto TiO_2 films are shown in Figures 17 and 18, respectively. The N3 solid sample shows a strong broad band at 1720 cm^{-1} due to carboxylic acid groups (Figure 17a). It is interesting to note the presence of only one band in the carboxylic acid position compared to the PAS IR spectra where two bands were observed due to cis- and trans-carboxylic acid groups. However, the bandwidth of the carboxylic acid groups in ATR spectra (60 cm^{-1}) is larger than the difference between the cis- and the trans- carboxylic groups (40 cm^{-1}). The intense peak at 1229 cm^{-1} is assigned to υ(C-O) stretch.

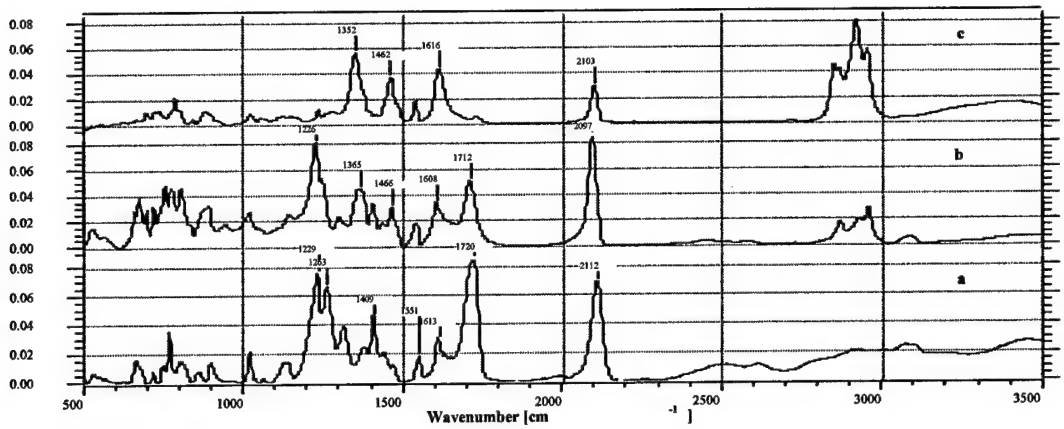

Figure 17. ATR-FTIR spectra of N3 (a), N719 (b) and N712 (c) obtained using solid samples.

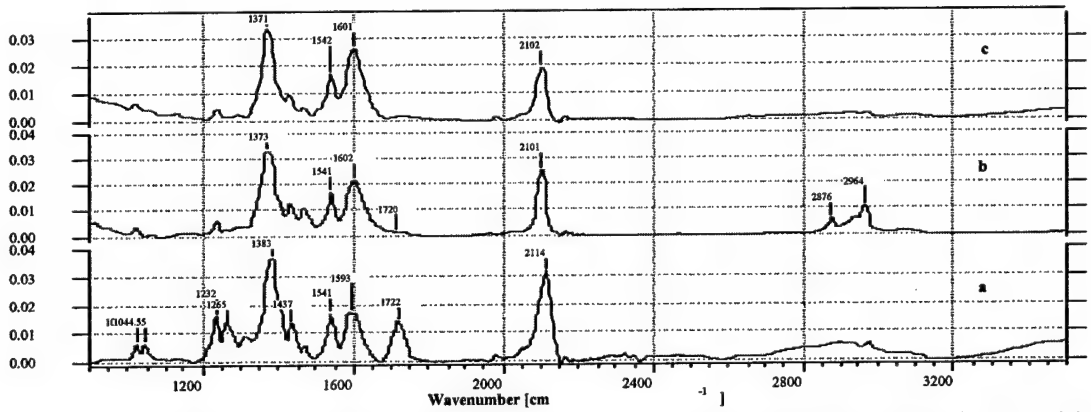

Figure 18. ATR-FTIR spectra of the TiO_2 films adsorbed by N3 (a), N719 (b) and N712 (c) dyes.

The N719 complex that contains two carboxylic acid and two carboxylate groups shows bands at 1712 and 1608 cm^{-1} due to υ(-C=O) and υ($-COO^-_{as}$), respectively. The symmetric stretch of carboxylate group was observed at 1365 cm^{-1}. The intense peak at 1226 cm^{-1} is assigned to υ(C-O) stretch (Figure 17b). The FTIR spectra of the N712 complex show bands due to carboxylate groups asymmetric and symmetric at 1616 cm^{-1} ($-COO^-_{as}$), and 1352 cm^{-1} ($-COO^-_s$), respectively (Figure 17c). The significant difference between PAS mode and the ATR mode is the bandwidth, which is smaller and sharp (30 cm^{-1}) in the former case compared to the ATR mode. The banddue tọυ(NC) of the thiocyanate ligand was observed at 2112, 2097 and 2103 cm^{-1} in N3, 719 and 712 complexes, respectively. It is interesting to compare the intensity of the NCS peak in the N3, N719 and N712 complexes where in the later case it is lower than the former two complexes, which is due to differences in the dipole movement. The protons in both the

complexes N3 and N719 are located trans to the NCS groups, which induces a larger dipole compared to the NCS groups in N712.

Figure 18 (a) shows ATR-FTIR spectrum of the N3 adsorbed on TiO_2. The major difference between the solid and the adsorbed N3 spectra is the presence of carboxylate asymmetric 1593 cm^{-1} $\upsilon(-COO^-_{as})$ and symmetric 1383 cm^{-1} $\upsilon(-COO^-_{s})$ bands together with carboxylic acid group at 1722 cm^{-1}. The presence of carboxylic acid and carboxylate groups in the IR spectra of adsorbed N3 on TiO_2 testify that all the carboxylic acid groups are not dissociated or involved in the adsorption on the TiO_2 surface. On the other hand the complex N712 (Figure 18c) shows the presence of only carboxylate groups at 1601 $\upsilon(-COO^-_{as})$ and 1371 cm^{-1} $\upsilon(-COO^-_{s})$ confirming the absence of ester bond between the complex and the TiO_2.

In the N3 and the N712, there are four anchoring groups. Because of steric reasons anchoring of these complexes onto the TiO_2 surface using all the groups is not possible. However, the question arises as to how many groups are adsorbed on the surface and what is the anchoring mode? A comparison of the normalized intensities of the carboxylate group in the free and the adsorbed dyes with the bpy band at 1544 cm^{-1} indicate two carboxylate groups are involved in the anchoring of the dye onto the TiO_2 surface.

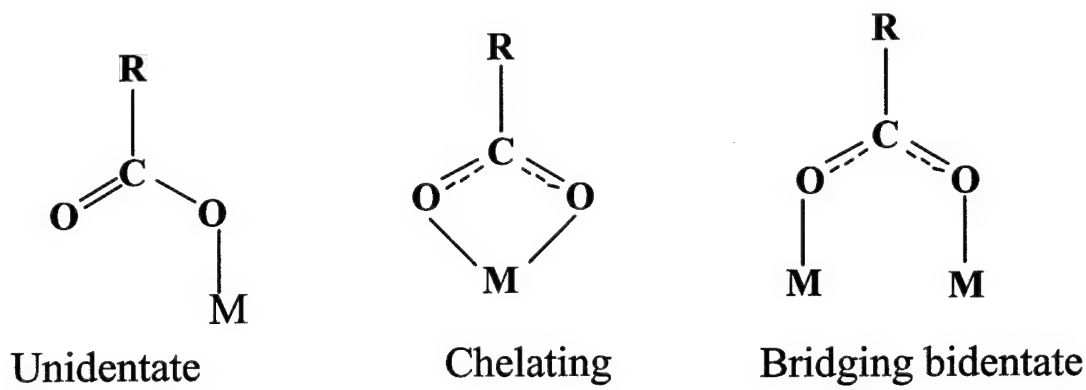

Scheme-3

A carboxylate group can coordinate to the TiO_2 surface in number of ways: as a unidentate mode, as a chelating mode and as a bridging bidentate mode shown in scheme 3. The unidentate coordination of the carboxylate group removes the equivalence of the two oxygen atoms resulting to an ester type of bond formation between the carboxylic acid group and the TiO_2 surface. Based on the IR data of adsorbed N712 complex this type of coordination can be ruled out, leaving only two possiblities, chelation and/or bridging type of coordination. However,

for identifying carboxylate-anchoring mode, based on metal acetate complexes several groups have used the difference between the asymmetric and symmetric bands in the free and the adsorbed state as criteria. Where, if the difference between the carboxylate group asymmetric and symmetric bands in the adsorbed state is lower than the free state then the anchoring mode is either bidentate chelation or bridging. If the difference is greater or equal to the free state then anchoring mode is unidentate.[32]

The separation between the carboxylate group asymmetric and symmetric bands of N712 in the free (264 cm^{-1}) and the adsorbed state (230 cm^{-1}) suggest that this dye anchor either as bidentate chelation or as bridging coordination to the TiO_2. The separation in the N3 and the N719 complexes between the carboxylate group asymmetric and symmetric bands in the adsorbed state is 211 and 227 cm^{-1} consistent with bidentate chelation or bridging coordination mode. However, recent theoretical studies on the interaction of formic acid and sodium formate on anatase (101) surface showed that the formation of bidentate chelation mode is highly unstable leaving the possibility of bridging coordination mode.[33] Anchoring of the dye onto the TiO_2 surface using bidentate chelation mode of the carboxylate group should result in enhanced stability for the sensitizer compared to the unidentate adsorption. Our findings are in excellent agreement with photoelectron spectroscopic data of N3 adsorption on TiO_2.[34]

The ATR-FTIR data of the N3 and the N712 complexes show that these dyes anchor onto the TiO_2 surface using two of its four carboxylic acid groups as a bridging coordination mode. Nonetheless, out of four anchoring groups which of the two i.e. cis-, trans-, or mixed carboxylic acid groups remained unsolved? The N719 complex that contains two carboxylic groups, which are trans to the NCS ligands and two carboxylate groups, which are trans to each other. When the complex N719 is adsorbed on the surface, it could adsorb using the carboxylic or carboxylate or both carboxylic and carboxylate groups. The FTIR spectra show (Figure 18b) the presence of mainly carboxylate groups demonstrating that the complex is being adsorbed on the surface using the two carboxylic groups, which are trans to the NCS ligands.

2.3.11. Thermal behavior of the dyes

2.3.11. 1. Thermal behavior of the free dyes. Thermal stability of ruthenium (II) N3, N719 and N712 complexes has been studied using thermoanalytical techniques. The combined TG, DTG, and DSC curves of N3 in dynamic atmosphere of air and nitrogen are presented in Figures 19 and 20, respectively. In air, three well-defined steps can be observed in the TG and DTG curves (Fig.

19). The first step between 35-100 °C, is associated with 8.14% mass loss which is attributed to the endothermic dehydration of the dye loosing 3.52 moles of water (-3.5H_2O = 8.11%). The elemental analysis of the complex N3 shows the presence of 3.5 water molecules per ruthenium center, which is consistent with TGA analysis. The dye is stable up to about 250 °C and does not undergo any changes detectable by TG and DSC. Further evidence for the stability of the dye comes from the IR and ^{1}H NMR studies. The IR and ^{1}H NMR spectra of the sample were essentially unchanged, when a sample of N3 was heated up to 150 °C in air atmosphere and kept under these conditions for 1h. The coordinated NCS ligand remains intact and shows an intense band at 2107 cm^{-1} due to thiocyanate ν(CN) in the IR spectrum and the ^{1}H NMR spectrum shows peaks at the positions identical to the unheated complex.

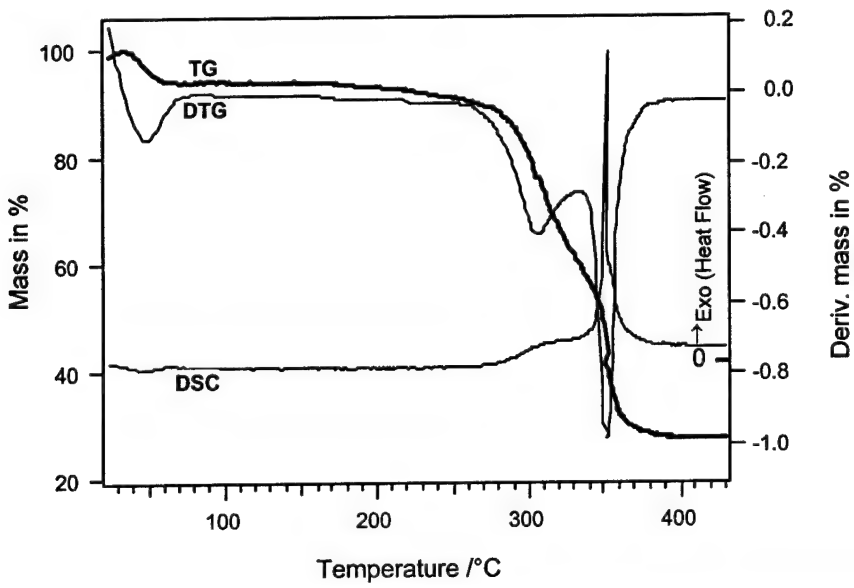

Figure 19. TG, DTG, and DSC curves of N3 in a dynamic air atmosphere (20ml/min).

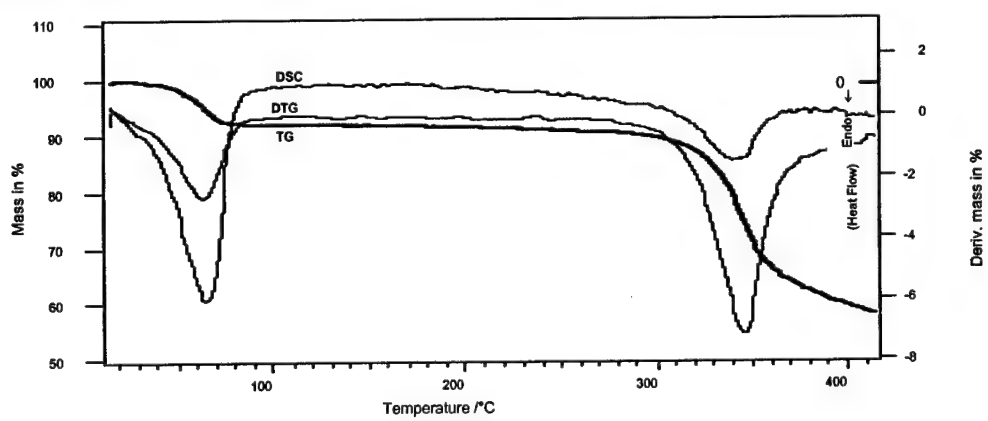

Figure 20. TG, DTG, and DSC curves of **N3** in a dynamic nitrogen atmosphere (20ml/min).

Figure 20 shows that decarboxylation of the complex N3 under N_2 takes place at a higher temperature (T_i = 290 °C) compared to air, and overlaps with decomposition. These two processes occur concurrently as a single endothermic step. In air however, the decarboxylation reaction begins at 250 °C and proceeds as a well-defined exothermic process which is clearly separated from the decomposition process. The mass loss in this step is 23.67% (-4CO_2 = 22.65%) and during this process four carboxylate groups on the two bipyridine ligands are oxidized into carbon dioxide.[35]

The TG, DTG, and DSC curves of N719 in dynamic air and nitrogen atmospheres are shown in Figure 21 and 22, respectively. The major difference between thermal behavior of the dyes with organic cations N719 and N3 is the additional de-amination process. Similar to N3, the first step, between 35 to 90 °C, is accompanied by 2.23% mass loss (- 1.5 H_2O = 2.23%) which is attributed to the dehydration process. The dye is stable up to 190 °C showing no changes detectable by TG and DSC. The IR and ^1H NMR spectra of a sample of N719 heated up to 150°C under nitrogen for 1h is essentially unchanged. In the second step, between 190 and 295°C, tetrabutylammonium undergoes decomposition resulting in gaseous products. Thermal properties of tetraalkyl ammonium salts have been studied and it is well established that tertiary amines are one of the thermal decomposition products formed at elevated temperatures. It is clear that in a dynamic atmosphere, most of the resulting amine escapes from the reaction chamber, however the possibility of secondary reactions for the trapped amine molecules cannot be ruled out. These reactions accompanied by the decomposition of the organic ligands in air atmosphere might well account for the three exothermic processes following the decarboxylation reaction which occurs in the third step between 295 and 345 °C. The mass loss in the second step is 33.63%, which correlates with the release of 1.69 moles of tetrabutylammonium (-2Bu_4N^+ =39.77 %). This is a reasonable value considering the overlap between deamination and decarboxylation processes in steps 2 and 3. The mass loss in the third step is 18.99 % which corresponds to the release of 5.2 CO_2 molecules (-4CO_2 = 14.52%). A comparison between the theoretical and experimental values of the total mass loss for the release of 4 (CO_2 + Bu_4N^+) in these two successive steps, which are 54.29% and 52.61% respectively, indicates that a combination of these two processes can reasonably well account for the experimental results. In a nitrogen atmosphere, however, the decarboxylation and decomposition processes occur in a single endothermic step in a manner similar to N3.

An interesting observation in the thermal behavior of N719 is that the decarboxylation and decomposition reactions take place at higher temperatures relative to N3. While in a dynamic air atmosphere, decarboxylation begins at T_i = 250 °C for N3 (with the temperature for the maximum rate T_m = 308 °C) the corresponding temperatures for N719 are T_i = 295 °C and T_m = 315 °C. The decomposition process also takes place at higher temperature in N719, T_i = 340°C and T_m = 360 °C compared to N3. This additional stability towards decarboxylation and decomposition, which is also observed in N712, could be due to softer interaction between the bulky organic cations with carboxylate groups.

Figure 23 and 24 show TG, DTG, and DSC of N712 in dynamic air and nitrogen atmospheres, respectively. The thermal processes are similar to those observed for N719 except for the higher water content of N712 due to its more hygroscopic character relative to N719, and a two step deamination process with a higher ratio, $4Bu_4N$ vs. $2Bu_4N$. The interesting feature of the deamination of N712 is the decomposition of four Bu_4N groups in two successive steps with T_{m1} = 210 °C and T_{m2} = 235 °C. The pK_a of the carboxylate groups of N3 have been measured and it is clear that the two carboxylate groups located trans to NCS ligands are more basic than the ones trans to each other.[23] The observed two step deamination process for N712 can be rationalized on the basis of the difference in the extent of interaction between the two types of carboxylate anions with Bu_4N^+ cations.

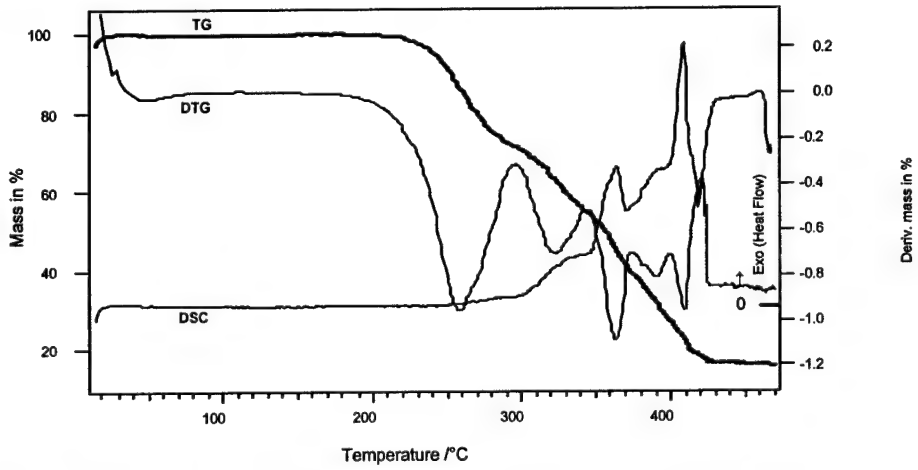

Figure 21. TG, DTG, and DSC curves of N719 in a dynamic air atmosphere (20ml/min).

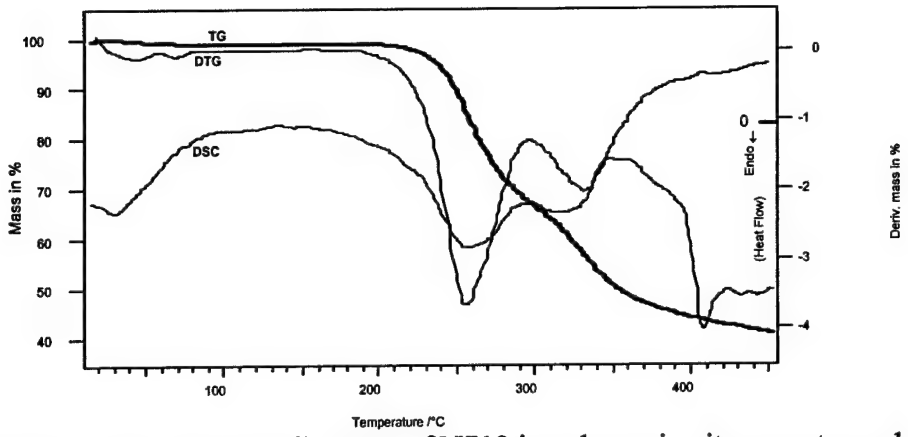

Figure 22. TG, DTG, and DSC curves of N719 in a dynamic nitrogen atmosphere (20ml/min).

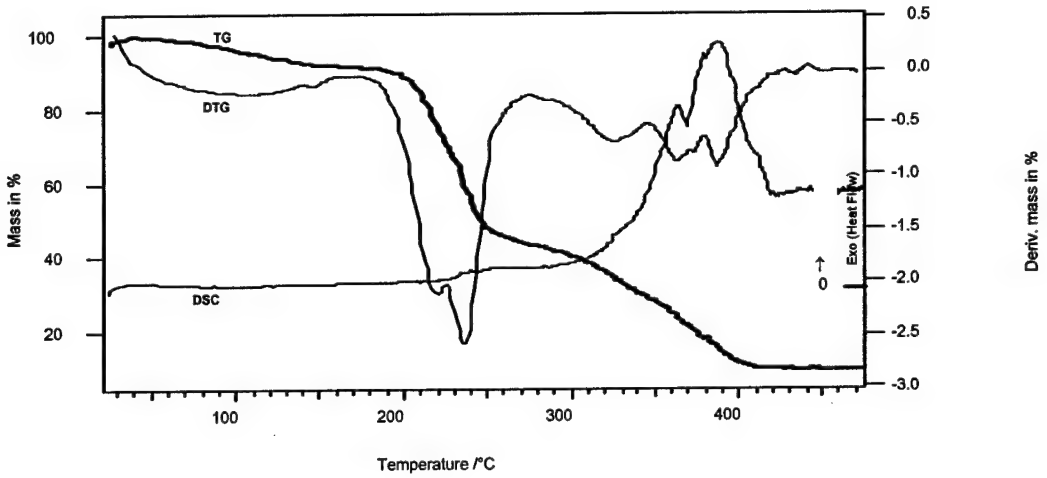

Figure 23. TG, DTG, and DSC curve of N712 in a dynamic air atmosphere (20ml/min).

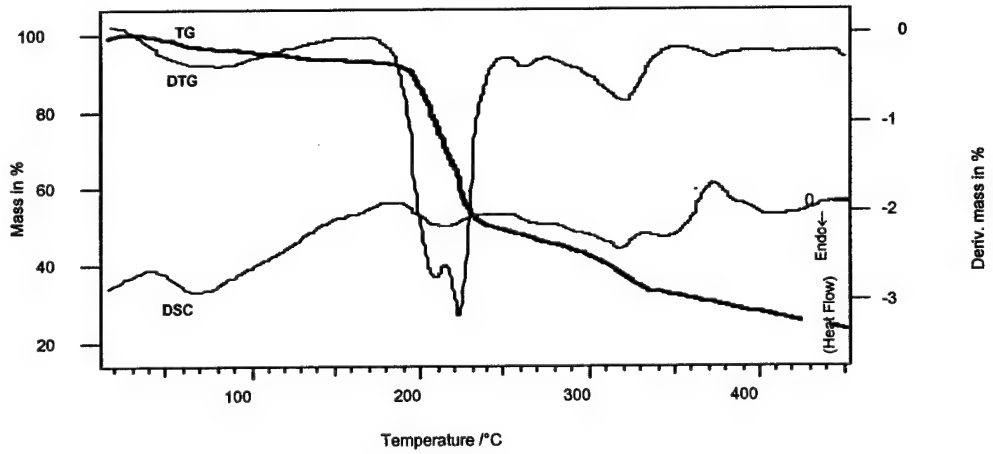

Figure 24. TG, DTG, and DSC curve of N712 in a dynamic nitrogen atmosphere (20ml/min).

2.3.11.2. Thermal behavior of the dyes on TiO_2

One of the interesting features of the thermal behavior of the dyes is their additional thermal stability when anchored onto TiO_2 in comparison with their free form. As in the free dye, the first step between 40 to about 100 °C belongs to the dehydration process. In this step the water from the mesopores of TiO_2, which is mostly adsorbed from the environment, is released. The decarboxylation process, however, begins at a higher temperature relative to the free dye. The initial temperatures (T_i) for decarboxylation and decomposition processes of N3 in the free form are 250 °C and 335 °C, respectively. These two processes begin to occur at 320 °C and 370 °C when N3 is anchored onto TiO_2.

A similar trend is observed for N719 on TiO_2 with T_i values of 340 °C and 378°C as compared to 295 °C and 340 °C for decarboxylation and decomposition processes of the free dye. The remarkable increase of about 60°C in the thermal stability of the dyes against decarboxylation and about 40 °C against decomposition can be rationalized in terms of the strong interaction between the carboxylate groups and TiO_2. An higher activation energy is also expected for the decarboxylation of the dye on TiO_2 relative to the free dye. In order to estimate the activation energy of the decarboxylation of N3, the temperature (T_m) at maximum weight loss (TG) in the decarboxylation process was determined as a function of heating rate (θ) applied from the thermoanalytical curves. The activation energy was directly estimated from the slope of the graph Log θ against $1/T_m$. The estimated value of E_a=126 kJ mol^{-1} for the decarboxylation of dye N3 on TiO_2 as compared to 115 kJ mol^{-1} for the free dye is consistent with the observed higher thermal stability of the dye anchored onto TiO_2.

It is evident from the thermoanalytical data obtained for N719 that the deamination process is slow and takes place within a large temperature range. In addition, the approximate weight loss in this process correlates well with the presence of about one Bu_4N^+ as a counterion with the dye on TiO_2. The ^1H NMR spectrum of the desorbed complex N719 from the TiO_2 surface gives an additional support for the presence of one Bu_4N^+. Therefore, it is most likely that the strong interaction between TiO_2 and the negatively charged carboxylate groups can account for the charge compensation by hydroxide loss from the TiO_2 surface as well as for the additional stability of the dye toward decarboxylation.

2.3.12. Photovoltaic performance.

2.3.12.1. Influence of protons on power conversion efficiency of the cell. The performance of

N3 sensitizer and its various protonated forms on nanocrystalline TiO_2 electrodes have been studied and the data are collected in Table 3. Figure 25 shows the current-voltage characteristics obtained with a sandwich cell under illumination by simulated AM 1.5 solar light. The incident monochromatic photon-to-current conversion efficiency (IPCE) is plotted as a function of excitation wavelength show in the plateau region 90% for N3 complex while for N712 complex it is only about 70%. In the red region, the difference is even more pronounced. Thus, at 700 nm the IPCE value is twice as high for the N3 complex as compared to the N712 complex. Consequently the short circuit photocurrent is 19 ± 1 mA/cm^2 for N3 complex, while it is only about 13 ± 1 mA/cm^2 for N712 complex. However, it is impressive that the photovoltage for N712 is 900 mV, which is 300 mV higher than the N3 (see figure 25). The increased open-circuit potential in the former case is the result of negative shift of the Fermi level that increases the gap between the redox couple iodide/triiodide and the Fermi level. The photovoltaic performance of N719 complex that carries two protons shows 17 ± 1 mA current and 730 mV potential. The fill factor also increases with increasing open circuit potential of the dye-sensitized solar cell. The data presented in Table 3 suggest that the one proton dye is the optimum for high power conversion efficiency of the cell.

The decrease in the IPCE of the N712 compared to the N3 is due the influence of protons on the energetics of the TiO_2 conduction band and therefore on the energetics of electron injection. The second possible reason could be slow regeneration of the dye by the redox couple because of decreased driving force between the dye and the redox couple. Recently, Tachibana et al. reported electron injection kinetics for nanocrystalline TiO_2 electrodes sensitized with the N3 and the N719 dyes.[36] In their studies, they found that the electron injection kinetics for N719 dye is retarded 30-fold compared to the N3 dye. Their data imply that the low IPCE in the N712 complex compared to the N3 dye is due to the energetics of the TiO_2 conduction band rather than the decrease in the driving force between the sensitizer and the redox couple.

2.3.12.2. Effect of LH-20 column Purification on photovoltaic efficiency. The N719 complex was purified on a Sephadex LH-20 column three times. Elemental analysis data of the N719 complex purified once, twice and three times are the same. However, there are differences in the NMR spectroscopic and the photovoltaic data of these samples. The total efficiency of dye-sensitized solar cell increased with increased number of purifications up to three times. Figure 26 shows a comparison of efficiency with one, two and three times purified N719 dye on a

Sephadex LH-20 column. Figure 27 shows the best efficient cell (10.58%) measured with 3 times LH-20 purified sample using an electrolyte that contains guanidinium thiocyanate, 30 mm I_2, 0.6 M of N-butyl-N'-methylimidazolium iodide, 0.5 M tert-butyl pyridine in 84% acetonitrile, 15% valeronitrile and 1% water.

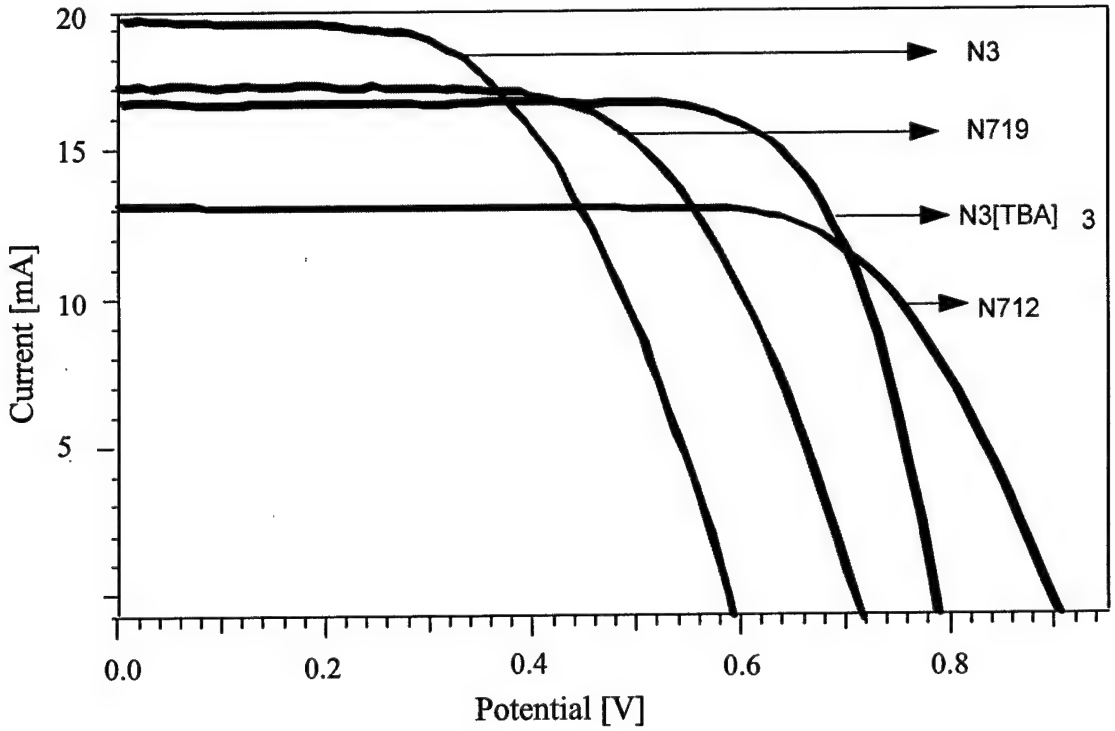

Figure 25. Photocurrent-voltage characteristics of nanocrystalline TiO_2 cell sensitized with N3 (contains 4 protons), N719 (contains 2 protons), N3[TBA]$_3$ (contains 1 proton) and N712 (contains zero proton) dyes measured under AM 1.5 sun using 1cm^2 size of TiO_2 electrodes with I^-/I_3^- redox couple in methoxyacetonitrile (N3 = [Ru(dcbpyH$_2$)$_2$(NCS)$_2$], N719 = (Bu$_4$N)$_2$[Ru(dcbpyH)$_2$(NCS)$_2$], N3[TBA]$_3$ = (Bu$_4$N)$_3$[Ru(dcbpyH)(dcbpy)(NCS)$_2$] and N712 = (Bu$_4$N)$_4$[Ru(dcbpy)$_2$(NCS)$_2$]).

Sensitizer	Number of protons	Solvent for dye adsorption	Current mA/cm^2	Potential (mV)	Fill Factor	Efficiency at 1.5 AM
N3	4	1:1 CH_3CN+ *tert*-BuOH	19 ± 0.5	600 ± 30	0.65 ± 0.05	7.4
N719	2	1:1 CH_3CN+ *tert*-BuOH	17 ± 0.5	730 ± 30	0.68 ± 0.05	8.4
N712	0	C_2H_5OH	13 ± 0.5	900 ± 30	0.7 ± 0.05	8.2
$N3[TBA]_3$	1	5:95 CH_3CN +*tert*-BuOH	17±0.5	770 ±20	0.73±0.05	9.56
N3[TBA]	3	1:1 CH_3CN+ *tert*-BuOH	17 ± 0.5	700 ± 20	0.65 ±0.05	7.7

Table 3. Performance Characteristics of Photovoltaic cells based on Nanocrystalline TiO_2 films sensitized by N3 with different degrees of protons.

Fogure 26. Effect of LH-20 purification on the efficiency of dye-sensitized solar cell under AM 1.5 sun

Cell Name: PL0705/bb1_May 12#32

Measurement Date	: Mon, May 12, 2003 / 11:14:29 PM
Type of cell	: PC; tipex + AR
Cell Active Area	: 0.158 cm^2
Light Source	: Xe 450W @ AM1.5G
Dye Sensitiser	: N719
Additional Remarks	: 111.. old rec.; 24h
Electrolyte 1316	: 1376 mod.0.1M GRh; 85% ACN..
Working Temperature	: 298 K
SemiConductor Layer	: 16/4+ TiCl4>; 20nm; + AR
Layer Thickness, Porosity	: 12 µm, 0.68 %
Working Electrode Glass	: LOF 15ž/cm
Counter Electrode Type	: LOF 15ž/Pt°/Ag
Data File Name	: PL0705/bb1_May 12#32
Current Compliance	: 2 mA
Settling Time, Voltage Step	: 0.1 s, 10 mV0 s

	9.4% Sun	55.3% Sun	99.8% Sun
Thermopile $_{ref}$	Nan Sun	Nan Sun	Nan Sun
Current $_{ref}$	-364.346 µA	-2.136 mA	-3.851 mA
Power $_{in}$	9.439 mW/cm^2	55.331 mW/cm^2	99.762 mW/cm^2
Norm. Std. Dev.	0.19	0.33	0.27
Module U_{oc}	722.52 mV	778.56 mV	795.65 mV
Cell U_{oc}	722.52 mV	778.56 mV	795.65 mV
I_{sc}	-269.369 µA	-1.563 mA	-2.801 mA
J_{sc}^{norm}	-1.72 mA/cm^2	-11.45 mA/cm^2	-17.77 mA/cm^2
U_{pmax}	594.88 mV	632.06 mV	629.87 mV
I_{pmax}	-1.6 mA/cm^2	-9.4 mA/cm^2	-16.8 mA/cm^2
Power $_{out}$	972.19 µW/cm^2	5.94 mW/cm^2	10.55 mW/cm^2
Total Power $_{out}$	153.61 µW	938.16 µW	1.67 mW
Fill Factor	0.789	0.771	0.748
Efficiency η	10.30%	10.73%	10.58%

IPCE @ 550 nm : 160.11 %
Slope ŽV$_{oc}$/Žln(I $_o$) : 31.172 mV
Ideality Factor @ 1 Sun : 1.73
Series Resistance @ 1 Sun: 14.69 ž ± 0.96 %, (2.32 ž/cm2)

Calibration File: Solar Lab I:Igor Applications:DataScan Data:cal_Thu, Oct 11, 2001

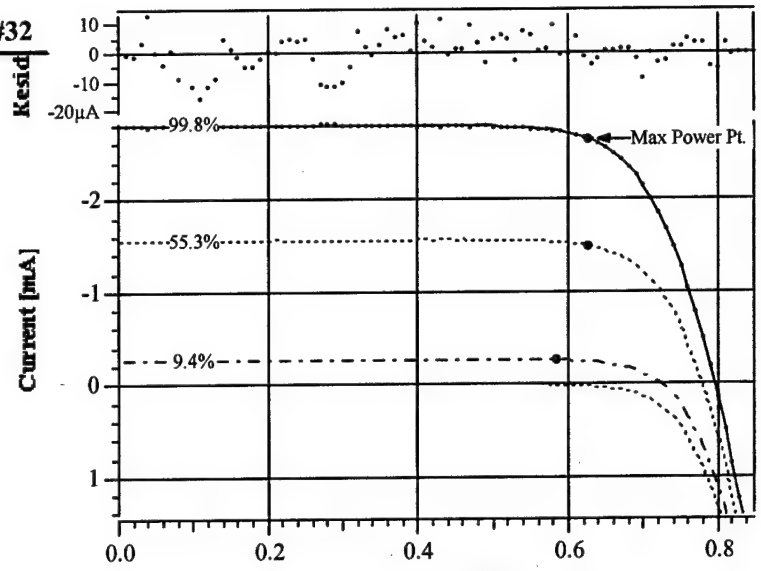

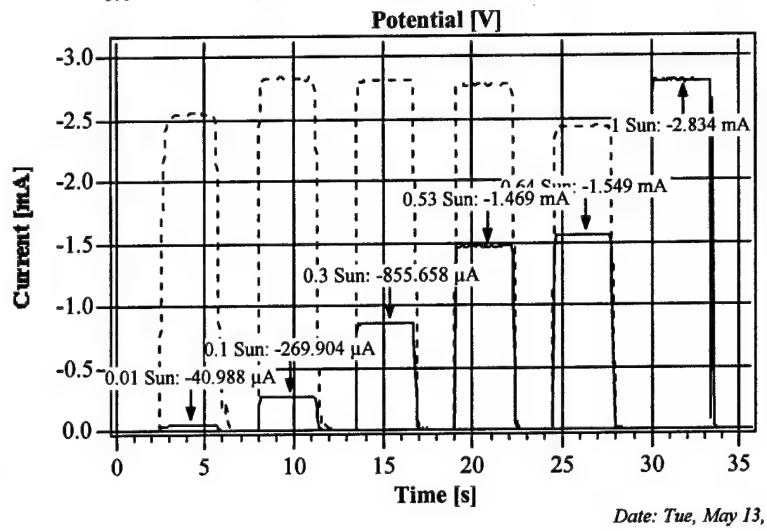

© RAHB: KIDAQ *Measured by Paul* *Date: Tue, May 13, 20*

Figure 27. Photocurrent–voltage curve of a solar cell based on an electrolyte containing guanidinium thiocyanate as self-assembly facilitating agent. The cell was equipped with an antireflecting coating. The conversion efficiency in full sunlight was 10.58%.

3. Hydrophobic Sensitizers

The pioneering studies on dye sensitized solar cells using *cis*-dithiocyanatobis(4,4'-dicarboxylic acid-2,2'-bipyridine)Ruthenium(II), (N3) is a paradigm in this field. A new development for dyes applied to solar cell comes from amphiphilic heteroleptic N3-equivalents.[37] These amphiphilic heteroleptic sensitizers have several advantages compared to the N3 complex: (a) The ground state pK_a of the 4,4'dicarboxy-2,2'-bpy is higher so that enhances the binding of the complex onto the TiO_2 surface. (b) The decreased charge on the sensitizer attenuates the electrostatic repulsion and there by increasing the dye loading. (c) The presence of hydrophobic moiety on the ligand increases the stability of solar cells towards water induced desorption. (d) The oxidation potential of these complexes is cathodically shifted compared to the N3 sensitizer, which increases the reversibility of ruthenium III/II couple leading to enhanced stability. In this section we describe detailed synthesis, characterization and photovoltaic data of this novel class of compounds

3.1. Synthesis

3.1.1. Materials: The solvents (puriss grade, from Fluka), hydrated ruthenium trichloride (from Johnson Matthey), 4,4'-dimethyl-2,2'-bipyridine (dmbpy), 4,4'-dinonyl-2,2'-bipyridine (dnbpy), dichloro(p-cymene)ruthenium(II) dimer and potassium/ammonium thiocyanate were obtained (from Aldrich) and used as received. 4,4'-dihexyl-2,2'-bipyridine and 4,4'-ditridecyl-2,2'-bipyridine were synthesized using literature procedures.[37, 38]

3.1.2. Synthesis of $[Ru(H_2dcbpy)(dmbpy)(NCS)_2]$ N820 (H_2dcbpy = 4,4'-dicarboxy-2,2'-bipyridine, dmbpy = 4,4'-dimethyl-2,2'-bipyridine)

In a typical synthesis, $[RuCl_2(p\text{-cymene})]_2$ (0.1 g, 0.16 mmol) was dissolved in DMF (50 ml) to which was added 4,4'-dimethyl-2,2'-bipyridine (0. 0.058 g., 0.32 mmol) as a solid. The reaction mixture was heated to 55-65 °C under nitrogen for 4 h with constant stirring. After this period H_2dcbpy (0.08 g., 0.32 mmol) was added as a solid and refluxed at 155-165 °C for 4 h. Then, excess of NH_4NCS (0.76 g., 10 mmol) was added to the reaction mixture and continued refluxing for another 5 h at 140-150 °C. The reaction flask was allowed to cool to 25 °C. and the solution was filtered through a G4 sintered glass crucible. The solvent was removed by using a rotary-evaporator under vacuum. The resulting solid was washed with water to remove excess of NH_4NCS and the insoluble product was collected on a sintered glass crucible by suction

filtration. The solid was further washed with distilled water and diethyl ether. The crude complex was purified on a Sephadex LH-20 column using methanol as an eluent.

^{1}H NMR (δ_H/ppm in CD_3OD) 9.66 (d, 1H), 9.27 (d, 1H), 9.05 (s, 1H), 8.90 (s, 1H), 8.5 (s, 1H), 8.34 (s, 1H), 8.32 (d, 1H), 7.88 (d, 1H), 7.70 (d, 2H), 7.65 (d, 1H), 7.37 (d, 1H) 7.05 (d, 1H), 2.91 (s, 3H), 2.45 (s, 3H).

Analysis found C, 47.23% ; H, 3.33%; N, 12.59%. Calculated C, 47.05%; H, 3.34%; N, 12.66% for $C_{26}H_{20}N_6O_4.Ru.S_2\ H_2O$

3.1.3. Synthesis of [Ru(H_2dcbpy)(dhbpy)(NCS)$_2$] N823 (H_2dcbpy = 4,4'-dicarboxy-2,2'-bipyridine, dhbpy = 4,4'-dihexyl-2,2'-bipyridine)

Using the same conditions as for complex N820, starting from ligand 4,4'-dihexyl-2,2'-bipyridine the title compound was obtained as a dark powder. Yield 65%.

^{1}H NMR (δ_H/ppm in CD_3OD) 9.66 (d, 1H), 9.26 (d, 1H), 9.02 (s, 1H), 8.87 (s, 1H), 8.51 (s, 1H), 8.37 (s, 1H), 8.18 (d, 1H), 7.85 (d, 1H), 7.67 (d, 2H), 7.61 (d, 1H), 7.39 (d, 1H) 7.05, 3.15 (t), 2.7(t), 1.95 (m), 1.57 (m), 1.0 (t).

Analysis found: C, 54.90%; H, 5.17%; N, 10.61%. Calculated C, 55.01%; H, 5.13%; N, 10.6% for $RuC_{36}H_{40}N_6O_4S_2$.

3.1.4. Synthesis of [Ru(H_2dcbpy)(dnbpy)(NCS)$_2$] Z907 (H_2dcbpy = 4,4'-dicarboxy-2,2'-bipyridine, dnbpy = 4,4'-dinonyl-2,2'-bipyridine)

Using the same conditions as for complex N820, starting from ligand 4,4'-dinonyl-2,2'-bipyridine the title compound was obtained as a dark powder. Yield 60%.

^{1}H NMR (δ_H/ppm in CD_3OD) 9.72 (d, 1H), 9.28 (d, 1H), 9.08 (s, 1H), 8.92 (s, 1H), 8.55 (s, 1H), 8.42 (s, 1H), 8.28 (d, 1H), 7.88 (d, 1H), 7.70 (t, 2H), 7.40 (d, 1H), 7.05 (d, 1H), 2.95 (t, 2H), 2.75(t, 2H), 1.95 (m, 2H), 1.40 (m, 26H), 0.90 (t, 6H).

Analysis found: C, 57.90%; H, 5.97%; N, 9.61%. Calculated C, 57.99%; H, 5.98%; N, 9.66% for $RuC_{42}H_{52}N_6O_4S_2$.

3.1.5. Synthesis of [Ru(H_2dcbpy)(tdbpy)(NCS)$_2$] N621 (H_2dcbpy = 4,4'-dicarboxy-2,2'-bipyridine, tdbpy = 4,4'-tridecyl-2,2'-bipyridine)

Using the same conditions as for complex N820, starting from ligand 4,4'-tridecyl-2,2'-bipyridine the title compound was obtained . Yield, 60%.

^{1}H NMR (δ_H/ppm in CD_3OD) 9.70 (d, 1H), 9.3 (d, 1H), 9.1 (s, 1H), 8.95 (s, 1H), 8.55 (s, 1H), 8.40 (s, 1H), 8.28 (d, 1H), 7.95 (d, 1H), 7.70 (d, 2H), 7.65 (d, 1H), 7.41 (d, 1H) 7.15, 3.15 (t), 2.7(t), 1.9 (m), 1.45 (m), 0.98 (t).

Analysis found: C, 60.95%; H, 7.08%; N, 8.45%. Calculated C, 61.13%; H, 6.98%; N, 8.56% for $RuC_{50}H_{68}N_6O_4S_2$.

3.2. Characterization

3.2.1. Synthetic Studies: Scheme **4** shows the details of the synthetic strategy adopted for the preparation of hydrophobic heteroleptic complexes. During the reaction, aliquots of the intermediate products were withdrawn and characterized by NMR and UV/Vis spectra. Reaction of dichloro(p-cymene)ruthenium(II) dimer in N,N'-dimethylformamide (DMF) solution at 60°C with 4,4'-substituted-2,2'-bipyridine (L) ligand resulted a mononuclear complex. In this step, coordination of substituted bipyridine ligand to the ruthenium center takes place with cleavage of the doubly chloride-bridged structure of the dimeric complex.[39] The proton NMR spectra of the mononuclear complex show three pyridine protons (two doublets and one singlet) and two cymene protons (two doublets) in the aromatic region. The presence of three protons clearly testifies that the bipyridine ligand is trans to the cymene group.

The heteroleptic dichloro complexes were prepared by reacting the mononuclear [Ru(4,4'disubstituted-2,2'-bpy)Cl(cymene)]Cl complex with the H_2dcbpy ligand in DMF under reduced light at 150°C. The UV/Vis spectral properties of $[Ru(L)(L')(Cl)_2]$ (L = 4,4'-dicarboxy-2,2'-bipyridine, L' = 4,4'-dialkyl-2,2'-bipyridine) complexes are identical to the same complexes prepared by using the $RuCl_2(DMSO)_4$ method.[37] Displacement of the cymene ligand from the coordination sphere of ruthenium metal by substituted bipyridine ligand takes place efficiently in organic solvents (ethanol and DMF) even under dark at 100°C. However, when the reaction was carried out in ethanol, formation of ≈15% *trans* isomer is evident. Therefore, it is necessary to use high boiling solvents to reflux the reaction mixture at 150°C in order to obtain the more thermodynamically stable *cis* geometrical isomer.

The $[Ru(L)(L')(Cl)_2]$ complex was reacted with 30 fold excess of ammonium thiocyanate ligand to obtain the $[Ru(L)(L')(NCS)_2]$ complex. Scheme 5 shows the structures of amphiphilic heteroleptic sensitizers. The NMR of the crude complex shows presence of 95% N-bonded and 5% S-bonded isomers, which were separated on a Sephadex, LH-20 column of 2 x 30 cm, using methanol as an eluent.

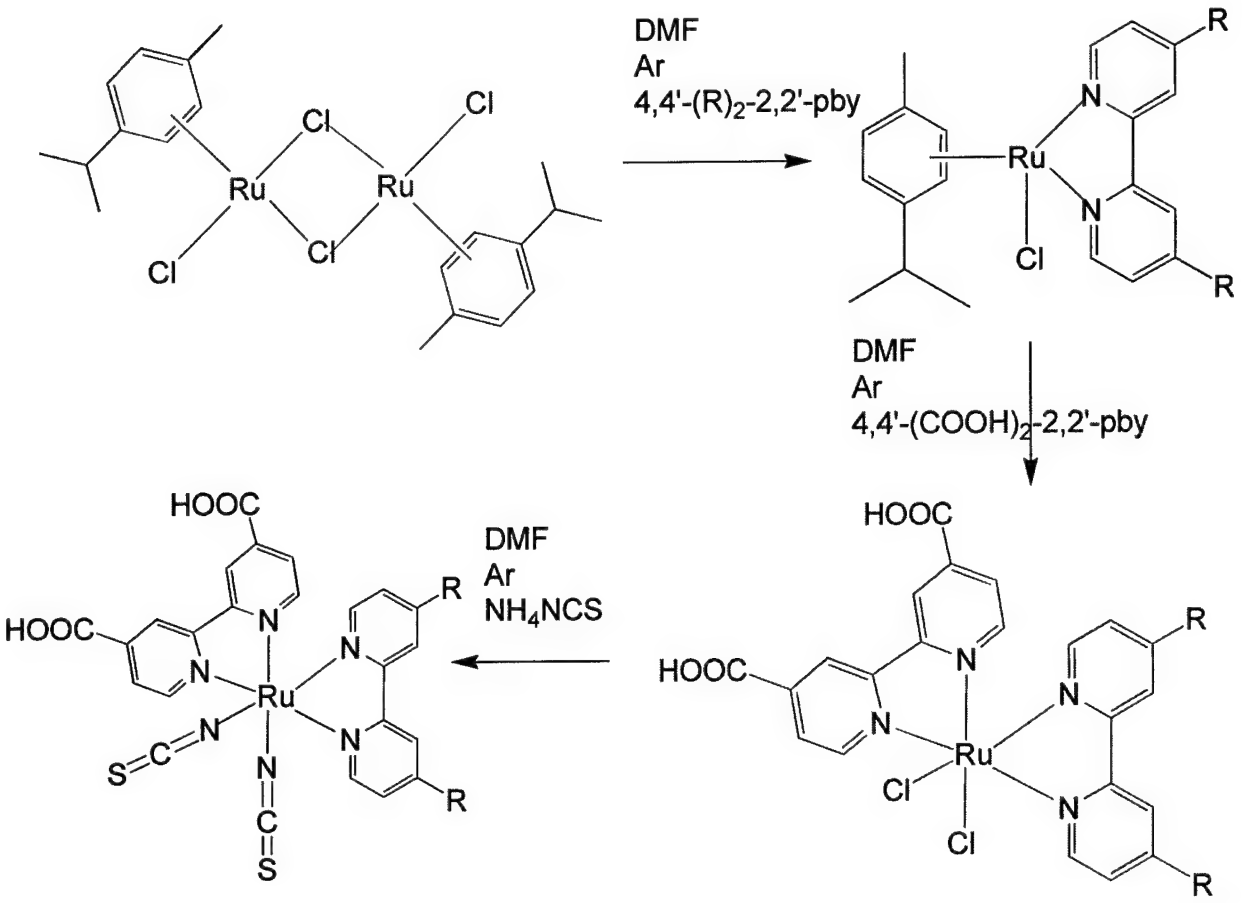

Scheme 4. The synthetic strategy adopted for the preparation of *cis*-amphiphilic heteroleptic complexes.

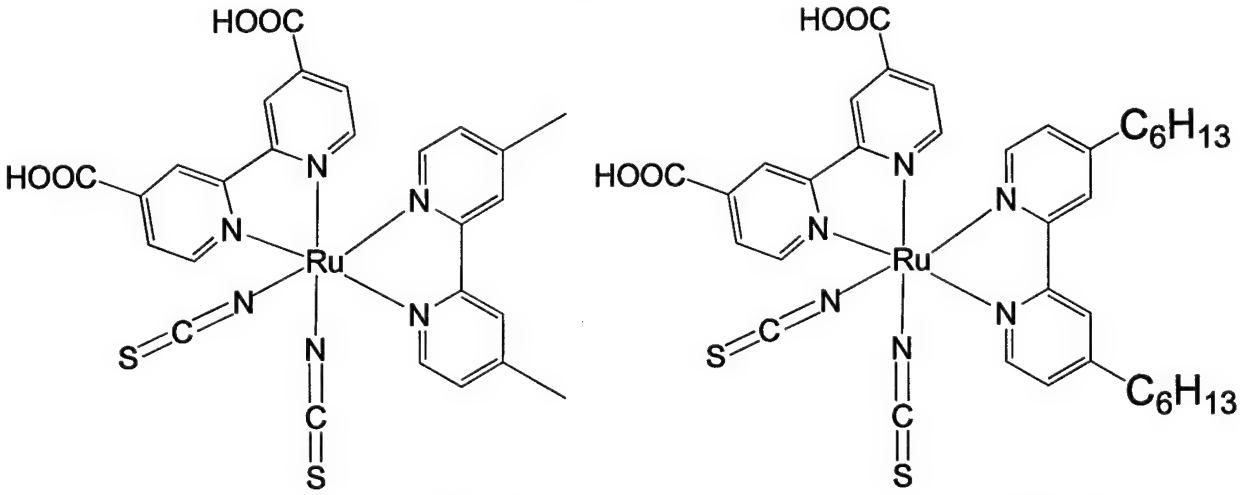

N820 **N823**

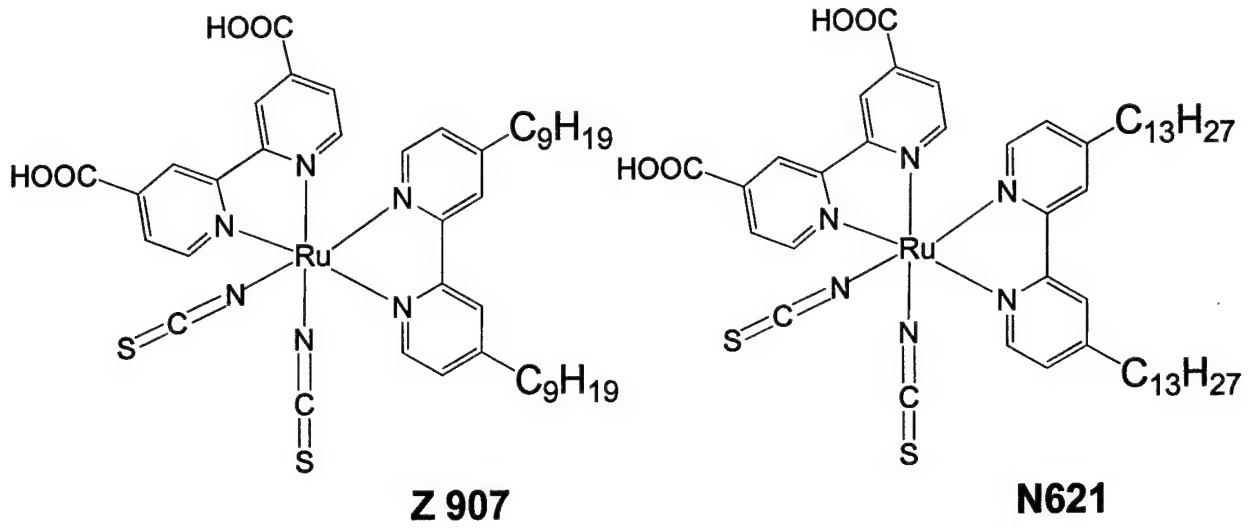

Scheme 5. Structures of amphiphilic heteroleptic sensitizers

3.2.2. NMR spectral data: The NMR spectrum of complex [Ru(L)Cl(p-cymene)]Cl displays two doublets and a singlet at □ 9.49; 8.89 and 8.11 ppm due to H6, H3 and H5 protons, respectively. The cymene aromatic protons are observed as two doublets at □ 6.15 and 5.90 ppm. Proton NMR spectra of the intermediate dichloro heteroleptic complex [Ru(L)(L')$(Cl)_2$] (L = 4,4'-dicarboxy-2,2'-bipyridine, L' = 4,4'-dialkyl-2,2'-bipyridine) is complicated in DMSO-d_6 solvent because of labile nature of the chloride ligands. Nevertheless, in CD_3OD solvent the chloride ligands seem to be stable and the proton NMR spectra of the dichloro heteroleptic complexes show expected peaks, which are down field shifted compared to the cis-dithiocyanate complexes.

The symmetry in heteroleptic complexes is lowered when compared to the corresponding homoleptic complexes. Hence, the NMR spectra of these complexes are expected to be much more complicated. In theses complexes the two halves of each ligand is necessarily in different magnetic environment. Figure 28 shows a representative proton NMR spectrum of N621 complex, which show 12 resonance peaks in the aromatic region.

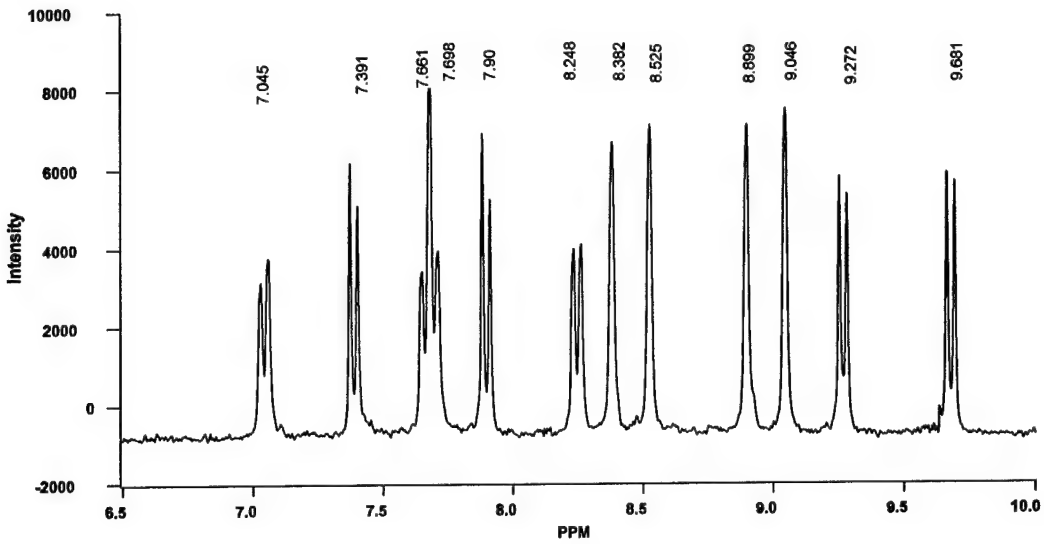

Figure 28. Proton NMR specrum of complex N621 in CD_3OD.

3.2.3. ^{13}CNMR. Carbon 13 NMR spectra of these heteroleptic complexes were useful to identify the mode of coordination of thiocyanate ligand. The N-coordinated thiocyanate carbon resonance peak has been reported in number of complexes at 130 - 135 ppm.[40] In these complexes the two peaks at 136-133 ppm are due to the N- coordinated thiocyanate ligand, which are trans to the carboxylic acid pyridine and alkyl substituted pyridine, respectively. In the aromatic region (δ 170-120 ppm), these complexes show 22 resonance signals corresponding to 22 carbons of two different bipyridyl ligands. The peaks between δ 10–50 ppm, are due to the aliphatic resonance carbon signals. A representative ^{13}C NMR spectrum of complex N621 is shown in Figure 29.

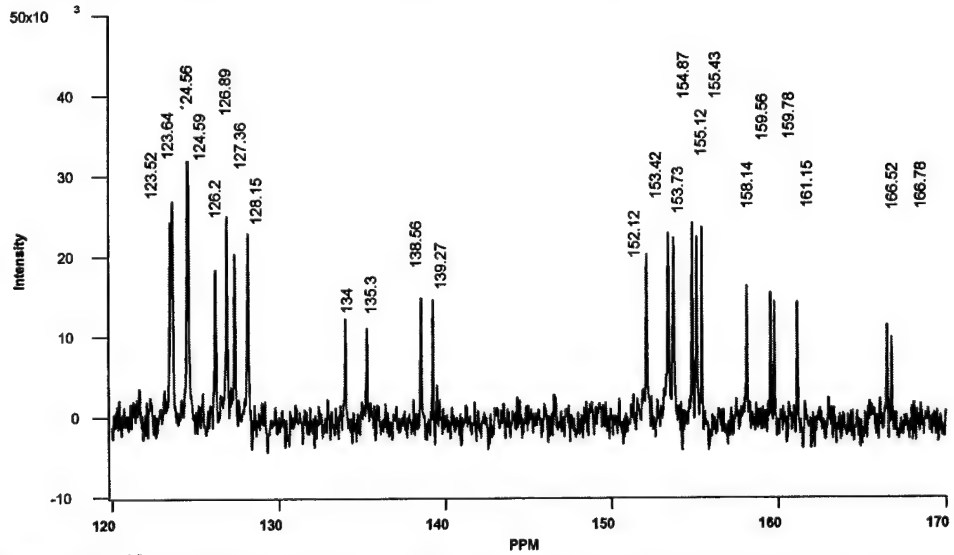

Figure 29. ^{13}C NMR spectrum of the complex **2** measured in CD_3OD solvent.

3.2.4. ATR-FTIR Spectral data. ATR-FTIR spectra of these amphiphilic heteroleptic sensitizers measured as a solid samples show a strong broad band in the region of at 1700 cm^{-1} due to carboxylic acid groups. The intense peak in the region of 1230 cm^{-1} is due to □(C-O) stretch.[41] The banddue to□(NC) of the thiocyanate ligand was observed in the range of 2100-2115 cm^{-1} in these complexes. The adsorbed complexes on TiO_2 film show the presence of carboxylate asymmetric 1593 cm^{-1} □($-COO^-_{as}$) and symmetric 1383 cm^{-1} □($-COO^-_s$) bands together with a strong□(NC) of the thiocyanate group at 2103 cm^{-1}. The presence of carboxylate bands in the IR spectra of adsorbed complexes on TiO_2 testify that the two carboxylic acid groups are dissociated and involved in the adsorption on the TiO_2 surface.

3.2.5. Electronic Spectra. The amphiphilic heteroleptic sensitizers show broad and intense visible bands between 390 to 540 nm region due to metal-to-ligand charge transfer transitions that are assigned to metal-to-ligand charge-transfer (MLCT) origin. The bands in the UV region at 295 and 312 nm are assigned to intra ligand (π-π^*) charge transfer transitions of 4,4'-alkylsubstituted-2,2'-bpy and dcbpy ligands, respectively.[42] The lowest MLCT band in amphiphilic heteroleptic sensitizers is blue shifted by 15 nm compared to the homoleptic complex *cis*-dithiocyanatobis(4,4'-dicarboxylic acid-2,2'-bipyridine)Ruthenium(II).

Table 4. Absorption, Photophysical and Electrochemical Properties of the Ruthenium Complexes

Complex	[a] Abs. max. (nm) (□/10^4 M^{-1} cm^{-1})			[b] Em. □max	[c] □ (ns)	[d] $E_{1/2}$ Ox (ΔE)/V	[d] $E_{1/2}$ Red (ΔE)/V
	$\tilde{\pi}\pi^*L^1$	$\tilde{\pi}\pi^*L^2$	dπ-π*			$Ru^{III/II}$	4,4'-dcbpy
N820	295 (4.54)	312 (3.35)	383 (1.13) 524 (1.16)	750	37	0.78 (0.08)	-1.5 (0.09)
N823	296 (4.26)	312 (3.20)	384 (1.01) 525 (1.11)	760	29	0.73 (0.1)	-1.57 (0.07)
Z907	295 (4.24)	312 (3.01)	385 (1.09) 526 (1.16)	769	27	0.74 (0.08)	-1.62 (0.07)
N621	296 (4.21)	312 (3.02)	384 (1.08) 525 (1.15)	760	29	0.74 (0.08)	-1.60 (0.07)
N3		314 (4.82)	398 (1.4) 539 (1.42)	830	20	0.85	-

[a] The data are referred to the protonated complexes measured in ethanol. L1 and L2 represents 4,4'-dialkyl-2,2'-bpy and 4.4'-dcbpy, respectively. [b] Emission data were obtained by exciting at lowest energy MLCT band at 530 nm, without degassing at room temperature. The recorded

values ± 2 nm.[c] Measured in ethyl alcohol at room temperature. [d]The electrochemical data were measured in DMF solvent with 0.1 M tetrabutyl ammonium hexafluorophosphate using a gold (or glassy carbon) electrode. The reported data is V vs. SCE

Deprotonation of the COOH groups in amphiphilic heteroleptic sensitizers blue shifts the $\tilde{\pi}\pi^*$ charge transfer band from 312 to 310 nm and the low energy MLCT band from 540 to 514 nm (Figure 30). The blue shift is due to an increase in the energy of the LUMO of the ligand, causing the $\tilde{\pi}\pi^*$ and $d\tilde{\pi}\pi^*$ transitions to occur at higher energies. However, the band at 294 nm due to 4,4'-alkyl-2,2'-bpy $\tilde{\pi}\pi^*$ charge transfer transition, is unaffected in the pH range 2 to 12. In amphiphilic heteroleptic sensitizers, the molar extinction coefficient of the $\tilde{\pi}\pi^*$ charge transfer transitions of 4,4'-dialkyl-2,2'-bipyridine is 35 - 40% higher than compared to the molar extinction coefficient of 4,4'-dicarboxy-2,2'-bipyridine $\tilde{\pi}\pi^*$ charge transfer transitions. There are also two shoulders at 360 and 500 nm, which are tentatively attributed to a metal-to-ligand charge transfer transitions involving the 4,4'-alkyl-2,2'-bpy ligand. The molar extinction coefficient of the lowest energy MLCT band in amphiphilic heteroleptic sensitizers is 25% lower compared to the *cis*-dithiocyanatobis(4,4'-dicarboxylic acid-2,2'-bipyridine)Ruthenium(II) complex. For comparison, the UV/Vis spectral data of homoleptic complex of *cis*-dithiocyanatobis(4,4'-dicarboxylic acid-2,2'-bipyridine)Ruthenium(II) complex , were included in Table 4.

The absorption spectra of the amphiphilic heteroleptic sensitizers anchored on 6 □m thick TiO_2 nanocrystalline electrode show the low energy MLCT maximum at 528 nm, which is considerably red shifted compared to the solution spectra of deprotonated complex in ethanol. This is due to the fact that on the electrode the carboxylate groups bind to the TiO_2 surface in which Ti^{4+}acts as an electron acceptor similar to proton causing slight decrease the LUMO of dcbpy. The amphiphilic heteroleptic sensitizers adsorbed onto the TiO_2 surface is slightly higher in quantity compared to the standard N3 dye. The amount of dye adsorbed on the 6 □m thick TiO_2 nanocrystalline electrode from dilute solutions of 3×10^{-4} M in 1:1 acetonitrile and *tert*-butanol over 24 hours is comparable to the dye adsorbed from 9×10^{-3} M solution in DMF over 30 minutes.

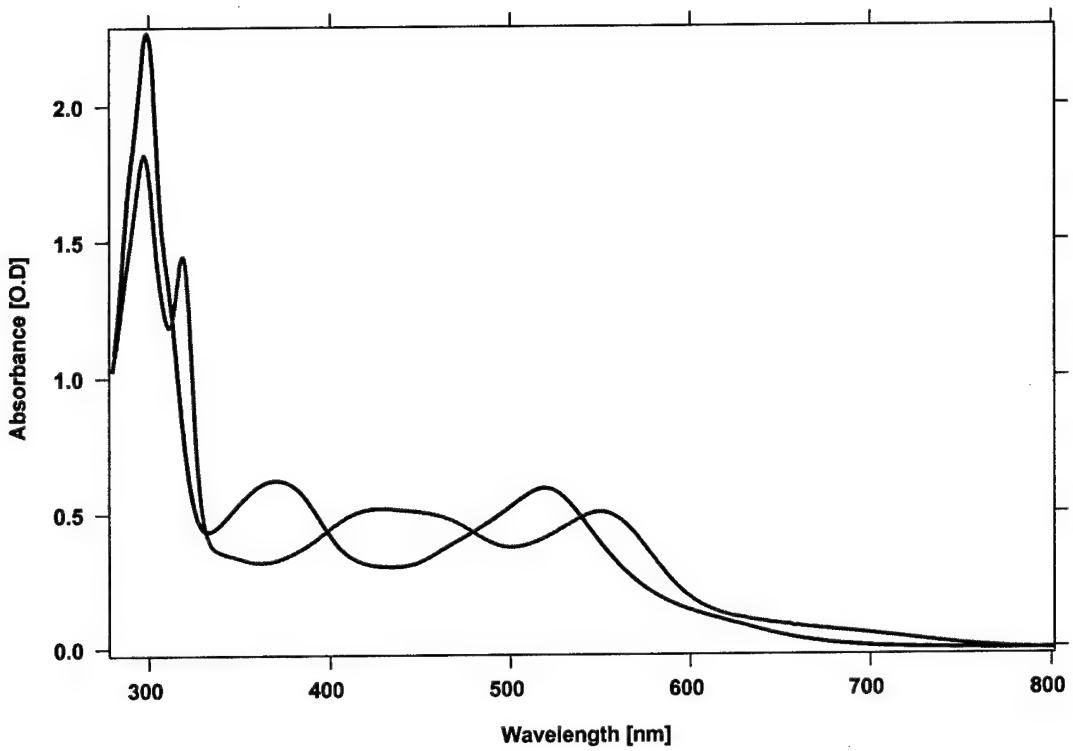

Figure 30. UV/Vis absorption spectrum of the deprotonated complex **2**. The concentration of the solution was 3.5 x 10^{-5} M in ethanol.

3.2.6. Emission Spectra. Emission data of the amphiphilic heteroleptic sensitizers were obtained for air saturated solutions at room temperature by exciting at 530 nm in ethanol solution. The emission maxima of theses complexes in de-protonated state is at a higher energy and is more intense as compared with that observed from protonated form. Emission lifetime data are consistent with the trend observed in emission intensities. The red-shifted emission from the protonated form of the complexes is due to stronger π-acceptor properties of the COOH group lowering the energy of the CT excited state. The π orbital of the protonated ligand is lower in energy than that of the deprotonated form. The shorter-lived emission lifetime in the acid form of the complexes is due to proton-induced quenching of the excited state.[43] Figure 31 shows a representative absorption and emission spectra of the complex Z907.

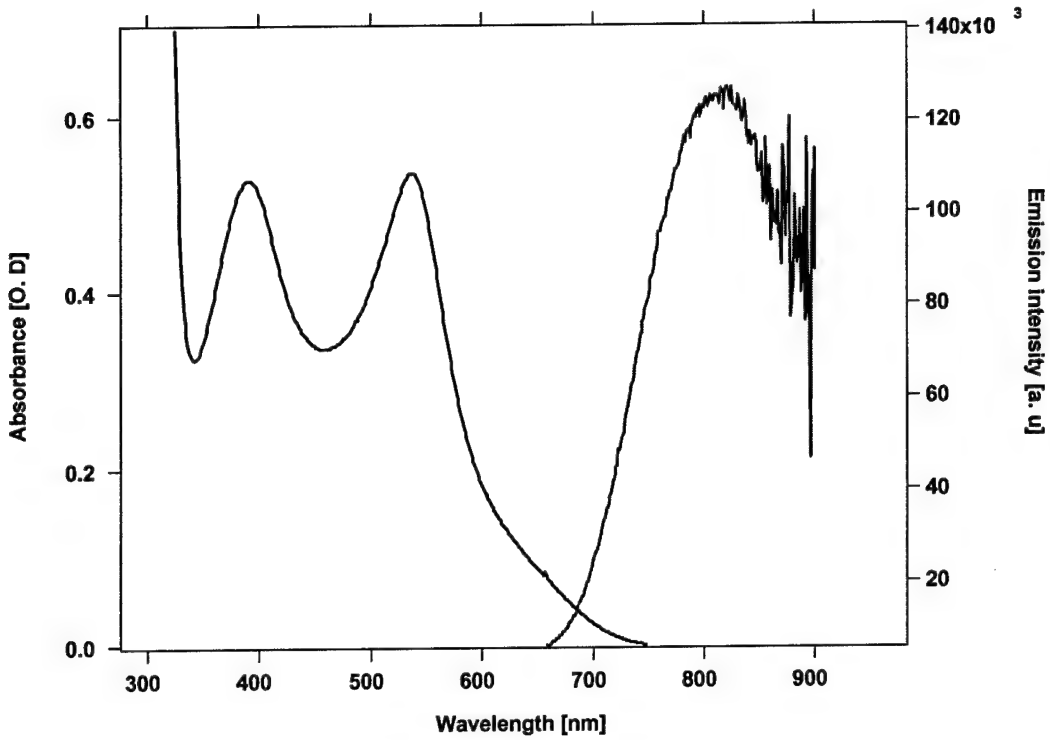

Figure 31. UV/Vis absorption and emission spectra of Z907 complex measured in DMF

3.2.7. Electrochemical data. Electrochemical data of the amphiphilic heteroleptic sensitizers measured using a gold or a glassy carbon electrode in DMF solvent with 0.1 M tetrabutyl ammonium hexaflurophosphate are compiled in Table 4. As observed the amphiphilic heteroleptic sensitizers displayed one ruthenium-centered oxidation and two ligand based reduction couples between 1.0 to -1.9 V vs., SCE. Figure 32 shows a typical cyclic voltammogram of the Z907 complex, measured using a gold electrode with scan rate of 1000 mV /s. Upon scanning to positive potentials a quasi reversible couple at $E_{1/2}$ = 0.74 V vs. SCE with a separation of 0.08 V between anodic to cathodic peak was observed due to the $Ru^{II / III}$ couple (Figure 31, process *B*). The couple at $E_{1/2}$ = 0.46 V vs., SCE labeled as *A* is due to ferrocenium/ferrocene couple, which were used as an internal standard. The ruthenium oxidation potential in Z907 complex is shifted cathodically by 0.11 V, compared to the *cis*-dithiocyanatobis(4,4'-dicarboxylic acid-2,2'-bipyridine)Ruthenium(II) couple. The difference (0.11 V) in the oxidation potential of Z907 complex compared to the N3 complex is due to presence of 4,4'nonyl-2,2'-bpy in Z907, which is a stronger donor when compared to the 4,4'-dicarboxylic acid-2,2'-bipyridine.

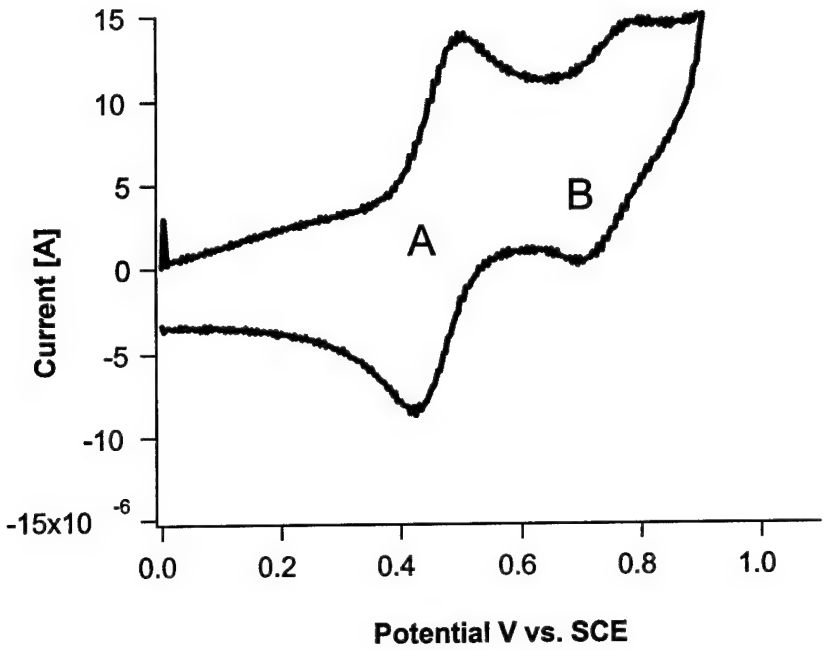

Figure 31. Cyclic voltammogram of Z907 complex measured in DMF solution containing 0.1 M TBA(PF_6) using a gold electrode with scan speed of 1000 mV /s. The couple labeled as A at $E_{1/2}$ = 0.46 V vs., SCE is due to ferrocenium/ferrocene, which was used as an internal standard. The couple labeled as B at $E_{1/2}$ = 0.74 V vs., SCE is due to the $Ru^{III/II}$.

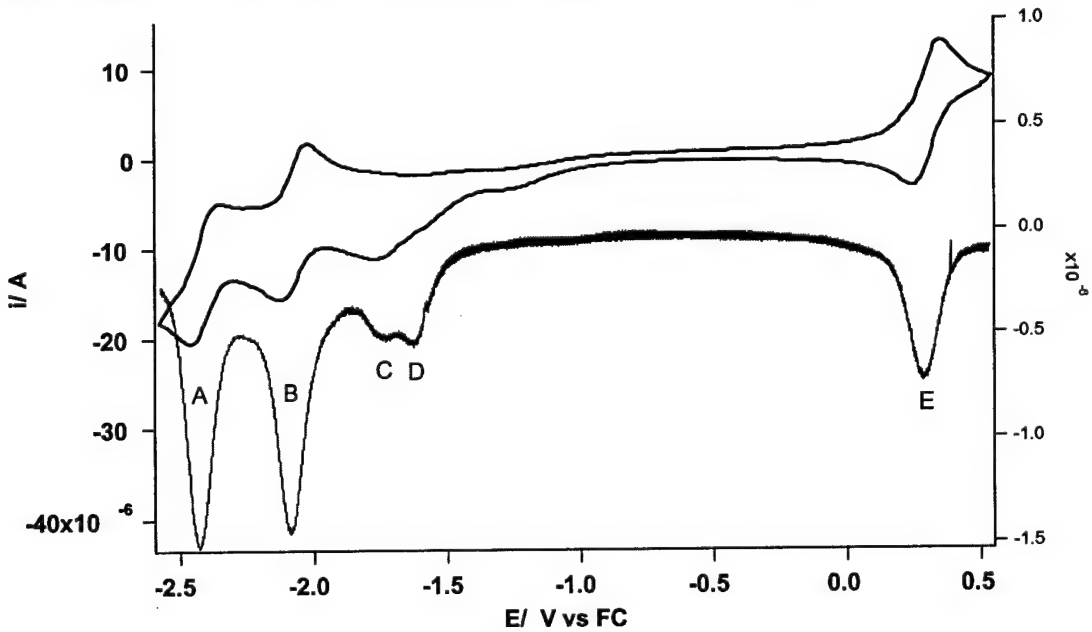

Figure 32 Cyclic voltammogram of complex N621 measured in DMF solution containing 0.1 M TBA(PF_6) using a gold electrode with scan speed of 1000 mV /s. The couple labeled as A at $E_{1/2}$

= 0.46 V vs., SCE is due to ferrocenium/ferrocene, which was used as an internal standard. The couple labeled as B at $E_{1/2}$ = 0.74 V vs., SCE is due to the $Ru^{III/II}$.

The amphiphilic heteroleptic sensitizers, when scanning towards negative potentials with 1000 mV/s an irreversible wave and two quasi-reversible waves were observed (Figure 32). The irreversible wave at –1.24 V vs., SCE is due to reduction of carboxylic acid protons to hydrogen. Wolfbauer et al., has observed a similar behavior deprotonation, followed by reduction of protons of the $dcbpyH_2$ ligand in $[Ru(dcbpyH_2)_2(NCS)_2]$ complex at platinum electrode.[44] However, on a glassy carbon electrode this process is absent. Based on the electrochemical properties of homoleptic complexes of *cis*-dithiocyanatobis(4,4'-dicarboxylic acid-2,2'-bipyridine)Ruthenium(II) the two quasi-reversible waves at $E_{1/2}$ = -1.62 and -1.88 V vs., SCE are assigned to the reduction of dcbpy and 4,4'-alkyl-2,2'-bpy ligands, respectively. The separation between the anodic and the cathodic peaks of the first reduction couple is 0,07 V, and the second couple is 0,11 V.

3.2.8. Photovoltaic performance. The TiO_2 electrodes were heated at 400 °C for 20 minutes before dipping them into the dye solution. The electrodes were left for 18-22 hours in dilute solution of 3 x 10^{-4} M in ethanol or 1:1 acetonitrile + *tert*-butanol. Alternatively, a measured volume of the concentrated solution 9 x 10^{-3} M in DMF was pipetted (10 µl for 0.5 cm^2 TiO_2 area) onto the surface of the TiO_2 electrode and the dye solution left for 10-30 minutes. The dye-coated electrodes were rinsed quickly with acetonitrile and used as such for photovoltaic measurements. The photovoltaic performance of cells dipped between for 30 minutes in concentrated solution and 18 hours in dilute solution are similar.

A comparison of the efficiency of a sandwich-type cell with 12 +4 µm thick TiO_2 films sensitized by amphiphilic heteroleptic sensitizers were shown Figure 33. The data are collected using an electrolyte having composition of 0.6M N-methyl-*N*-butyl imidiazolium iodide, 0.05 M iodine, 0.05 M LiI and 0.5 M *tert*-butylpyridine in a 50 : 50 (v/v) mixture of valeronitirile and acetonitrile. It is interesting to note that under identical conditions the short circuit photocurrent density of amphiphilic heteroleptic sensitizers slightly increases with increasing chain length. The photo voltage of the cell containing the complex N820 is lower than the N621 complex. The Very similar data were obtained for TiO_2 electrodes, which were dipped for 30 minutes in dye solutions of 9 x 10^{-3} M in DMF.[25] The important effect asserted by the 4 µm thick 400 nm particles layer is evident in the red region of the IPCE curve. The incident monochromatic photon-to-current conversion efficiency at 700 nm is twice as high for the TiO_2 film containing a

scattering layer as compared to the 7 μm thick TiO_2 film without a scattering layer.

The photocurrent action spectra obtained with the TiO_2 films coated with a monolayer of complex Z907 in a sandwich cell under illumination by simulated AM 1.5 solar light is shown in Figure 34. The incident monochromatic photon-to-current conversion efficiency (IPCE) is plotted as a function of excitation wavelength showing a plateau region at 90%. The photocurrent action spectra of the amphiphilic heteroleptic complexes show broad features covering a large part of the visible spectrum. From the overlap integral of this curve with the standard global AM 1.5 solar emission spectra one measures a short circuit photocurrent density of 17 mA/cm^2. In agreement with this measurement under standard global AM 1.5 solar conditions the cell gave a photo-current density of 17.3 mA/cm^2, 760 mV open circuit potential and 0.75 fill factor yielding close to 9.86 % efficiency.

Figure 33. Comparison of the efficiency obtained using complexes N820, N823, Z907 and N621 on 12 + 4 μm thick thick TiO_2 electrodes under AM 1.5 sun. The composition of the electrolyte used in these measurements is 0.6M M-methyl-*N*-butyl imdiazolium iodide, 0.05 M iodine, 0.05 M LiI and 0.5 M *tert*-butylpyridine in a 50 : 50 (v/v) mixture of valeronitirile and acetonitrile.

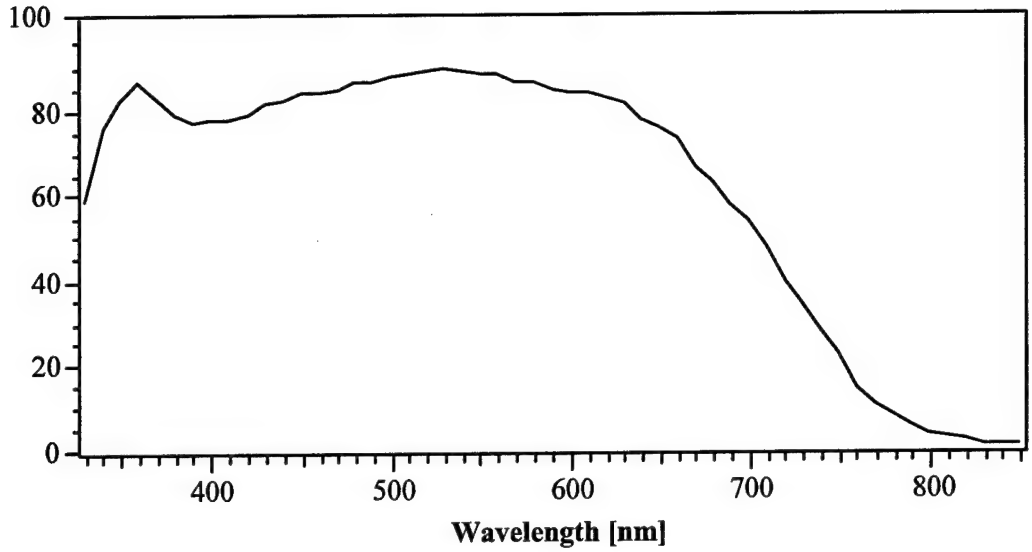

Figure 34 Photocurrent action spectrum obtained with the Z907 complex attached to nanocrystalline TiO_2 film. The incident photon to current conversion efficiency is plotted as a function of the wavelength of the exciting light. The electrolyte composition was 0.6M N-methyl-*N*-butyl imidiazolium iodide, 0.05 M iodine, 0.05 M LiI and 0.5 M *tert*-butylpyridine in a 50:50 (v/v) mixture of valeronitrile and acetonitrile.

3.2.9. Photovoltaic stability, Figure 35 presents a typical photocurrent density-voltage curve for cells based on the Z-907 dye and the polymer gel electrolyte under AM 1.5 sunlight illumination. The short-circuit photocurrent density (J_{sc}), open-circuit voltage (V_{oc}), and fill factor (FF) are 12.5 mA cm^{-2}, 730 mV and 0.67, respectively, yielding an overall energy conversion efficiency (η) of 6.1%.[45] The action spectrum of the photocurrent is shown in the inset of Fig. 35. The photon-to-current conversion efficiency (IPCE) reaches a maximum efficiency of 80% at 540 nm. The photovoltaic performance obtained with ionic liquid and polymer gel electrolytes is almost identical indicating that gelation has no adverse effect on the conversion efficiency.

The use of the amphiphilic Z-907 ruthenium dye in conjunction with the polymer gel electrolyte was found to result in remarkably stable device performance both under thermal stress and light soaking. The high conversion efficiency of the cell was sustained even under heating for 1,000 h at 80 °C, maintaining 94 % of its initial value after this time period as shown in Fig. 36. Devices using liquid electrolyte retained only 88 % of their initial performance under the same conditions. The difference may arise from a decrease in solvent permeation across the sealant in the case of the solid polymer gel as compared to the liquid electrolyte. Tolerance of such a severe thermal stress by a DSC having over 6% efficiency is unprecedented. So far, dye sensitised solar

cells have been plagued by performance degradation at temperatures between 80 and 85 °C. The best result obtained in previous studies was a decline in conversion efficiency from initially 4.5 to 3 % when the cell was maintained over 875 h at 85 °C.

After the first week of aging the efficiency was moderately enhanced due to an increase in the J_{sc} and FF values. Then a gradually small decrease in the V_{oc} without much variation in J_{sc} and FF caused a decrease in the overall efficiency by 6%. This is well within the limit of thermal degradation accepted for silicon solar cells. The devices also showed excellent photostability when submitted to accelerated testing in a solar simulator at 100 mW cm^{-2} intensity. Thus after 1,000 h of light soaking at 55°C the efficiency had dropped by less than 5 % for cells covered with a UV absorbing polymer film. The efficiency difference for devices tested with and without the polymer film was only 4 % at AM 1.5 sunlight indicating a very small sacrifice in efficiency due to UV filter.

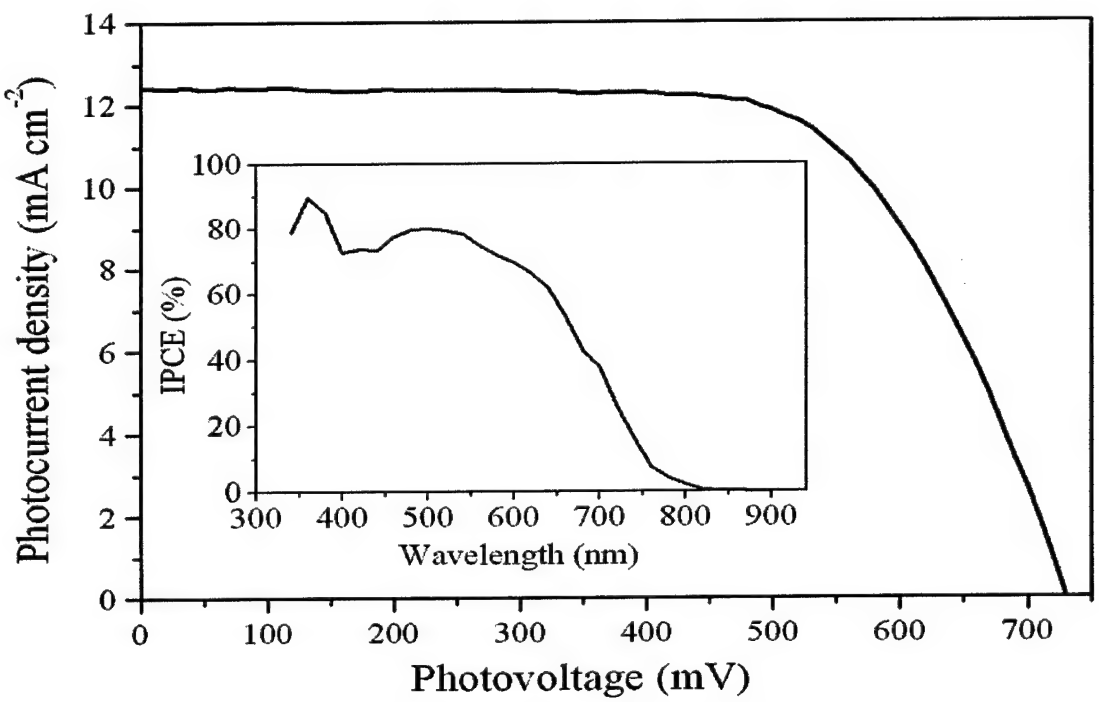

Figure 35 Typical photocurrent density–voltage characteristic of photovoltaic cells with the polymer gel electrolyte and Z-907 dye at an irradiance of AM 1.5 sunlight (99.8 mW cm^{-2}). Cell area: 0.152 cm^2. The inset is IPCE for the quasi-solid-state cells.

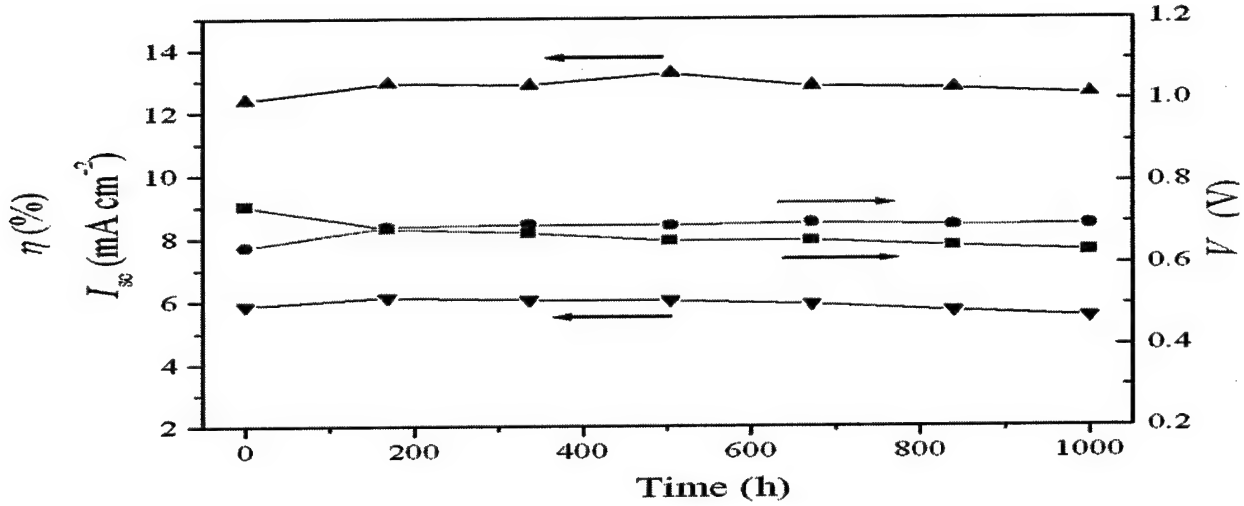

Figure 36. Detail device parameter variation for cells with polymer gel electrolyte during accelerated aging at 80 °C.

4. Ruthenium sensitizers with antenna and extended π-system

The idea of using antenna effect for converting UV light to visible light is of relevance for dye-sensitized solar cell applications. The feasibility of such an approach was carried out, with the dye (Z910) shown in Figure 37. Experiments carried out with this sensitizer on TiO_2 resulted in significant photocurrents leading to 10.3% global conversion efficiency under simulated AM 1.5 sunlight conditions.

A two-step synthesis was used to afford ligand containing antenna and extended π-system 4,4'-di-(2- (4-methoxyphenyl) ethenyl)-2,2'-bipyridine. First, a nucleophilic addition of the anion of 4,4'-dimethyl-2,2'-bipyridine to *meta*-methoxybenzaldehyde gave the corresponding alcohol. Dehydration was achieved using acetic acid with an easy separation by chromatography separation. The corresponding sensitizer (Z-910) was synthesized using the procedure applied for the amphiphilic heteroleptic sensitizers starting from $[RuCl_2(p\text{-cymene})]_2$ dimer.

4.1. Synthesis

4.1.1. 4,4'-di-(2-hydroxy-2-(3-methoxyphenyl)ethyl)-2,2'-bipyridine (A). Scheme 6 shows the reactions steps and the conditions applied for the ligand synthesis. Lithium diisopropyl amide (LDA) was formed by mixing BuLi (5.92×10^{-3}mol) with DIPA (0.78 mL) in 20 mL THF at -60°C under N_2. The LDA solution was stirred at room temperature for 30 minutes and cooled to -

40°C. 4,4'-dimethyl-2,2'-bipyridine (0.5 g, 2.48×10^{-3} mol) dissolved in 20 mL THF was added to the LDA through a double tipped needle, the cooling bath was removed and the black reaction mixture was then stirred at room temperature during one hour. After cooling the reaction to -60°C, a solution of 3-methoxybenzaldehyde (0.727 mL, 2.48×10^{-3} mol) diluted in 10 mL THF was added through a double tipped needle. A yellow precipitate was formed. Stirring was continued for three hours, then the mixture was stirred into water and extracted with CH_2Cl_2 (1×100 mL). The organic phase was then washed with brine, dried over $MgSO_4$ and concentrated. NMR of the crude product showed more than 85% of conversion compared to the aldehyde and complete conversion compared to the bipyridine. The crude product **A** was used without further purification.

^{1}H NMR (200Mhz) ($CDCl_3$) δ 8.37 (2H, d, *J*= 5 Hz, pyridine), 8.21 (2H, broad s, pyridine), 7.24 (2H, t, *J*= 8.4 Hz, methoxyphenyl), 7.06 (2H, dd, J_1= 5 Hz, J_2= 1.6 Hz, methoxyphenyl), 6.93 (4H, m, benzylic -CH_2- + methoxyphenyl), 6.80 (2H, d, J_1= 8.4 Hz, J_2= 1.8 Hz, broad s), 4.98 (2H, m, benzylic -C*H*(OH)-), 3.77 (6H, s, -OCH_3), 3.03 (4H, m, benzylic -CH_2-). ^{13}C NMR, 159.7, 155.6, 148.9, 148.8, 145.4, 129.5, 125.0, 122.2, 118.1, 113.3, 111.1, 74.2, 55.2, 45.5.

4.1.2. 4,4'-di-(2-(3-methoxyphenyl) ethenyl)-2,2'-bipyridine (DMPEbpy). The crude **A** was dissolved in conc. AcOH (10 mL, excess) and the mixture was stirred under reflux for 18 hours. When the reaction mixture was cooled to room temperature, the product precipitated and **B** was obtained with a yield of 36% (0.378 g, 0.898×10^{-3} mol) from 4,4'-dimethyl-2,2'-bipyridine.

^{1}H NMR ($CDCl_3$) δ 8.69 (2H, d, *J*= 4.8 Hz, pyridine), 8.61 (2H, s, pyridine), 7.47 (2H, *J*= 16.4 Hz, d, vinylic), 7.43 (2H, d, *J*= 4.8 Hz, pyridine), 7.32 (2H, t, *J*= 7.6 Hz, methoxyphenyl), 7.18 (2H, d, methoxyphenyl), 7.14 (4H, d, J_1= 16 Hz, broad s, vinylic+ methoxyphenyl), 6.90 (1H+1H, d, J_1= 7.6 Hz, broad s), 3.87 (s, 6H, -OCH_3). ^{13}C NMR, 49.5, 148.9, 133.3, 129.8, 126.4, 124.9, 122.2, 121.1, 119.7, 118.4, 114.5, 112.1, 55.3, 21.2. IR (KBr) 3306, 2937, 1598, 1487, 1462, 1435, 1263, 1149, 1046, 783, 700. Anal. Calcd for $C_{28}H_{24}N_2O_2$: C, 79.98; H, 5.75; N, 6.66; Found: C, 79.11; H, 5.81; N, 6.56;

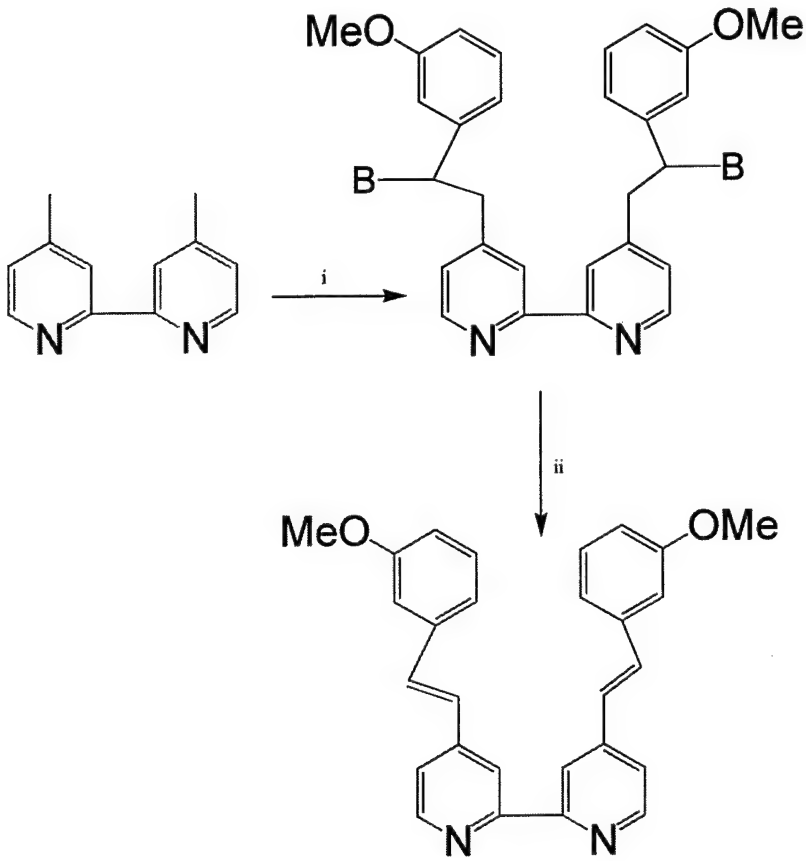

Scheme 6. *Reaction conditions:* i) a) 2.2 eq. LDA, THF, -78 °C, N_2. ii) conc. AcOH, reflux

4.1.3. Synthesis of [Ru(H_2dcbpy)(BMPEbpy)(NCS)$_2$] (Z910) (H_2dcbpy = 4,4'-dicarboxy-2,2'-bipyridine, BMPEbpy = 4,4'-di-(2-(3-methoxyphenyl) ethenyl)-2,2'-bipyridine)

Using the same conditions as for complex N820, starting from ligand 4,4'-di-(2-(3-methoxyphenyl) ethenyl)-2,2'-bipyridine the title compound was obtained as a dark powder. Yield 65%.

^{1}H NMR (δ_H/ppm in CD_3OD+ NaOD) 9.4 (d, 1H), 9.2 (d, 1H), 8. 9 (s, 1H), 8.8 (s, 1H), 8.3 (s, 1H), 8.15 (s, 1H), 7.9 (d, 1H), 7.80 (d, 1H), 7.7 to 6.9 (m, 16H), 4.1 (s, 3H), 4.0 (s, 3H). Anal. Calc. for $RuC_{42}H_{34}N_6O_7S_2$: C, 56.0; H, 3.78; N, 9.34%. Found: C, 55.22; H, 3. 97; N, 9.39%.

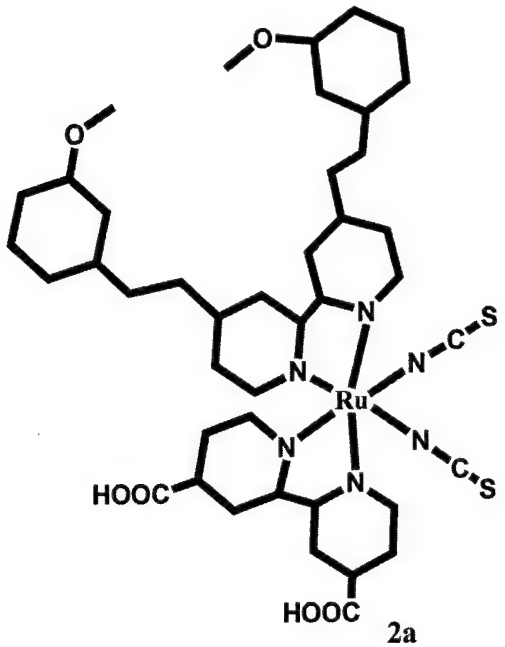

2a

Figure 37. Ruthenium sensitizer with antenna and extended π-system

5. Panchromatic Ruthenium Sensitizers

The optimal sensitizer for the dye-sensitized solar cell should be panchromatic, i.e. absorb visible light of all colours. Ideally, all photons below a threshold wavelength of about 920 nm should be harvested and converted to electric current. In order to absorb the light below 920 nm, the redox level (energy levels) of the sensitizer needs to be tuned. The metal-to-ligand charge-transfer transitions can be tuned to lower energy in two ways. Firstly, by introducing a ligand with a low lying π* molecular orbital and secondly by the destabilization of the metal t_{2g} orbitals with a strong donor ligand. In an effort to integrate the concepts of donor and acceptor in a single complex we have engineered at a molecular level and synthesized functionalized hybrid tetradentate ligands and their ruthenium complexes (Figure 38), which are expected to show thermal and photo stability. The donor units of the tetradentate ligand (*alkyl substituted*-pyridine) tune the metal t_{2g} orbital energies and the acceptor units (4,4'-methoxycarbonyl-2,2'bipyridine) tune the π* molecular orbitals. The axial coordination sites are used further to fine-tune the spectral and redox properties and to stabilise the hole that is being generated on the metal, after having injected an electron into the conduction band.

5.1. Synthesis.

5.1.1. 4',4''-Diethoxycarbonyl-2,2':6',2'':6'',2'''-quaterpyridine (L^1). Tetrahydrofurane (20 ml) was added to a mixture of $NiBr_2(PPh_3)_2$ (100 mg, 0.144 mmol), Zinc (120 mg, 1.89 mmol) and tetraethylammonium iodide (Et_4NI, 60 mg, 0.233 mmol) under nitrogen at room temperature. The resulting green color of the solution changed gradually to dark red. Ethyl-6-bromo-2,2'-bipyridine-4'-carboxylic ester (70 mg, 0.23 mmol) was separately dissolved in THF and added to the above solution by syringe. After stirring for 16h at 50°C, the mixture was poured into 2M aqueous ammonia solution (60 ml). To the resulting mixture was added chloroform (100 ml). The organic layer was separated and the aqueous phase was extracted with chloroform (3x30 ml). The combined organic phases were washed with water (5x50 ml), saturated NaCl-solution (50 ml). The organic layer was dried ($MgSO_4$) and solvent was removed. To the resulting residue, concentrated hydrochloric acid (20 ml) was added and then, extracted with dichloromethane (3x30 ml). The aqueous phase was cautiously neutralized with solid sodium carbonate. After extraction with dichloromethane (4x40 ml) the combined organic phases were dried ($MgSO_4$) and the solvent was removed. Compound $\mathbf{L^1}$ was then purified on silica gel with dichloromethane / hexane : 3 / 2. Yield: 30 mg (58%).

^1H NMR ($CDCl_3$): □ 9.16 (2H, d, *J* 1.50, $H^{3'}$); 9.03 (2H, d, *J* 1.50, $H^{5'}$); 8.75 (2H, m, H^6); 8.71 (2H, md, *J* 7.80, H^3); 7.92 (2H, ddd, *J* 8.30, *J* 7.80, *J* 1.95, H^4); 7.39 (2H, ddd, *J* 8.30, *J* 7.80, *J* 1.95, H^5); 4.52 (4H, q, *J* 6.90, CH_2); 1.50 (6H, t, *J* 6.90, CH_3).

Anal. found: C, 68.64; H, 5.01; N, 12.26%; Calc. for $C_{26}H_{22}N_4O_4$: C, 68.71; H, 4.88; N, 12.33%.

5.1.2. Synthesis of $[Ru(L^1)Cl_2]$. $[Ru(p\text{-cymene})Cl_2]_2$ (61 mg, 0.1 mmol) was dissolved in ethanol (50 mL) by heating. To this orange solution was added ligand $\mathbf{L^1}$ (100 mg, 0.2 mmol) and the mixture was refluxed for 6 h. The black precipitate which formed was filtered and washed with ethanol to yield the title compound as a dark powder (120 mg, 90%).

Anal. Found: C, 49.31; H, 3.7; N, 8.95%; Calc. for $C_{26}H_{22}N_4O_4Cl_2Ru$: C, 49.79; H, 3.54; N, 8.93%.

5.1.3. Synthesis of $[Ru(L^1)(SCN)_2]$. To a solution of complex $Ru(L^1)Cl_2$ (42 mg) in DMF (35 mL) was added ammonium thiocyanate (350 mg) in water (15 mL). The reaction mixture was heated at 140 °C for 3 h. The solution was allowed to cool to room temperature. The black

precipitate, which formed was filtered washed thoroughly with water and dried under vacuum to yield the title compound as a dark powder (10 mg, 23%). The resulted crude complex was further purified using a Sephadex LH-20 column.

^{1}H-NMR (CD_3OD, □ppm, *J* Hz): 9.72 (2H, d, H^6 *J* 6.); 8.99 (2H, s, $H^{3'}$); 8.93 (2H, s, $H^{5'}$); 8.70 (2H, d, $H^{3'}$ *J* 8); 8.38 (2H, t, H^4; *J* 6); 8.01 (2H, t, H^5 *J* 6); 4.49 (4H, q, *J* 7, CH_2); 1.42 (6H, t, *J* 7, CH_3).

Anal. Found: C, 49.91; H, 3.32; N, 12.85%;. Calc. for $C_{28}H_{22}N_6O_4S_2Ru$: C, 50.06; H, 3.30; N, 12.51%.

5.2. Characterization

5.2.1. Synthetic Studies. The ligand $\mathbf{L^1}$ was obtained in 58% yield by coupling ethyl-6-bromo-2,2'-bipyridine-4'-carboxylic ester in presence of $NiBr_2(PPH_3)_2$ catalyst.[46] The [Ru(*p*-cymene)Cl_2]$_2$ complex was reacted with $\mathbf{L^1}$ ligand in ethanol under an argon atmosphere to obtain the corresponding *trans*-dichloro species in good yield. However, refluxing in DMF solvent gave lower yields. Reaction of the *trans*-dichloro complexes with a large excess of the ambidentate thiocyanate ligand in DMF and water solution resulted in a mixture of linkage isomers. The major isomer (about 95%) is the complex with two N-bonded isothiocyanates. The isomer ratios were estimated by integrating the H-6 ^{1}H NMR signals, where the isomers show distinctly different positions.[32] These isomers were separated on a Sephadex LH-20 column using an eluent 1:5 DMF/methanol mixture.

5.2.2. NMR Spectroscopy Studies. The ^{1}H NMR spectra of the ligands show sharp signals in the aromatic region, however their corresponding ruthenium complexes exhibit slightly broader signals. The complex [Ru(L^1)$(SCN)_2$] exhibit two singlets due to H3' and H5' protons of the central two pyridine rings. The two doublets and the two triplets were assigned to H3 and H6 and H4 and H5, respectively. The coordination induced chemical shift (CIS), □complex - □ligand) is positive, which can be considered as a measure of donor strength of the ligand.

5.2.3. IR spectral data. The ATR-FTIR spectra of [Ru(L^1)$(SCN)_2$] complex show a broad band at 3465 cm^{-1}, due to □(O-H) water molecules. The complex exhibit characteristic ring stretching modes in the region between 1620-1450 cm^{-1} and NCS band at 2085 cm^{-1}, due to υ(CN) of the N-coordinated thiocyanate ligand. The peak at 1719 cm^{-1} due to carbonyl group υ(C=O) and the

intense band at 1240 is assigned to the ϋC-O) stretch. The methyl stretching modes are located at 2960 cm^{-1} and 3063 cm^{-1}.

5.2.4. Electrochemical Studies. The cyclic voltammogram of complex $[Ru(L^1)(SCN)_2]$ measured in DMF solvent containing 0.1 M tetrabutylammonium tetrafluoroborate shows a chemically reversible wave at $E_{1/2}$ = 750 mV (vs. AgCl/Ag), which is attributed to the $Ru^{III/II}$ redox couple. The separation between the cathodic and the anodic wave at a scan rate of 500 mV/s, is 60 mV. The i_{ox}/i_{red} peak current is substantially greater than unity due to the oxidation of the thiocyanate ligand subsequent to the oxidation of the ruthenium(II) center. The standard equilibrium potential for thiocyanogen / thiocyanate couple is 0.53 V vs. SCE in aqueous and non-aqueous solvents. Surely, the standard equilibrium potential for coordinated thiocyanate shifts anodically compared to the thiocyanogen/thiocyanate couple due to electron donation to the metal. Nevertheless, the oxidation of metal at 0.75 V may still lead to the oxidation of thiocyanate ligand. It is interesting to note that the thiocyanate containing ruthenium complexes are quite reversible provided that the oxidation potential of the complex is around 0.5 - 0.6 V. In a cathodic scan, the complex $[Ru(L^1)(SCN)_2]$ display reduction wave at –1.35 V, however in the reverse scan the re-oxidation peak corresponding to the reduction wave, is absent. These waves are assigned to the irreversible reduction of the tetradentate ligand.

5.2.5. Electronic Spectra. The $[Ru(L^1)(SCN)_2]$ complex is very weakly soluble in common organic solvents such as acetonitrile, ethanol, methanol and dichloromethane. However, in DMF and DMSO the complex is soluble enough to measure the NMR, cyclic voltammetry and electronic spectral properties. Figure 39 shows a comparison of UV-visible spectra of the $[Ru(L^1)(SCN)_2]$ complex with N719. The absorption spectrum of $[Ru(L^1)(SCN)_2]$ complex in DMF solution shows four broad absorption bands in the visible region at 657, 613, 487 and 360 nm due to be metal-to-ligand charge-transfer (MLCT). The bands in the UV at 289 and 324 nm with a shoulder at 355 nm is assigned to intra ligand $\tilde{\pi}\pi^*$transition.

5.2.6. Emission Spectra. The complex $[Ru(L^1)(SCN)_2]$, when excited within the MLCT absorption band in an air-equilibrated DMF solution, show a luminescence maximum at 900 nm with a lifetime of 30 (±1) ns. The emission spectral profile is independent of excitation wavelength and the excitation spectrum matches well with the absorption spectrum.

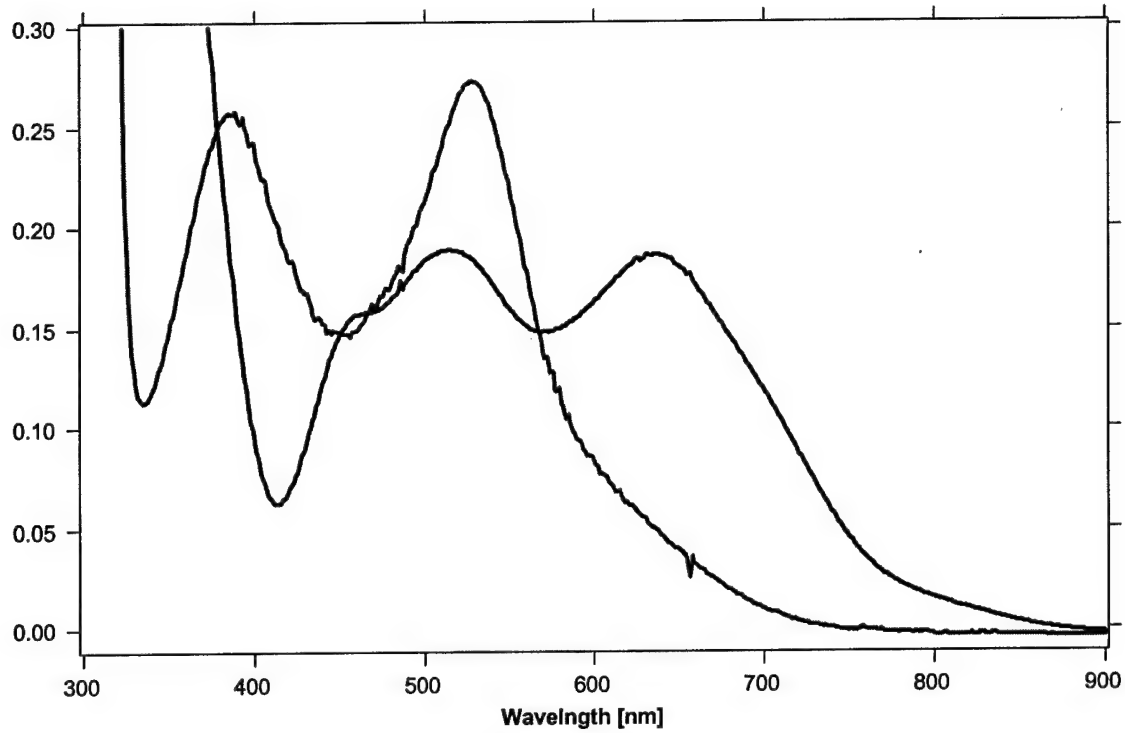

Figure 39. Comparison of UV/Vis Absorption Spectra of N719 and trans-[Ru(L^1)$(NCS)_2$]

5.3. Photovoltaic data. The initial studies of the films sensitized by [Ru(L^1)$(NCS)_2$] complex into a photoelectrochemical 'sandwich' solar cell employing an electrolyte that contains 0.6 M dimethylpropylimidazolium iodide, 0.1M of iodine, 0.5 M *tert*-butylpyridine and 0.1 M of lithium iodide in methoxyacetonitrile were performed. The photocurrent action spectrum of such a cell where the incident photon to current conversion efficiency is plotted as a function of wavelength show broad features covering the entire visible spectrum and extending into the near IR region up to 940 nm. The incident photon-to-current conversion efficiency (IPCE) value in the plateau region being about 75%. The overlap integral of this curve with the standard global AM 1.5 solar emission spectrum yields a short circuit photocurrent density (isc) of 18 ± 0.5 mA/cm^2. The open circuit potential (Voc) is 650 ± 50 mV and the fill factor (ff) is 0.65 ± 0.05. A current of 18 mA/cm^2 for a 12 □m thick TiO_2 electrodes under AM 1.5 solar emission spectrum is really impressive. Therefore, we believe that the panchromatic light harvesting properties of these complexes combined with nearly quantitative electron injection from the excited dye into the conduction band of the nanocrystalline TiO_2 film should supercede that of the N3 sensitizer after optimization of the open circuit potential and the fill factor

6. New sensitizers

In an effort to overcome the problems associated with lower LUMO of quaterpyridine ligands, we are developing novel tetradentate ligands containing oxygen and nitrogen linkers in collaboration with Prof. Viscardi (Dipartimento di Chimica, Università di Torino, Italy). The linker atoms are expected to rip apart the conjugation of quaterpyridyl ligands resulting more negatively shifted LUMO of its ruthenium complexes with respect to TiO_2 conduction band (Figure 40). The shifting of LUMO level is imperative to obtain high quantum yields of electron injection onto TiO_2 conduction band. The proposed ruthenium complexes in all probability show absorption properties in the visible and the near IR region, which should lead to significant increase in a short circuit photocurrent density under AM 1.5 sun. The details of the ligand synthetic plan are shown in scheme 7. The research based on these new concepts is in progress at EPFL.

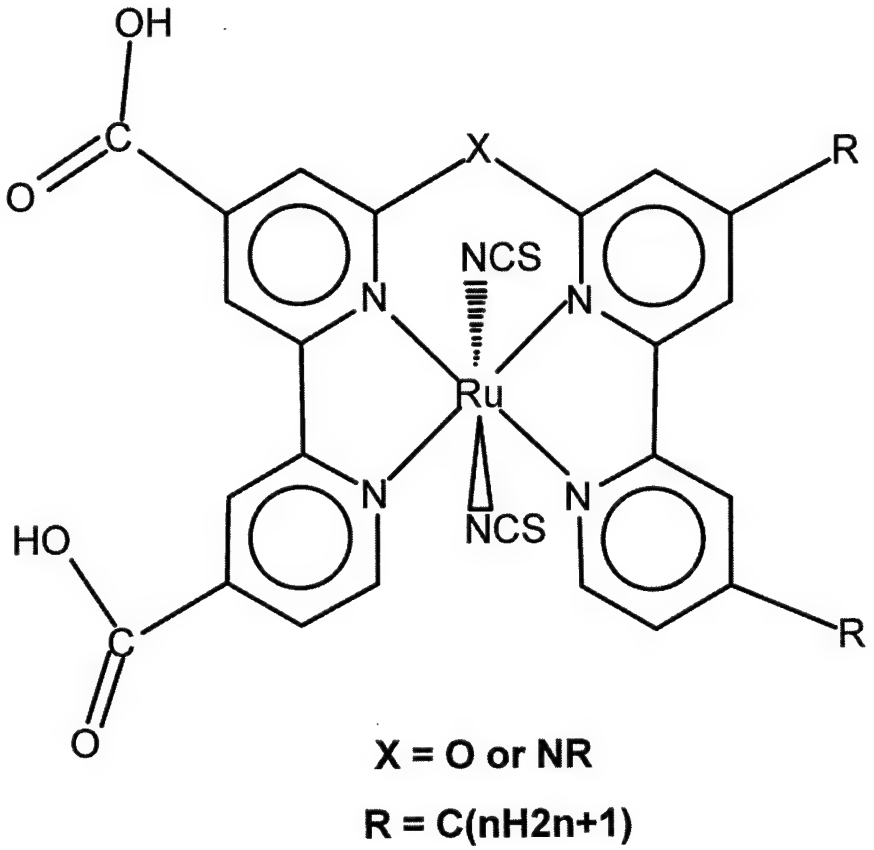

Figure 40. Proposed panchromatic sensitizers

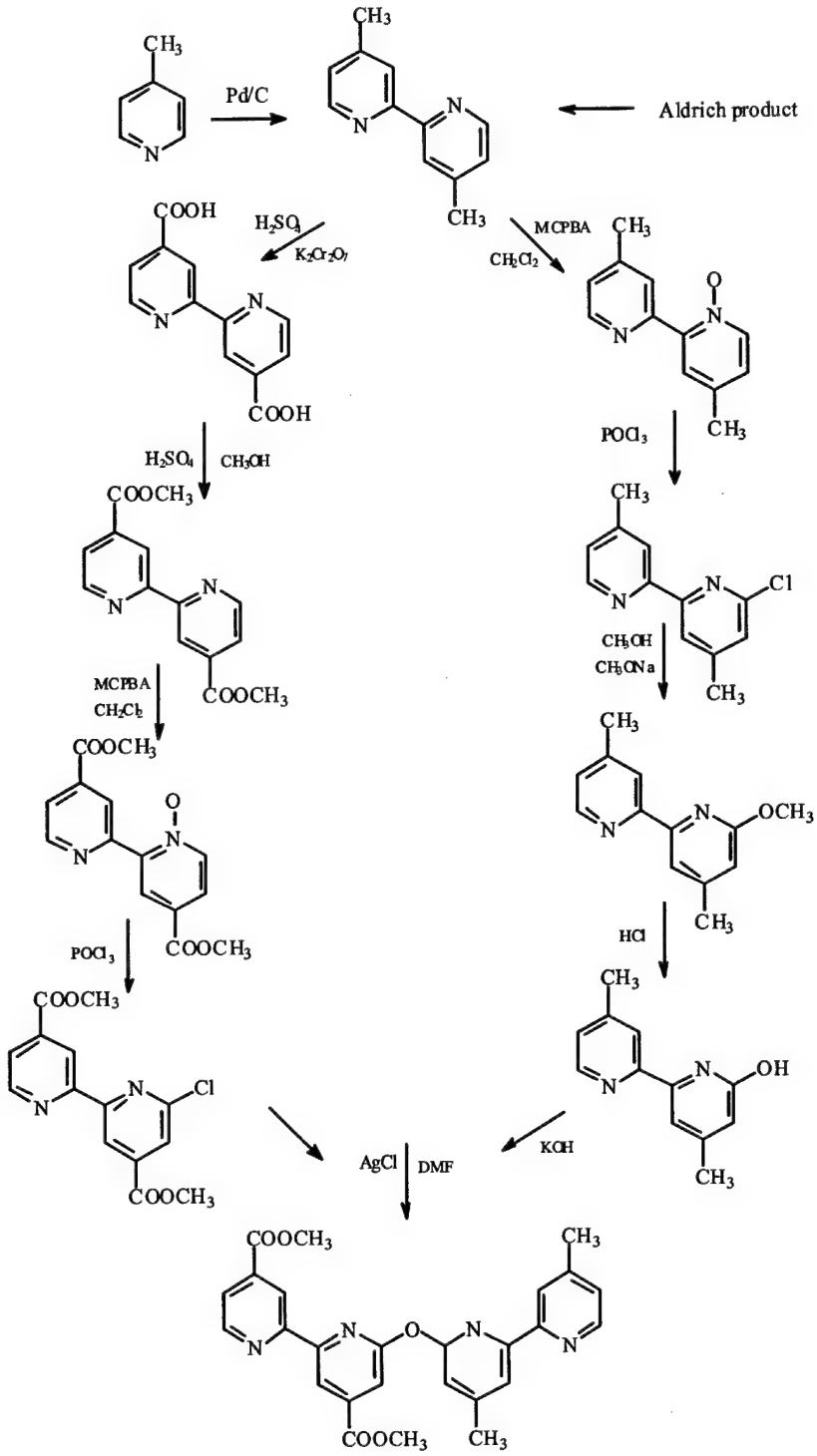

Scheme 7. Synthetic scheme applied for synthesis of 4,4'-dimethyl-4'',4'''-dimetghoxycarbonyl-2,2';6',2'';6'',2'''-quaterpyridine.

References

[1] M. Grätzel, *Nature* **2001**, *414*, 338.
[2] G. Rothenberger, P. Comte, M. Graetzel, *Solar Energy Mat. Solar Cells* **1999**, *58*, 321.
[3] G. Rothenberger, P. Comte, M. Grätzel, *Solar Energy Materials $ Solar Cells* **1999**, *58*, 321.
[4] M. K. Nazeeruddin, P. Pe'chy, T. Renouard, S. M. Zakeeruddin, R. Humphry-Baker, P. Comte, P. Liska, C. Le, E. Costa, V. Shklover, L. Spiccia, G. B. Deacon, C. A. Bignozzi, M. Gra1tzel, *J. Am. Chem. Soc.* **2001**, *123*, 1613.
[5] M. K. Nazeeruddin, E. Muller, R. Humphry-Baker, N. Vlachopoulos, M. Grätzel, *J. Chem. Soc. Dalton Trans.* **1997**, 4571.
[6] K. G. Brooks, S. D. Burnside, V. Shklover, P. Comte, F. Arendse, A. J. McEvoy, M. Grätzel, in *Proc. Am. Ceram. Soc.*, Indianapolis, **1999**.
[7] N. Papageorgiou, P. Liska, A. Kay, M. Graetzel, *J. Electrochem.Soc.* **1999**, *146*, 898.
[8] Y. Tachibana, J. E. Moser, M. Graetzel, D. R. Klug, J. R. Durrant, *J. Phys. Chem.* **1996**, *100*, 20056.
[9] M. K. Nazeeruddin, A. Kay, I. Rodicio, R. Humphry-Baker, E. Muller, P. Liska, N. Vlachopoulos, M. Grätzel, *J. Am. Chem. Soc.* **1993**, *115*, 6382.
[10] M. Turrion, J. Bisquert, P. Salvador, *J. Phys. Chem. B* **2003**, *107*, 9397.
[11] J. van de Lagemaat, A. J. Frank, *J. Phys. Chem. B* **2000**, *104*.
[12] D. Cahen, G. Hodes, M. Grätzel, J. F. Guilemoles, I. Riess, *J. Phys. Chem. B* **2000**, *104*, 2053.
[13] J. Ferber, J. Luther, *J. Phys. Chem. B* **2001**, *105*, 4895.
[14] M. K. Nazeeruddin, R. Humphry-Baker, M. Grätzel, D. Wöhrle, G. Schnurpfeil, G. Schneider, A. Hirth, N. Trombach, *J. Porphyrins and Phthalocyanines* **1999**, *3*, 230.
[15] A. Juris, V. Balzani, F. Barigelletti, S. Campagna, P. Belser, A. von Zelewsky, *Coord. Chem. Rev.* **1988**, *84*, 85.
[16] G. A. Crosby, *Acc. Chem. Res.* **1975**, *8*, 231.
[17] T. J. Meyer, *Acc. Chem. Res.* **1978**, *11*, 94.
[18] K. Kalyanasundaram, *Coord. Chem. Rev.* **1982**, *46*, 159.
[19] R. Krause, *Structure and bonding, Springer-Verlag* **1987**, *67*, 1
[20] S. Ernst, W. Kaim, *Inorg. Chem.* **1989**, *28*, 1520.
[21] A. Launikonis, P. A. Lay, A. W. H. Mau, A. M. Sargeson, W. H. F. Sasse, *Aust. J. Chem.* **1986**, *39*, 1053.
[22] M. J. Root, B. P. Sullivan, T. J. Meyer, E. Deutsch, *Inorg. Chem.* **1985**, *24*, 2731.
[23] M. K. Nazeeruddin, S. M. Zakeeruddin, R. Humphry-Baker, M. Jirousek, P. Liska, N. Vlachopoulos, V. Shklover, C. H. Fischer, M. Grätzel, *Inorg. Chem.* **1999**, *38*, 6298.
[24] M. K. Nazeeruddin, R. Humphry-Baker, P. Liska, M. Grätzel, *J. Phys. Chem. B* **2003**, *107*, 8981.
[25] M. K. Nazeeruddin, R. Splivallo, P. Liska, P. Comte, M. Grätzel, *Chem. Chommun.* **2003**, 1456.
[26] P. Chen, T. J. Meyer, *Chem. ReV.* **1998**, *98*, 1439.
[27] J. C. Curtis, B. P. Sullivan, T. J. Meyer, *Inorg. Chem* **1983**, *22*, 224.
[28] K. Kalyanasundaram, M. K. Nazeeruddin, *Inorg. Chem.* **1990**, *29*, 1888.
[29] P. J. Giordano, C. R. Bock, M. S. Wrighton, L. V. Interrante, R. F. X. Williams, *J. Am. Ceram. Soc.* **1977**, *99*, 3187.
[30] M. K. Nazeeruddin, K. Kalyanasundaram, *Inorg. Chem.* **1989**, *28*, 4251.
[31] K. S. Finnie, J. R. Bartlett, J. L. Woolfrey, *Langmuirr* **1998**, *14*, 2744.
[32] G. B. Deacon, R. Phillips, *J. Coord. Chem. Rev.* **1989**, *33*, 227.
[33] A. Vittadini, A. Selloni, F. P. Rotzinger, M. Grätzel, *J. Phys. Chem. B* **2000**.
[34] K. Westermark, H. Rensmo, H. Siegbahn, K. Keis, A. Hagfeldt, *J. Phys. Chem. B* **2002**, *106*, 10102.
[35] A. Nasar, M. K. Nazeeruddin, M. Gra1tzel, *Thermochimica Acta.* **2000**, *348*, 105.

[36] Y. Tachibana, M. K. Nazeeruddin, M. Graetzel, D. R. Klug, J. R. Durrant, *Chem. Phys.* **2002**, *284*, 127.
[37] S. M. Zakeeruddin, M. K. Nazeeruddin, R. Humphry-Baker, P. Pechy, P. Quagliotto, C. Barolo, G. Viscardi, M. Graetzel, *Langmuir* **2002**, *18*, 952.
[38] D. K. Ellison, R. T. Iwamoto, *Tetrahedron Letters* **1983**, *24*, 317.
[39] S. B. Wendicke, E. Burri, R. Scopelliti, K. Severin, *Organometallics* **2003**, *22*, 1894.
[40] M. K. Nazeeruddin, S. M. Zakeeruddin, R. Humphry-Baker, S. I. Gorelsky, A. B. P. Lever, M. Grätzel, *Cooed. Chem. Rev.* **2000**, *208*, 213.
[41] A. Fillinger, B. A. Parkinson, *J. Electrochem. Soc.* **1999**, *146*, 4559.
[42] T. J. Meyer, *Pure Appl. Chem.* **1986**, *50*, 1293.
[43] K. Kalyanasundaram, M. K. Nazeeruddin, *Chem. Phys. Letters* **1992**, *193*, 292.
[44] G. Wolfbauer, A. M. Bond, G. B. Deacon, D. R. MacFarlane, L. Spiccia, *J. Am. Chem. Soc.* **2000**, *122*, 130.
[45] P. Wang, S. M. Zakeeruddin, J. Moser, M. K. Nazeeruddin, T. Sekiguchi, M. Graetzel, *nature materials* **2003**, *2*, 402.
[46] T. Renouard, R.-A. Fallahpour, M. K. Nazeeruddin, R. Humphry-Baker, S. I. Gorelsky, A. B. P. Lever, M. Grätzel, *Inorg. Chem.* **2002**, *41*, 367.

APPENDIX 2

A.1 Molecular Structures A1

A.1.1 spiro-MeOTAD A1

A.1.2 Dye Structures A2

A.1.3 Base Selection for interface Modification A3

A.1.4 Alternative redox mediator for verification of silver effect A3

A.2 Calculation of Mismatch Factor A4

A.3 Device Characterization at NREL A5

A.4 IMPS Model A6

A.1 Molecular Structures

A.1.1 spiro-MeOTAD

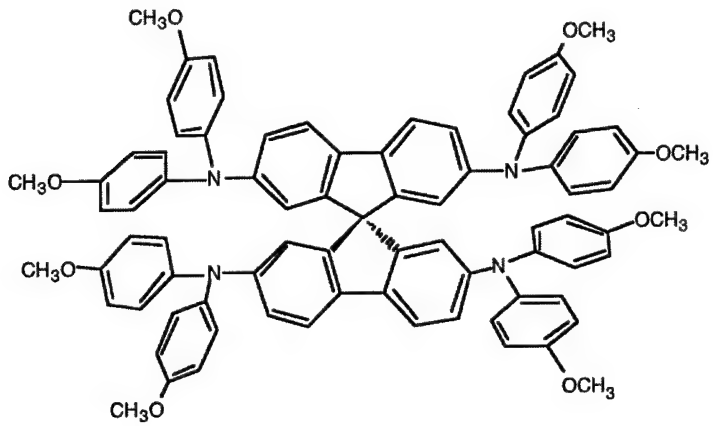

2,2',7,7'-tetrakis(N,N-di-p-methoxyphenyl-amine)-9,9'-spirobifluorene

Spectrum of spiro-MeOTAD and its oxidised form

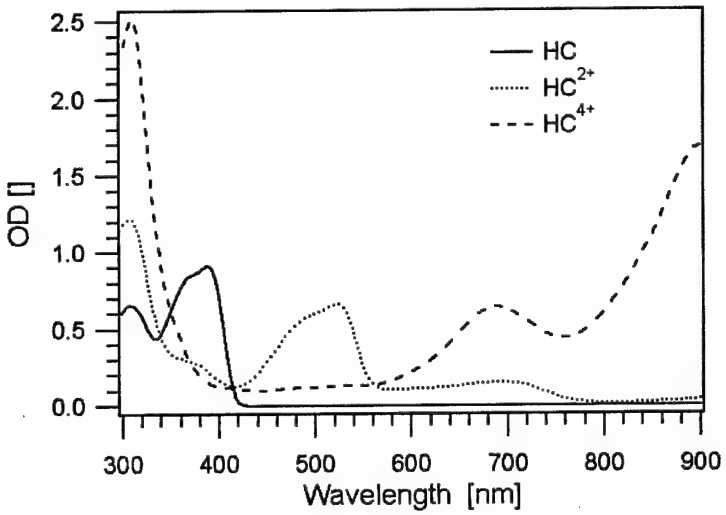

A.1.2 Dye Structures

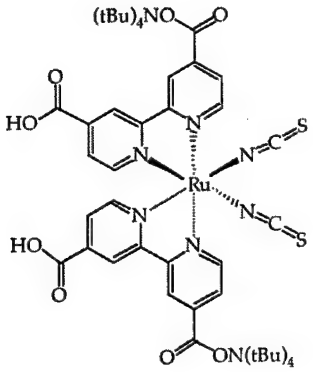

N719

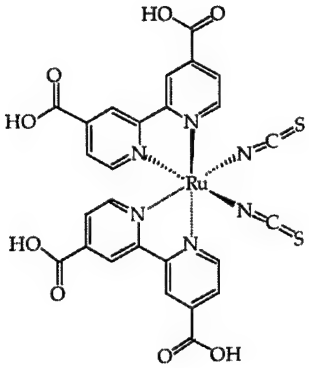

"Red Dye":N3

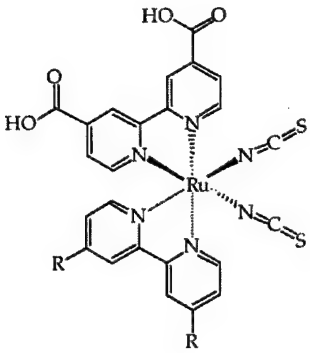

hydrophobic dye series

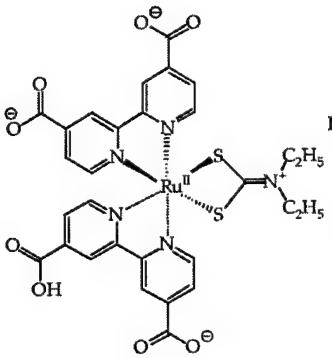

$TBA_2[Ru(dcbpyH_2)_2L]$

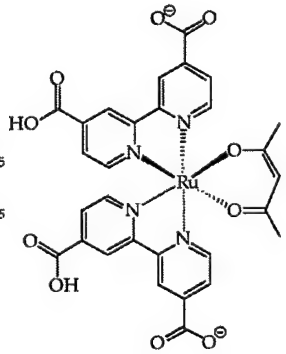

$TBA[Ru(dcbpyH_2)(dcbpyH)L]$

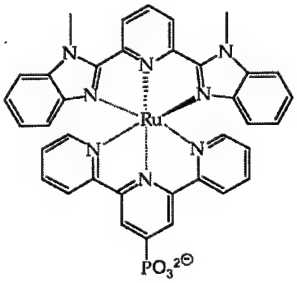

$[Ru(terpyH_2PO_3)(dmpip)]$

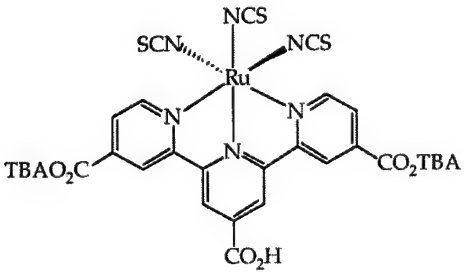

"Black Dye": N749

A.1.3 Base Selection for interface Modification

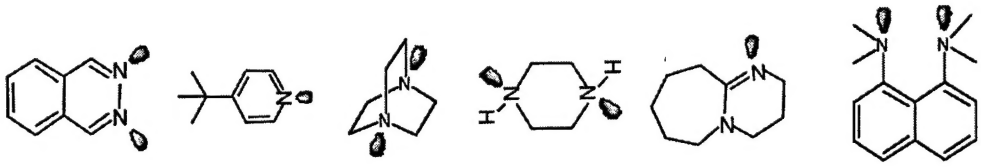

Phthalazine **tBP** **Dabco** **Piperazine** **DBU** **Proton sponge**

A.1.4 Alternative redox mediator for verification of silver effect

$Co^{II}(dbbip)_2^{2+}$

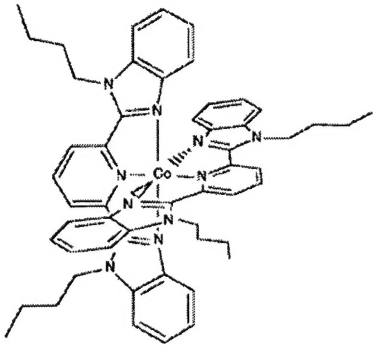

The picture was taken from: H. Nusbaumer, et al. *J. Phys. Chem. B* **2001**, *105*, 10461-10464. The charge-transporting medium consists of the cobalt complex in an electrolyte solution. Correspondingly, solar cells based on this redox mediator are DSSC.

A.2 Calculation of Mismatch Factor

The spectral mismatch factor for the correction of the white light measurements, as discussed in chapter 2:

$$M = \frac{M_{RC}}{M_{TC}} = \frac{\int E_{AM1.5}(\lambda)\cdot S^{RC}(\lambda)\cdot d\lambda}{\int E_{sim}(\lambda)\cdot S^{RC}(\lambda)\cdot d\lambda}\cdot\frac{\int E_{sim}(\lambda)\cdot S^{TC}(\lambda)\cdot d\lambda}{\int E_{AM1.5}(\lambda)\cdot S^{TC}(\lambda)\cdot d\lambda}$$

was determined in the wavelength region from 350 to 800 nm for the SSD containing N719 or silver modified N719 based on the following spectral data:

1. Spectral response of the test cell (S^{TC}) and reference cell (S^{RC})

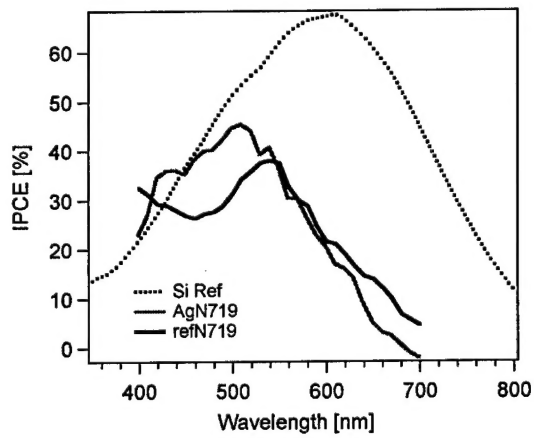

2. The spectral irradiation intensities at AM1.5 ($E_{AM1.5}$) and for the sulphur lamp (E_{sim}) used relative to the test cell respectively relative to the silicon reference cell.

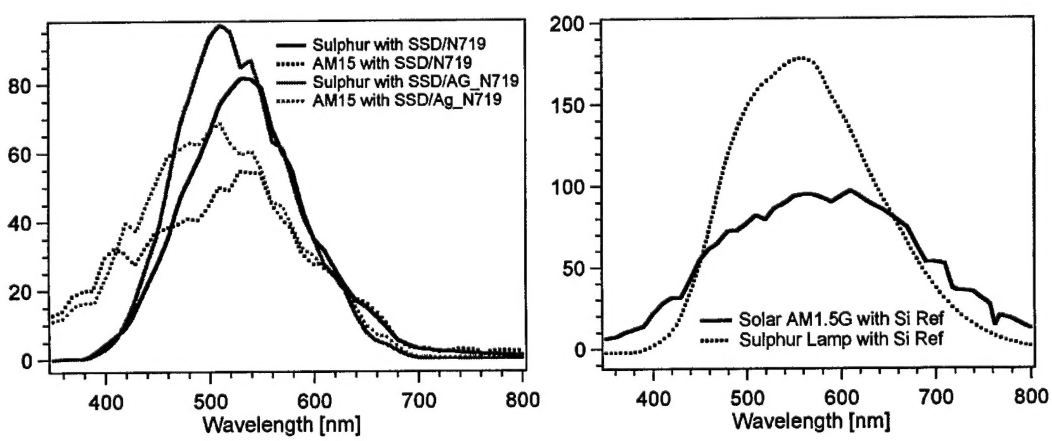

A.3 Device Characterization at NREL

Solid Nano-Crystal Cell

Device ID: 2303 #13H
Mar 29, 2001 11:23 AM
Reporting Spectrum: AM1.5 Global

Device Temperature: 25.0 ± 1.0 °C
Device Area: 1.066 cm^2
Irradiance: 1000.0 W/m^2

NREL X25 IV System
PV Performance Characterization Team

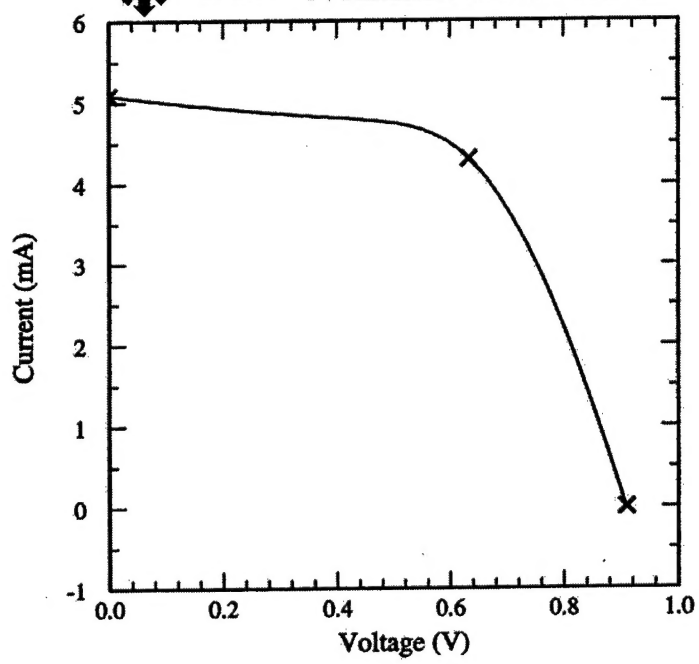

V_{oc} = 0.9103 V
I_{sc} = 5.0842 mA
J_{sc} = 4.7682 mA/cm^2
Fill Factor = 58.97 %

I_{max} = 4.3079 mA
V_{max} = 0.6329 V
P_{max} = 2.7263 mW
Efficiency = 2.56 %

Light soaked for 3 minutes to get to operating temperature.
2 second delay between data points to slow down IV measurement.

Original result sheet of current-voltage characteristics for a SSD with an active surface area of 1.07 cm^2, measured at NREL two weeks after device preparation. The hole conductor matrix was 0.26 mM in $Li(CF_3SO_2)_2N$, 0.18 M in tBP and 0.76 mM in $N(p\text{-}C_6H_4Br)_3SbCl_6$. The device was equipped with silver collecting strips to optimise current collection, an anti-reflecting film and a black mask. IPCE has been determined to 40 % in Lausanne.

A.4 IMPS Model[1]

The continuity equation:

$$\frac{\partial n(x,t)}{\partial t} = \eta \cdot \alpha \cdot \exp(-\alpha \cdot x) + D_{eff} \frac{\partial^2 n(x,t)}{\partial x^2} - \frac{n(x,t) - n_0}{\tau_n} \tag{1}$$

has been solved using the following boundary condition:

$$D \cdot \left. \frac{\delta n(x,t)}{\delta x} \right|_{x=0} = k_{ext} \cdot n(0,t) \tag{2}$$

where k_{ext} equals the potential-dependent exchange rate constant at the back contact. Taking in account that the gradient of the electron density at the surface is zero:

$$\left. \frac{\delta n(x,t)}{\delta x} \right|_{x=d} = 0 \tag{3}$$

the following relation has been formulated:

$$\frac{\delta j}{\delta I_0} = C \cdot \left(\frac{A}{N} + \frac{B}{N} - \alpha\right) \tag{4}$$

with the coefficients:

$$A = \alpha \cdot \exp(-\alpha \cdot d)(k_{ext} + \gamma \cdot D_{eff}) - \gamma \cdot \exp(-\gamma \cdot d)(k_{ext} + \alpha \cdot D_{eff}) \tag{5}$$

$$B = \alpha \cdot \exp(-\alpha \cdot d)(k_{ext} + \gamma \cdot D_{eff}) + \gamma \cdot \exp(\gamma \cdot d)(k_{ext} + \alpha \cdot D_{eff}) \tag{6}$$

$$C = \frac{\alpha \cdot I_0}{\gamma^2 - \alpha^2} \tag{7}$$

$$\gamma = \sqrt{\frac{1}{D_{eff} \cdot \tau} + i \cdot \frac{\omega}{D_{eff}}} \tag{8}$$

[1] L. Dloczik, et al. *J. Phys. Chem. B* **1997**, *101*, 10281-10289.